This is to certify that the

thesis entitled

ELECTRONIC SPECKLE PATTERN INTERFEROMETRY,
ELECTRONIC SHEAROGRAPHY, AND THEIR
APPLICATIONS

presented by

Xiaolu Chen

has been accepted towards fulfillment
of the requirements for

Ph.D. degree in Mechanics

Gary Lee Cloud, P.E.
Major professor

Date 31 January 1996

Electronic Speckle Pattern Interferometry, Electronic Shearography, and Their Applications

By
Xiaolu Chen

A DISSERTATION

Submitted to
Michigan State University
in partial fulfillment of the requirements
for the degree of

DOCTOR OF PHILOSOPHY

Department of Materials Science and Mechanics

1995

ABSTRACT

ELECTRONIC SPECKLE PATTERN INTERFEROMETRY, ELECTRONIC SHEAROGRAPHY, AND THEIR APPLICATIONS

By

Xiaolu Chen

Advances in computer and electronics technologies have brought new life to traditional film based holographic interferometry (HI) and shearography. As a result, the electronic versions of HI and shearography, called electronic speckle pattern interferometry (ESPI) and electronic shearography (ES), have been developed. These developments greatly reduced the rigorous stability requirement and the tedious and slow information processing procedures. Consequently, they have led to a real opportunity for more and more applications in the industrial and scientific worlds.

This paper contains a comprehensive and systematic discussion and analysis of the techniques of ESPI and ES systems and their engineering applications. The effect of the sensitivity vectors on the accuracy of the measurements is analyzed for various cases. A loadingless NDI method and a complementary NDI approach are proposed. Some experimental techniques and results on nondestructive evaluation (NDE) of fiber reinforced plastic (FRP) composite structures and other engineering applications are presented.

To My Family

ACKNOWLEDGMENTS

The author is glad to be able, at last, to offer his sincerest appreciation and gratitude to academic advisor and major professor Gary Lee Cloud for his valuable guidance and encouragement during the course of this research. The author also extends his appreciation to the guidance committee members Dr. Dashin Liu, Dr. Carl Foils, and Dr. Martin Crimp.

To my wife, Jianzhen Xie, and to my sons, Louie and Andrew, I offer love along with my appreciation of their patience and support.

My appreciation is extended to my graduate comrades Jim Nokes and Henry Wede for helpful assistance and discussions.

The author is grateful for support of this research by the Michigan Manufacturing and Processing Institute, The Research Excellence Fund of Michigan, and Lincoln Composites Corp..

TABLE OF CONTENTS

LIST OF TABLES

Table page

LIST OF FIGURES

Figure page

LIST OF ACRONYMS

ALU------ Arithmetic logic unit
CCD------ Charge coupled device
CPU------ Central processing unit
CTE------ Coefficient of thermal expansion
ES-------- Electronic shearography
ESPI------ Electronic speckle pattern interferometry
FEA------ Finite element analysis
FEM----- Finite element method
FRP------ Fiber reinforced plastic
HI-------- Holographic interferometry
LDV------ Laser Doppler velocimetry
LUT------ Look-up table
NDE------ Nondestructive evaluation
NDI------ Nondestructive inspection
NDT------ Nondestructive testing
PZT------ Piezo electric transducer
UDC------ Unidirectional fiber composite

CHAPTER I

INTRODUCTION

1.1 Introduction

With the advances of electronics and computer technology, a new generation of powerful engineering and scientific measuring tools is entering the world of engineering. Among them, electronic speckle pattern interferometry (ESPI) and electronic shearography (ES) have been developed. They are the electronic versions of traditional photographic based holographic interferometry (HI) and shearography respectively.

Because of their high strength-to-weight ratios and designable properties, fiber reinforced plastics (FRP) composite materials are becoming increasingly important for high volume industrial applications such as in the aircraft and automotive industries. Since a composite is a combination of two or more materials, the likelihood of defects in composite components is generally higher than in metals, and the mode of failure is also more complex. Consequently, there is an urgent need for nondestructive inspection of composite structures during and after fabrication. Since defects and damage can develop during service, nondestructive inspections may be required during the lifetime of a critical product such as an aircraft structural component or a pressure vessel. A universally practical method that can effectively and economically detect and characterize defects in composite materials in a production/field environment or a service/maintenance station has yet to be developed. Electronic Speckle Pattern Interferometry (ESPI) and Electronic Shearography (ES) are very promising in this regard.

FRP composites are very different materials from metals when considering which NDT methods are appropriate. In general, FRP materials have poor electrical and thermal conductivity, high acoustic attenuation and high anisotropy of mechanical and physical properties. Therefore, many traditional nondestructive evaluation (NDE) tools can not be effectively utilized to characterize flaws and damage in FRP composites.

At the present time, the NDE methods most widely used in industry for composite inspection are ultrasonics and x-radiography. Ultrasonic techniques detect the flaws by measuring the response to an ultrasonic stress wave travelling in the materials. Because of the point by point or line by line scanning procedure of the technique, the ultrasonic method is normally slow. Usually, some medium (water, gel...) is required to transfer ultrasound energy from the transducer into the material, and this is very inconvenient in some cases. X-radiography relies on the differential absorption or scattering of x-ray photons as they pass through a material. Flaws that either allow more x-ray photons to pass or that absorb or scatter the photons can be imaged if the effect is significant. The molecules in FRP composites are usually of low atomic weight nuclei, and hence the absorption of x-rays is low and contrast is usually poor, especially for a thin plate. Furthermore, neither ultrasonic nor x-ray methods relate the detection to the stress/strain states of the test object in any fundamental way. Therefore, how the detected flaw affects the performance of the component can not be revealed by the experiments.

Advances in electronics and computer science have brought Holographic Interferometry (HI) into the electronics age. As a result, electronic speckle pattern interferometry (ESPI, also known as TV-holography) and electronic shearography (ES, also known as TV-shearography) were developed in the early 70's. Many improvements and modification have been made on these systems since then. These advances have been making optical interferometry more and more acceptable to the industrial world. Consequently, ESPI and ES are becoming important tools for the detection of flaws and damage in materials and structures. Both ESPI and ES are non-contacting, fast, full-field, directly connected to computer, and sensitive to a wide variety of flaws; also, unlike other NDE techniques such as ultrasonics and x-radiography, interferometric techniques relate the flaw detection to the stress/strain state of the object under test. How the flaws affect the performance of the structure can be measured or at least estimated. The techniques can provide directly very important information about the influence of the flaw or damage on the performance of the structure. A permanent record can easily be saved and retrieved for later analysis or comparison in a cost-effective manner.

The current situation is that: (1) ESPI and ES have been developed into very powerful and promising engineering techniques. (2) ESPI and ES systems will be further improved along with the fast and continuous advances in electronics, computer technologies, and optical components. (3) There is a shortage of effective testing tools for new materials, new manufacturing processes and new construction techniques. (4) Although there have been many reports on applications of ESPI and ES techniques, their potentials are still far from fully exploited. (5) Industries in general are still slow in realizing the capabilities of ESPI and ES, thus they have not really enjoyed the benefit of the new technologies. On one hand there are the researchers who understand what powerful tools ESPI and ES are, but they don't know where or what the real problems are. On the other hand, we have the manufacturers, people who make things and have problems with the things they make. They are not aware that ESPI or ES is a possible solution, and this is the main reason why

ESPI and ES have not been very popular in industrial applications.

ESPI and ES will have more applications in both industry and research. In this work, the focus is on the systematic study of ESPI/ES and on NDE applications for FRP composite materials. The ultimate goal is to help bridge the gap between system development and practical applications.

1.2 Objective and scope

This work is composed of two parts: (1) a systematic and comprehensive development of theory and practical techniques of ESPI and ES systems, and (2) NDE of FRP composite materials and other applications using ESPI and ES systems. In the study of ESPI and ES theory, a detailed analysis and discussion is presented. Practical problems in using the systems are also discussed. A numerical model of ESPI system has been programed using Matlab software to analyze the influence of the sensitivity vectors on the accuracy of the measurements. A novel NDE method for FRP composites is proposed and presented. This technique takes advantage of the creep characteristics of the FRP materials under room temperature and gravity, and it may offer a "loadingless" method to the NDE of FRP composites. A new approach which makes use of the advantages of ESPI, ES, and ultrasound is proposed for effective nondestructive inspection. Some experiments on NDE of the impact damage of composite vessels will be shown along with other applications.

This Chapter is an introduction which describes briefly the historical background, the outline of the systems, and the applications. Chapter Two and Chapter Three deal with ESPI and ES systems respectively. Chapter Four focuses on the sensitivity analysis of both systems. Chapter Five presents some experimental techniques, results, and discussion of applications of ESPI and ES systems.

1.3 Background of the techniques and their applications

As mentioned previously, ESPI and ES are the digital electronic descendants of traditional photo-material based optical interferometries. Their developments have opened many new opportunities. An extensive literature review has been conducted in the areas of system development and applications. Over three hundred papers have been reviewed. Many of these papers are listed in the references in the back of this paper.

1.3.1 Historical background

In 1948, the basic principal of holography was invented by Dennis Gabor [1948, 1972]. The word holography comes from the Greek word holos meaning " the whole ". In a hologram the entire wave front including amplitude and phase is recorded. In the ordinary photographic process, the film records the intensity, throwing away the phase information. When a hologram is properly illuminated, an exact replica of the original wave front is reconstructed. This means that three-dimensional information is recorded in a hologram, as compared to two dimensions by an ordinary photographic camera. Descriptions of holography can be found in the books by Hariharan [1984] and Saxby [1988].

Holographic Interferometry (HI) was first demonstrated by Powell and Stetson [1965]. A comprehensive coverage of HI before 1978 can be found in an excellent and comprehensive book by Vest [1979].

A schematic of HI is shown in (a) of Figure 1.1. In holographic interferometry, one of the interfering wave fronts is stored in a hologram and then compared with another wave front. Alternatively, interference can take place between two stored wave fronts. This makes it possible to compare wave fronts which were originally separated in time or space. Through HI, one can produce three-dimensional images of diffusely reflecting objects which appear to be overlaid by interference fringes that are indicative of deformation, displacement or rotation of the object.

In spite of HI's advantages, industry in general has been slow and reluctant to accept this technique. HI has been mostly confined to research laboratories. The reasons for this, apart from the usual distrust towards new unfamiliar techniques, include the following: (1) The stability requirement in holography is not readily compatible with industrial environments. (2) The photographic recording process and subsequent development introduce an annoying time delay which prevents on-line inspection. Although new self-developing and reusable recording media such as photothermoplastic plate (film) and retrorefractive crystal have been developed, there still remains a time delay between recording and observation of the results. (3) Lack of direct connection with modern electronics and computers makes quantitative analysis of the results difficult. (4) The recording material cost is not cheap. (5) A highly trained lab technician is required.

In 1960, following the development of the CW HeNe laser, a phenomenon which attracted immediate attention was the granular appearance of a diffusing surface illuminated by the laser beam. This phenomenon was named ‘speckle’ [Dainty 1984; Halford, Gamble, and George 1987; Markhvida and Tanin 1991]. Laser speckle is the essential information carrier in HI, ESPI, ES and speckle photography. Laser speckles are

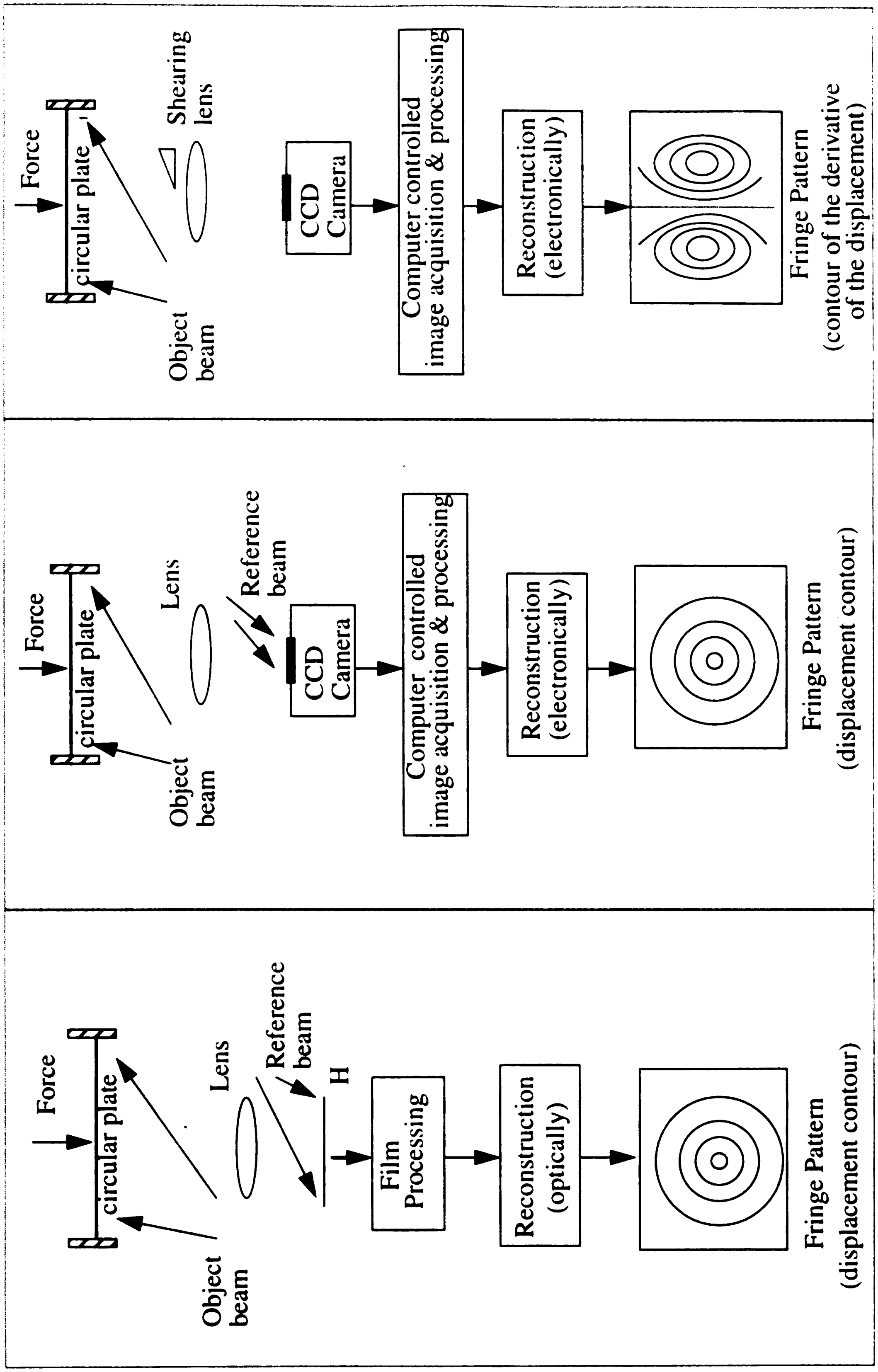

Fig. 1.1 Comparison of HI, ESPI, and ES.

the result of multiple interference of wavelets which arise from microscopic elements of the surface when a rough surface (in comparison with the optical wave length used) is illuminated by a laser wave. The speckles can be classified into two categories depending on their formation: objective and subjective speckles. The former are those intrinsically created by the illuminated surface, and the latter are those viewed through a lens or by the eye. The spatial frequency spectrum (speckle size) of the objective speckles is determined by the roughness or non-homogeneity of the surface, whereas the spatial frequencies of subjective speckles are controlled by the f-number of the lens or eye, thus the term subjective. Laser speckle was regarded, initially, as a nuisance since it caused a granular appearance. However, it was soon realized that speckle çould be used as a carrier of useful information. The property of speckle used in ESPI and ES is that when the surface moves the speckle created by the surface also moves. As a result, speckle has found a number of applications in measurement [e.g. Erf 1978; Françon 1979; Froehly 1981; Chiang 1982; 1993; Conley and Genin 1990].

In 1971, the first ESPI systems were developed independently by Butters and Leendertz in England [1971], and by Macovski et al. in the United States [1971]. A schematic of TV-holography is depicted in (b) of Figure 1.1 (page 7). The development of ESPI was reviewed by LØkberg [1980] and by Joenathan [1990]. The English group named the technique Electronic Speckle Pattern Interferometry (ESPI). In the literature, the name ESPI seems to be used more than the other names (TV-holography or Digital Electronic Speckle Interferometry). The English group is the only one of the pioneering groups which has continued ESPI research and development up to date. In the past twenty-some years, ESPI has been improved into a very valuable and promising measurement tool for engineering applications and scientific research. The major differences between HI and ESPI are the recording media and the information extraction process. Photographic materials are used as the recording media in HI, while in ESPI a CCD camera is used. The information is optically extracted in HI while the information is electronically extracted in ESPI.

Speckle shearography was developed by Leendertz and Butters in 1973 [Leendertz and Butters 1973], and by Hung and Taylor in 1974 [Hung and Taylor 1974]. The digital version, called electronic shearography (ES), was later developed by Nakadate et al., among others [Nakadate, Yatagai, and Satito, 1980a]. Like HI and ESPI, the only differences between traditional shearography and ES are the recording device and the information processing method. A schematic of ES is shown in (c) of Figure 1.1 (page 7). The fundamental difference between ESPI and ES is the optical setup. ESPI is a two-path interferometry (interference between a reference beam and an object beam) which measures the displacement, while ES is a single-path (common-path) interferometry (interference between two speckled beams produced from a single beam by a shearing device) which measures the derivative of the displacement.

Figure 1.1 illustrated the main differences among HI, ESPI and ES. The spatial characteristics of a holographic image are superior to ESPI or ES images, because HI photographic recording materials have higher resolutions than CCD cameras. However, it is the favorable temporal characteristics and the direct computer controlled automatic information analysis which make ESPI and ES valuable. In ESPI and ES, 30 (American TV standards) interferograms (speckle patterns) are recorded and reconstructed per second. The resulting real-time presentation of holographic interferometric results is the greatest asset of ESPI and ES. Photographic recording materials have the disadvantage that the time and effort of processing is considerable, particularly in the case of real-time measurements. This is especially detrimental when repetitive inspection in an industrial environment is needed. ESPI and ES dramatically reduce the time and effort involved. ES is closely related to ESPI. A CCD camera is used in both of the systems and the information processing software is almost the same.

1.3.2 Outline of the systems and applications

Limited overall discussions of systems and applications can be found in a few sources [Løkberg and Slettemoen 1987; Jones and Wykes 1989].

To facilitate a brief discussion of the systems and applications, a block diagram is shown in Figure 1.2. Although Figure 1.2 shows conceptually an out-of-plane sensitive

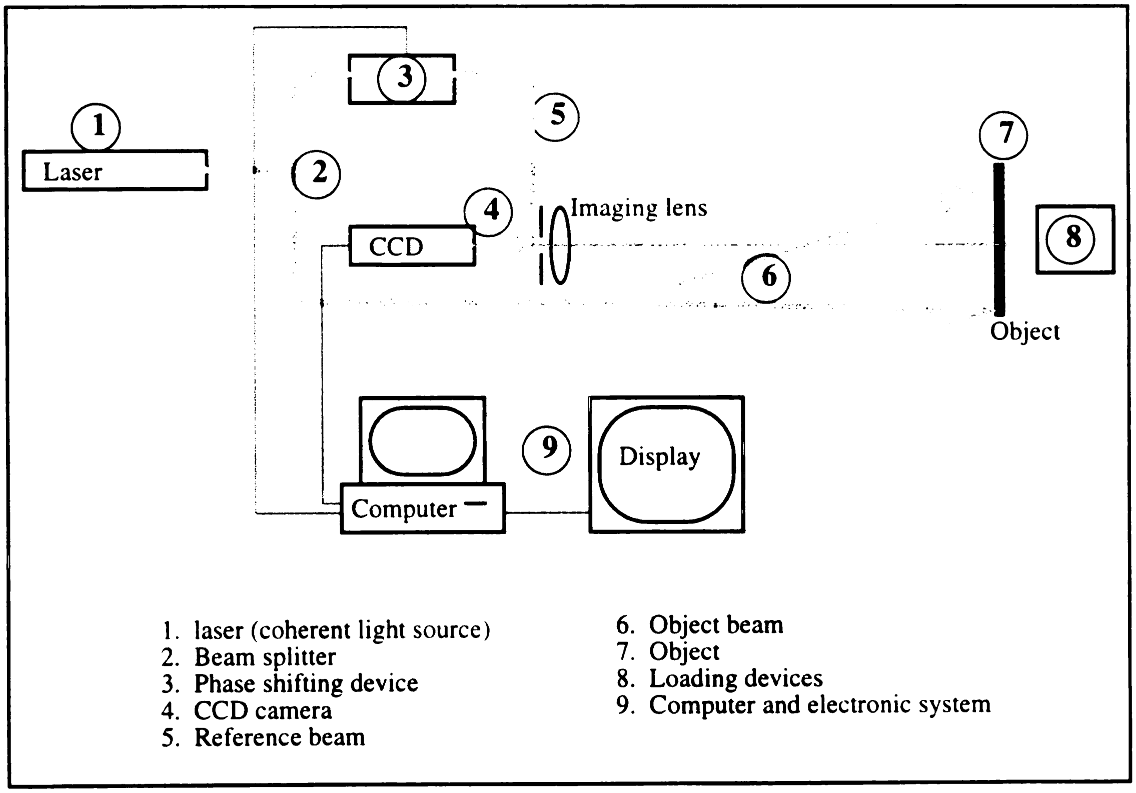

Fig. 1.2 Block diagram of the conceptual system.

ESPI setup, it can be configured into ESPI in-plane or ES setups. An in-plane sensitive ESPI setup can easily be arranged by shifting reference beam "5" to illuminate the object in the same way as the original object beam "6" but on the opposite side of the optical axis. An ES setup can be achieved by blocking or removing the reference beam "5" and changing the regular imaging lens to an image-shearing lens.

Basic elements and applications involved with ESPI and ES studies are briefly discussed below:

(1) Laser

Lasers are used to provide a coherent source as required for ESPI and ES to work. Three functioning parameters of the laser should be considered: (a) coherence length, (b) wavelength, (c) output power. The coherence length should be long enough for the object under test. The wave length should be in the sensitive region of the spectral response curve of the CCD camera. The required output power depends on the size of the test area and the surface condition. There are continuous lasers and pulsed lasers for different applications.

(2) Optical designs

Optical system design is used to achieve various optical setups for ESPI out-of-plane sensitive, ESPI in-plane sensitive, ES (out-of-plane derivative sensitive) or other arrangements. In designing the optical systems, a number of factors should be considered such as stability, easy alignment, path length compensation, reference beam intensity adjustment and object beam steering. Designs using fiber optics can make the system rugged, compact, and light in weight. A typical ESPI system uses an in-line smooth reference beam. An off-axis speckled reference beam design can make the system easy to align [Joenathan and Khorana 1991]. Feedback control to compensate for environmental noise and rigid body motion can also be achieved [Sciammarella, Bhat, and Bayeux 1993]. A multi-function design which combines ESPI and ES together was proposed by Cloud et al. [1993, 1994]. A combination design of ESPI + laser Doppler velocimetry (LDV) has been demonstrated [Valera, Doval, and Jones 1993].

(3) Phase measuring techniques

To obtain quantitative measurement, phase stepping or phase-shifting techniques are implemented in ESPI and ES. The basic principle of determining phase change is to artificially introduce known or constant phase changes in one of the beams in the interferometer. There are a number of phase changing devices and algorithms for determining the phase or phase change [Creath 1985]. For ESPI using optical fiber, the phase changes are best introduced by stretching the optical fiber using a PZT device. The actual phase or the phase change is then calculated by removing the modulo 2π ambiguity through phase unwrapping methods. Finally, the obtained phase information is converted to the displacement information with the consideration of the system sensitivity vector, and the result is displayed on the monitor.

(4) CCD device + Imaging lens

For the ES setup, as described before, the regular imaging lens is switched to an image-shearing lens. There are many designs to produce various shearing effects including lateral, radial, rotational and folding [Ganesan, Joenathan, and Sirohi 1988]. Lateral shearing is the one mostly used. Devices which can produce lateral shearing include the Michelson interferometer, glass wedge [Hung 1982], Fresnel biprism

[Nakadate et al 1980], two inclined glass plates [Klumpp and Schnack 1990], a split lens and birefringent devices. The amount of shearing can be varied in some of the designs. For good result the two sheared beams should be equal in intensity. The aperture of the imaging lens should be adjusted to satisfy the resolution requirement of the CCD device. Currently, the CCD device commonly used has 512 x 512 sensing elements. Although, higher resolution CCD devices (2048 x 2048) are available, there exists a trade-off between resolution and speed or price.

(5) Reference beam

An in-line smooth reference beam is used in most out-of-plane sensitive ESPI setups, which has the benefit of doubling the size of the speckles [Dainty 1984] and producing quality fringes. The reference beam "5" is removed or blocked in an ES setup. To obtain quantitative phase information, phase measuring techniques are normally implemented in the reference beam.

(6) Object beam

For out-of-plane sensitive ESPI, the object beam is normally a diverging beam from a spatial filter or from the end of an optical fiber. The object beam should cover the test area of interest and be strong enough to have good modulation with the reference beam after being collected by the imaging system. For in-plane sensitive ESPI, the two object beams should have equal intensity.

(7) Applications

The use of ESPI and ES has been demonstrated in many areas such as vibration analysis, nondestructive inspection and testing, material property characterization, bioscience and environmental study. Much effort is still needed to bring the techniques to more industrial applications. The experimental part of this research is concentrated on NDE of FRP composites. Detection of flaws and damage using ESPI and ES is based on the comparison of two stress states of the object. The flaws and damage are typically shown in the fringe pattern as some fringe anomalies such as "bull-eye", "butterfly", fringe discontinuity, and abrupt curvature or density changes of the fringes.

(8) Loading techniques

Loading technique plays a key role in successful nondestructive inspection of flaws and damage. Development of NDE methods using ESPI and ES eventually becomes the development of practical stressing techniques so that the flaws and damage can be effectively revealed. The loading or stressing techniques commonly used include mechanical loading, thermal stressing, pressure or vacuum, and vibration excitation. Note that for each type of the loading, there may be various ways to carry it out.

(9) Computer and electronic system

Computer technology has paved the way for the success of ESPI and ES. To take advantage of digital technology, the interference speckle pattern in the CCD sensing array is digitized by a frame grabbing board in the computer for subsequent image processing. Digital image processing can be implemented either in software or at higher speed using dedicated processing hardware. Normally, a frame grabbing board (typically including A/D, D/A and look-up tables) and a frame processor board are installed in the computer that controls ESPI or ES by menu driven software. With advances in electronics, CCD devices with higher and higher resolution will be used, and the speed will be compatible with the TV rate.

(10) Theoretical fundamentals

Fundamental aspects related to ESPI/ES are mainly concerned with the decorrelation mechanism and characteristics of the speckles [Jones and Wykes 1989; Chen 1992; Cloud 1995]. Decorrelation causes loss of phase information, therefore, no measurement can be made.

CHAPTER II
ESPI SYSTEM

2.1 Introduction

The basic idea of ESPI was developed in England by Butters and Leendertz [1971], and in the United States by Macovski et al. around 1971 [Macovski, Ramsey, and Schaefer 1971]. Many improvements have been made since then. The most notable development seems to be the use of a PZT phase shifting technique which enables quantitative displacement calculation. ESPI is an electronic version of holographic interferometry. It measures the displacements. Vibration modal analysis can also be vividly presented using ESPI. ESPI is under continuous development in both the technology itself and in its applications.

2.2 Basic operation of ESPI

In HI, film is used to record the information, while a CCD camera is now used in ESPI. Direct connection of ESPI to computer systems is readily achieved. ESPI can be operated in two modes, namely, the real-time mode and the time-average mode. In real-time mode, depending on the optical setup, ESPI measures the out-of-plane displacement or in-plane displacement. Fringe patterns in this case are the displacement contours. In time-average mode, ESPI displays the vibration mode shape. In this case the fringe pattern shows vibration amplitude contours. The major advantages of ESPI are: (1) Computer controlled fast data acquisition (1/30 sec. per frame), signal processing and graphical result presentation. Quantitative measurement of very small displacement can be achieved through the use of a phase measurement technique. (2) The system does not require the highly stable environment necessary for conventional holographic interferometry. (3) The system can be used in brightly lighted conditions; no dark room is needed. (4) Since no film and no processing of film are needed, there is virtually no material cost. A permanent record can easily be saved on disk or video tape for later use.

A schematic diagram of a typical (out-of-plane) ESPI system is shown in Figure 2.1. For most work, a He-Ne laser or a diode laser is normally used. Only when a large area has to be covered at once is an argon laser used. In the diagram, PZT is a piezo-electric transducer which is controlled by a computer, and it is used for shifting the phase of the reference beam in order to calculate the phase change introduced by the deformation of the target. M1 and M2 are mirrors. P is a prism used to compensate the optical path length of the reference beam so as to satisfy the coherence condition. C is a cubic prism used to combine the reference beam and the object beam at the image plate of the CCD camera. SF1 and SF2 are spatial filters. BA is a beam attenuator. BS is a beam splitter. L is an imaging lens with focal length f adjustable from 30 to 70 mm. For a typical 512 x 512 CCD, an aperture of 11, 16, or 22 is normally used to satisfy the resolution requirement of the CCD camera and at the same time to optimize the light intensity. The optimum result is obtained by experiment.

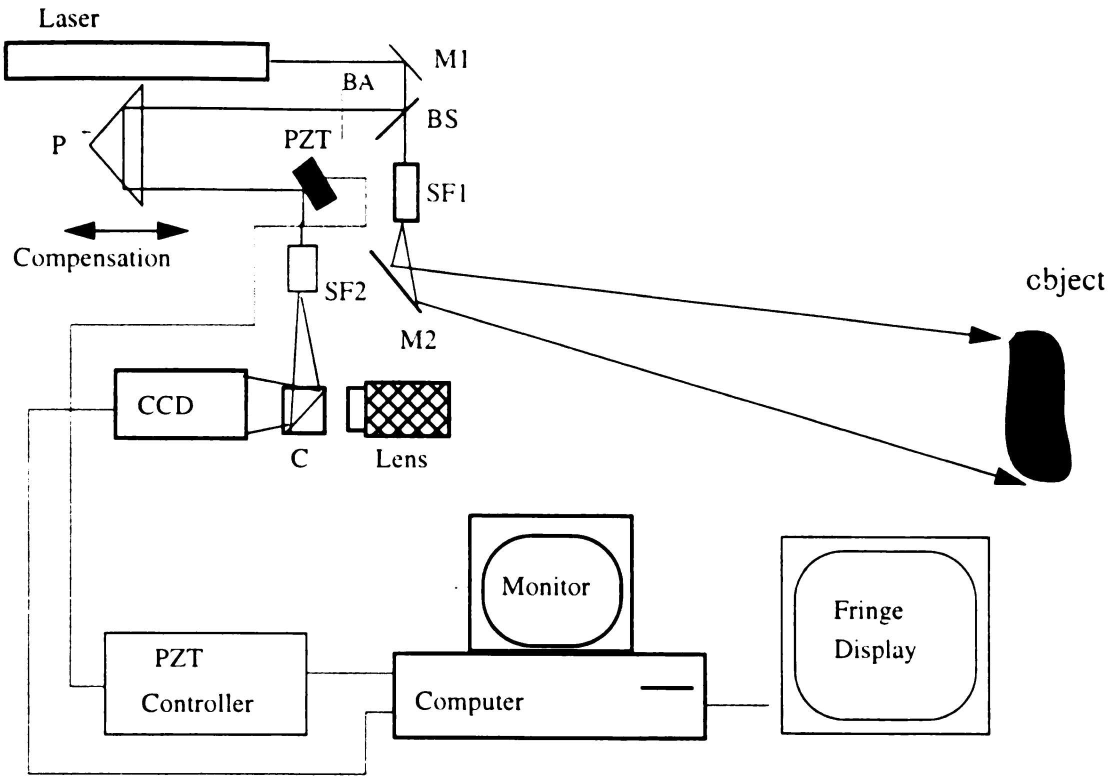

Fig. 2.1 A schematic of a typical ESPI system.

In real-time mode, ESPI operates in a three-step process. At the first step, the coherent combination of the reference beam and the object beam at a point or pixel in the CCD sensor plane results in the intensity of light

$$I_1 = I_r + I_o + 2\sqrt{I_r I_o}\cos\phi_0 \tag{2.1}$$

where I_r is the intensity of the reference beam, I_o is the intensity of the object beam, and ϕ_0 is the random phase difference between the two beams. The reference image can be taken from the test object in either an undeformed state or a deformed state. A computer equipped with a frame grabber board digitizes the entire video frame in 1/30 of a second (US standard). The frame (speckle pattern) then is stored in a frame buffer. At the second step, the object is deformed by applying one or more loading techniques. At this stage the intensity of light on the CCD camera becomes

$$I_2 = I_r + I_o + 2\sqrt{I_r I_o}\cos(\phi_0 + \Delta\phi) \qquad (2.2)$$

where $\Delta\phi$ is the additional phase change due to deformation of the object. During the loading process, the subsequent frames are subtracted continuously from the stored reference frame. The subtracted results can be expressed as

$$\Delta I = I_1 - I_2 = 4\sqrt{I_r I_o}\sin\left(\phi_0 + \frac{\Delta\phi}{2}\right)\sin\frac{\Delta\phi}{2} \qquad (2.3)$$

The subtracted results, when displayed on a TV monitor, yield fringes which are contours of constant phase change. The frame grabber board in the computer can perform real-time arithmetic and logic image processing operations including AND, OR, frame averaging, frame subtraction and addition, etc.. These operations are accomplished on-board through the use of a look-up table processor, which enables the results to be displayed at 30 frames per second. The video signals are proportional to the intensities, and hence the subtracted electronic signal $V \propto \Delta I$. Brightness on the monitor is then proportional to V. The brightness is maximum when $\Delta\phi = (2n+1)\pi$ and minimum when $\Delta\phi = 2n\pi$, n being an integer. $\Delta\phi$ is related to the optical geometry of the setup and the displacement vector. We have,

$$\Delta\phi = \vec{K} \bullet \vec{L} \qquad (2.4)$$

where $\vec{K}$ is the sensitivity vector of the optical setup, and $\vec{L}$ is the displacement vector.

For quantitative phase (displacement) calculation, phase shifting or stepping techniques are used. Several controlled phase steps are introduced to the reference beam, which results in at least three equations for solving the displacement introduced phase change. $\Delta\phi$ of every pixel point is then unwrapped to obtain the overall phase map of the entire test surface. The phase measurement techniques are discussed in detail in Section 2.9.

In time-average mode, ESPI can display the vibration mode shapes. For a sinusoidal vibration, the mode shape displayed on the TV monitor is given by

$$V \propto I = I_r + I_o + 2\sqrt{I_r I_o}\, J_o\left(\frac{4\pi}{\lambda} a_o\right) \cos\phi \tag{2.5}$$

where a_o is the vibration amplitude, and J_o is the zero order Bessel function.

2.3 The measurement probe--coherent light

Lasers are used to provide a coherent source for ESPI to work. Three functioning parameters of the laser should be considered: (1) Coherence characteristics -- adequate coherence is needed for any type of interferometry to work. Single mode output is always desired. Different lasers may have different coherence length. Since the structures tested are normally three dimensional, a certain amount of coherence length is needed. Furthermore, the longer the coherence length, the easier the path length match between the reference beam and the object beam; (2) Wavelength -- wavelength is the ruler of the measurement. The most important thing for wavelength is that it should fall into the sensitivity region of the spectral response curve of the imaging device. The sensitive range for a typical CCD camera is about 300 - 900 nm. Besides the sensitivity problem, visible light, obviously, is easier to work with than invisible light; (3) Power -- When a large object is to be measured, a relatively powerful laser may be needed. For static or quasi-static measurements, a CW (continuous wave) laser is used. A pulsed laser is normally employed for dynamic (transient or periodic) measurements. Short pulses (~20 ns) can freeze all but the most rapid of ambient vibrations and movements. However, pulsed lasers do not always remove the need for vibration isolation. When a long time interval is required between the two exposures, it is important that the objects do not have rigid body motion between exposures, or error fringes will appear in the final results. If the rigid body motion is excessive, fringes (information) will be completely washed out.

The main characteristics of some commonly used lasers for interferometry are summarized in Table 2.1.

Table 2.1 Commonly used lasers in interferometry

Laser Type	**Wavelength (μm)**	**Output**
HeNe	0.6328, 0.54, 1.15	0.5 - 50 mW
Argon ion	0.5145, 0.4880	0.5 - several W
Semiconductor	0.87, 0.75, 0.67	~1 - 100 mW
Ruby	0.6943	~0.6 - 10 J
Nd:YAG	1.06, 0.503(double v)	0.1 - 0.15 J
Dye	0.4 1- 1.08	~5 - 100 mW
CO_2	10.6	~1 W - several kW

The HeNe laser is inexpensive and provides a continuous output. An Argon ion laser is quite expensive and it is generally used for testing larger objects. When several lines are present in an argon laser the output wavelength may be selected by a prism. Operation on a single longitudinal mode is obtained by using a short Fabry-Perot etalon as a mode selector in the laser cavity. Semiconductor lasers (diode lasers) are now being used to an increasing extent. They have the advantages of low cost, small size, high efficiency, long coherence length, and potentially high power compared with the HeNe laser. Operation on a single longitudinal mode can be obtained quite easily. In addition, they can be tuned over a limited range by varying the injection current or the body temperature. It is possible to drive a diode laser in cw or pulsed mode. The major disadvantage is that most diode lasers emit invisible radiation. Dye lasers can be tuned over a fairly wide range with a given dye. A dye laser may be used in two-wavelength shape measurement if a wide range of contour interval is required. Very short pulses of light (~ 15 ns) with very high peak powers can be produced by ruby and Nd:YAG lasers. They are quite expensive, but are necessary for some unstable dynamic measurements.

2.4 The information carrier--laser speckles

Laser speckle is the displacement information carrier. The fundamental principle of ESPI and electronic shearography (ES) operation is based on the coherence nature of laser speckles. Laser speckle is created when a laser is used to illuminate a rough surface (compared with the laser wavelength). Light scattered from the surface is speckled. Figure 2.2 shows a picture of magnified laser speckles. Laser speckle is a result of the coherent addition of laser light scattered from an object surface; laser speckle itself is also coherent. Figure 2.3 shows a magnified picture of the result of interference between two laser speckle patterns where two beams join at a narrow angle. Note the grating-like modulation of the speckle.

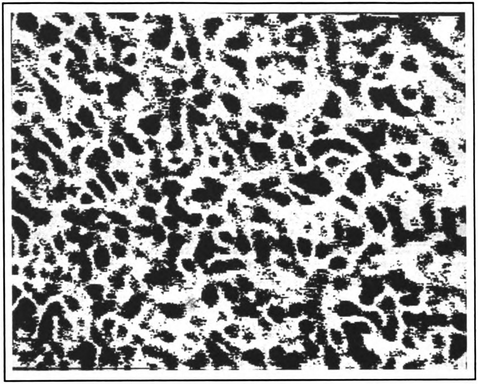

Fig. 2.2 A laser speckle pattern.

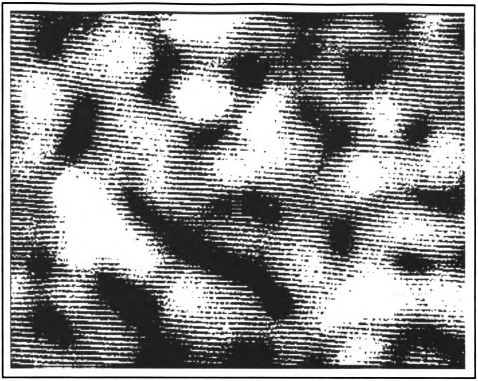

Fig. 2.3 Interference of two laser speckle patterns.

When the speckle field is formed by collecting the scattered radiation field with an imaging system and focusing it onto the screen (Figure 2.4) a 'subjective' speckle pattern is formed. The size *S* of the individual speckles in this case is then related to the aperture ratio *F* of the lens (the *f*-number) and the magnification *M* of the lens. The speckle size in the image is

$$S \approx 1.22(1+M)\lambda F\ , \tag{2.6}$$

From simple lens theory, the speckle size on the object is given by

$$S_{obj} \approx 1.22(1+M)\lambda\frac{F}{M}\ , \tag{2.7}$$

This is defined as the resolution element on the object. Subjective speckle is the type that is used in ESPI and most other speckle metrology methods.

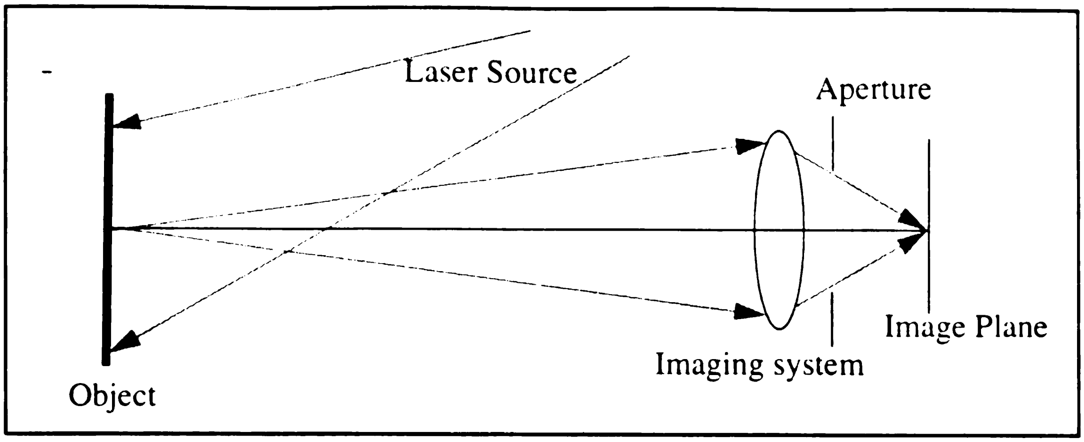

Fig. 2.4 Formation of 'subjective' laser speckles.

The motion of speckle patterns with motions of an object has been discussed extensively by Dainty [1984] and Erf [1978], among others. The general conclusion is that speckles in the image of an object will either shift their location as the object moves, or they will change their pattern, or both. Changes in the pattern of the speckles will cause a loss of correlation between the speckle patterns in subsequent pictures of the object. If the decorrelation is excessive, no fringe will be observed [Jones and Wykes, 1989; Cloud 1995].

If the field penetrates into the object sufficiently, or if multiple reflections occur on the object surface, the field scattered by the object may be highly sensitive to changes in the angle of illumination. Thus, rotations of the object relative to the illumination will affect the speckles formed by the imaging lens. If none of these factors operate, then the speckles in the image of the object will retain their pattern with motions of the object, and, furthermore, if the object is in focus, the speckles will retain their position on the object itself. If the object is not in focus, translations of the speckles relative to the object surface may be expected if the surface of the object rotates [Stetson 1975].

de

Th

de

2.

the

2.

(1

is

ho

di

ho

(2

ab

te

no

In general, the interference between two speckle patterns is more sensitive to decorrelation than the interference between a smooth reference field and a speckle pattern. The out-of-plane gradient-sensitive interferometer (e.g. ES) is the most sensitive to decorrelation.

2.5 The image recording device

An image (laser speckle pattern) may be recorded by a photographic film, a photo-thermoplastic plate, a CCD (charge coupled device), or a photorefractive crystal.

2.5.1 Comparisons of different recording media:

(1) Holographic film

Holographic film and plate have a resolution of 1000 lines/mm to 5000 line/mm which is adequate for all types of holography and interferometry. The major disadvantage of holographic emulsion is the need for chemical processing, which is time consuming and difficult to perform in situ. This has been one of the major barriers to the transfer of holographic techniques from the research lab to a test or production environment.

(2) Photo-thermoplastic

Photo-thermoplastic medium has about 300 lines/mm resolution and it can be reused about 1000 times. It permits on-site developing, and no chemicals are involved. This technology has greatly helped the transfer of holographic techniques from laboratory to non-research areas.

(3) Photorefractive crystals

Photorefractive crystals (e.g. Fe:$LiNbO_3$) are erasable and reusable without fatigue. Real-time recording and readout is possible. Short-pulse recording of high-speed phenomena is also possible [Magnusson et al 1994]. An application using photorefractive crystal ($Bi_{12}TiO_{20}$) as the recording media to study the elastic properties of solids was reported by Kamshilin et al [1990]. At present, the fringe visibility seems to be poor.

(4) CCD

The resolution for a CCD camera is typically in the range of 50 ~ 100 lines/mm. It is much lower than that of films, but it is satisfactory for most practical applications in speckle interferometry. Advantages are the speed and the direct interface with computers.

2.5.2 The CCD camera

A CCD (charge-coupled device) and an imaging lens are normally used to record the interferograms (the speckle pattern). The aperture of the imaging lens should be such that it matches the resolution of the CCD camera. A CCD is a solid-state sensor element. When a CCD is exposed to light, charge packets proportional to the light intensity develop, then stored charge packets are shifted to the storage CCD array which is not exposed to light. The light intensity values are then read from the storage array. Depending on how the imaging and storage CCD arrays are configured, different methods [Flory 1985] have been developed to read the light intensity values from the storage array.

In a standard TV setting, the frame is transferred at a rate of 30 frames per second (US standard). At present, a CCD camera with 512 x 512 elements is typically used in ESPI.

Although, 2048 x 2048 pixel CCDs are available, the price is high. Moreover, in order to acquire a 2048 x 2048 image at the video rate, one needs to digitize the picture at a pixel rate of about 126 MHz. This kind of frame grabber currently is not available.

When selecting a CCD camera for interferometry, additional considerations are: (1) the spectral response should be compatible with the wavelength of the laser used, (2) an optical filter may be needed in front of the imaging lens, and (3) an imaging lens with variable focal length is desired.

An increase in the resolution of a CCD camera decreases the *f*-number which is required to give fully resolved speckles. Therefore, for given object, the required laser power can be reduced. An increase of the resolution has other advantages. The speckle size is decreased by increasing the aperture (reducing the f-number), which makes the fringes less grainy and therefore smoother. If there is no memory loss effect [Chen 1992; Cloud 1995], the measurement range (the total number of fringes) may be increased because the fringe density is limited by the speckle size [Jones and Wykes 1989].

2.6 Optical system designs

The general purpose of optical system design for ESPI is to develop a system that is easy to align, robust, and compact enough for an industrial environment. Additional considerations are path-length compensation and variable intensity for the reference beam. Path-length compensation may not be needed when the laser used has a very long coherence length. Depending on the measurement, the optical system can be configured into an out-of-plane displacement sensitive setup or an in-plane displacement sensitive setup.

2.6.1

O

by an

norm

vec

ma

wh

pr

ve

(1

be

2.6.1 Out-of-plane displacement sensitive ESPI

Out-of-plane sensitive ESPI measures the out-of-plane displacement. This is achieved by arranging an object illuminating beam and a reference beam to meet at the image plane, normally, the target of a CCD camera. A principle design is shown in Figure 2.5.

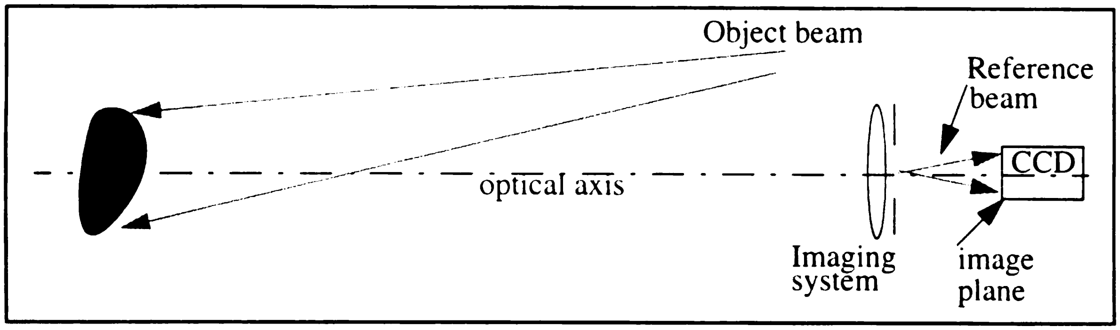

Figure 2.5 A principle optical design of an out-of-plane sensitive ESPI.

For an ideal out-of-plane sensitive setup in which the illumination and the observation vectors are parallel with the optical axis, the probed phase change due to a displacement may be expressed by

$$\Delta\phi \approx \frac{4\pi}{\lambda} d_z \tag{2.8}$$

where d_z is the out-of-plane displacement component. Detailed discussion will be presented in Chapter 4 about the measurement analysis and the influence of the sensitivity vectors on the accuracy of ESPI measurements for number of practical cases.

(1) On-axis smooth reference beam designs:

Typical out-of-plane sensitive ESPI systems use an on-axis (in-line) smooth reference beam arrangement. This arrangement is aimed at increasing the size of the speckle to satisfy

The si

doubl

patte

smoo

objec

2.1.

sc

be

in

co

ref

pi

L_2

satisfy the resolution requirement of the CCD camera and to improve the fringe quality. The size of the speckle on the detecting array of the CCD camera is approximately doubled when a strong uniform in-line reference beam is combined with the speckle pattern from the object [Dainty 1984]. Figure 2.6 shows one setup which uses an on-axis smooth reference beam. A beam splitter is used to combine the reference beam and the object beam. A cubic prism may also be used for this purpose, as was shown in Figure 2.1.

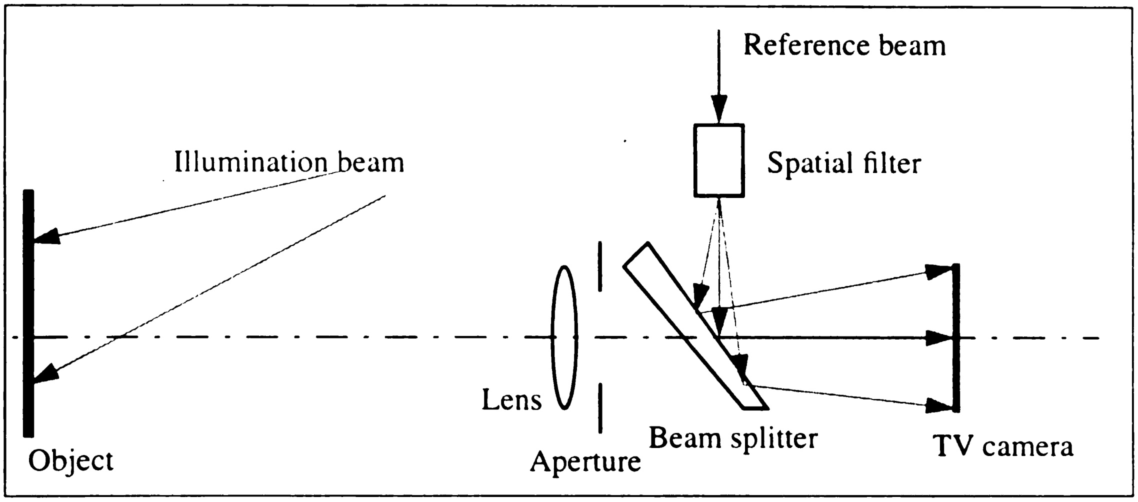

Fig. 2.6 On-axis setup using a beam splitter.

The setup shown in Figure 2.6 suffers from the disadvantage that dust particles and scratches on the beam splitter can act as light scattering sources, which cause reference beam noise and hence degrade the quality of addition fringes. However, If ESPI operates in the subtraction mode, this should not be a serious concern. Another arrangement which considerably reduces the reference beam noise is shown in Figure 2.7. The unexpanded reference beam is pre-expanded by lens L_1 and then focussed down through a mirror-with-pinhole [Jones and Wykes 1989]. The reference beam is aligned by translating the lens L_2 so that its focal point coincides with the pinhole. The small hole in the mirror does not degrade the image quality unless a significant fraction of the light transmitted by the viewing lens is incident on the hole. Since the quality of the reference beam is very important, all internal reflections in the camera front should be avoided.

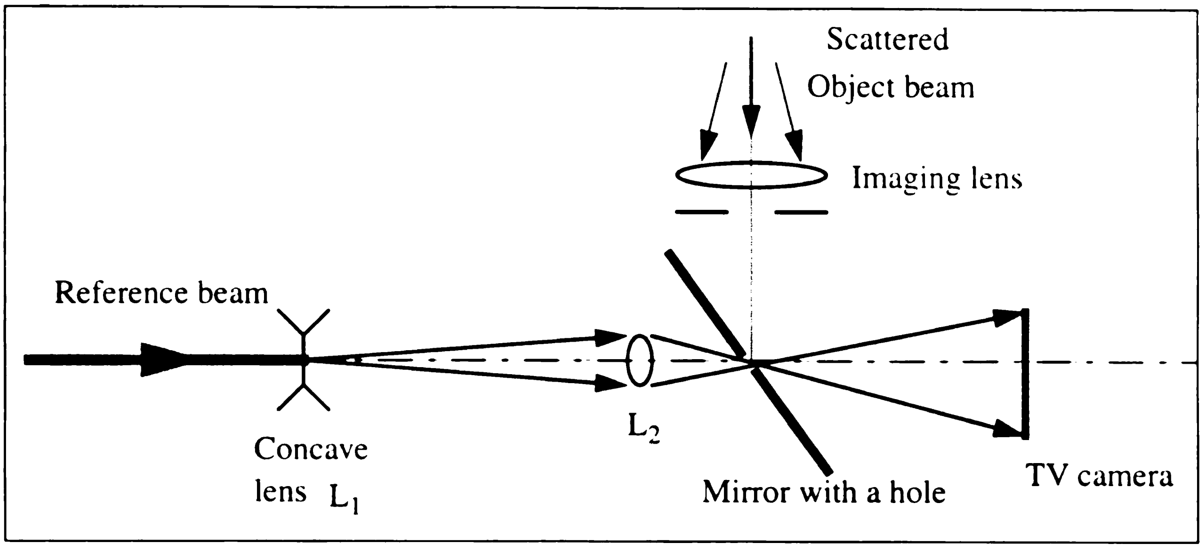

Fig. 2.7 On-axis setup using a hole-in-mirror design.

(2) Off-axis scattered reference beam designs:

In the on-axis ESPI setup it is well known that misalignment of the reference beam reduces the visibility of the fringes; and if the optical system is not well designed, the misalignment could also result in tedious work. To make the system insensitive to reference beam misalignment, an off-axis system was proposed by Joenathan and Khorana [1991]. Figure 2.8 is a schematic of this setup. In this arrangement, a mirror attached to a PZT device is placed beside the object to direct part of the illuminating beam to a ground glass placed in front of the imaging lens. The ground glass is so placed that it covers half of the aperture of the imaging lens. The disadvantage is that a collimated beam has to be used, which limits the application of this setup.

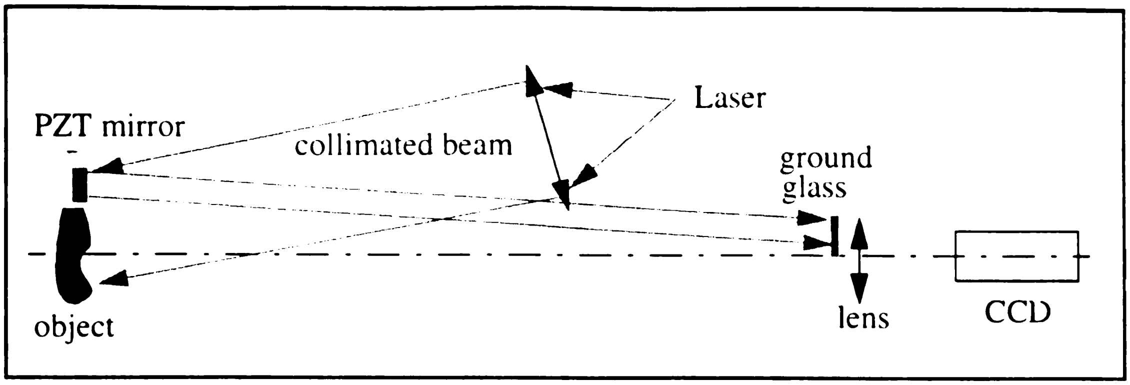

Fig. 2.8 Off-axis setup using a ground glass to produce a scattered reference beam.

Another off-axis reference beam arrangement which uses a ground glass as an image screen was reported by Joenathan and Torroba [1991a]. The schematic is depicted in Figure 2.9. An obvious disadvantage of this system is that it is difficult to make it compact.

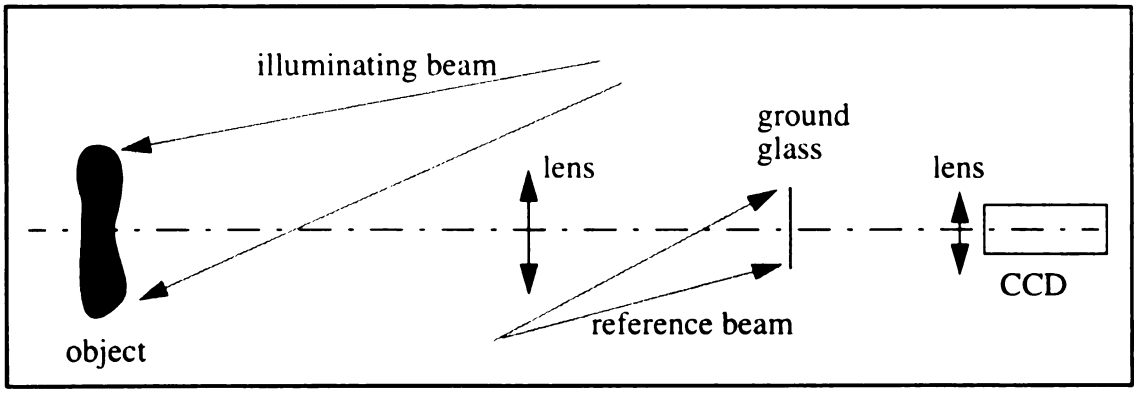

Fig. 2.9 Off-axis setup using a ground glass as the image plane.

2.6.2 In-plane displacement sensitive ESPI

In-plane sensitive ESPI measures the in-plane displacements. It is achieved by arranging two illuminating beams to meet at the image plane, normally, the target of a CCD camera. These two illuminating object beams are incident on the object at equal angles from the optical axis of the imaging system. Some in-plane sensitive setups are illustrated in Figures 2.10 through 2.12. For setups with collimated beams, see Figure 2.10 and 2.11, the phase change due to the out-of-plane displacement component will be cancelled out between the two beams. There is no contribution from the out-of-plane displacement. The in-plane displacement component d_x is measured by arranging the two illuminating beams in the x-z plane, and the phase change due to d_x is given by,

$$\Delta\phi = \frac{4\pi}{\lambda} d_x \sin\theta \tag{2.9}$$

where θ is the angle between the illuminating beam and the optical axis. The in-plane displacement component d_y can be measured if we arrange the illuminating beams in the y-z plane. From equation 2.9, one notices that the in-plane sensitivity may be changed by using different illumination angles.

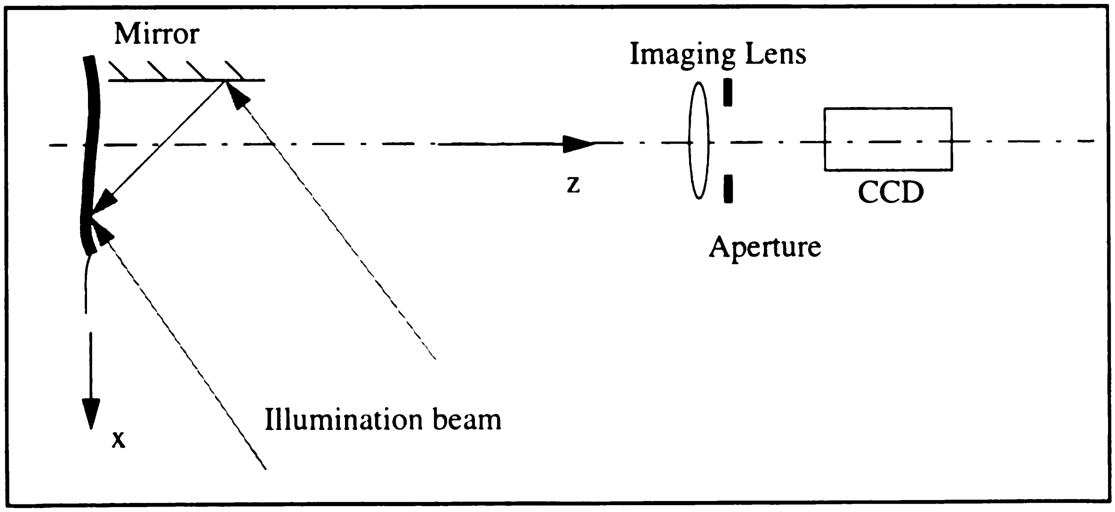

Fig. 2.10 In-plane sensitive setup with one collimated beam.

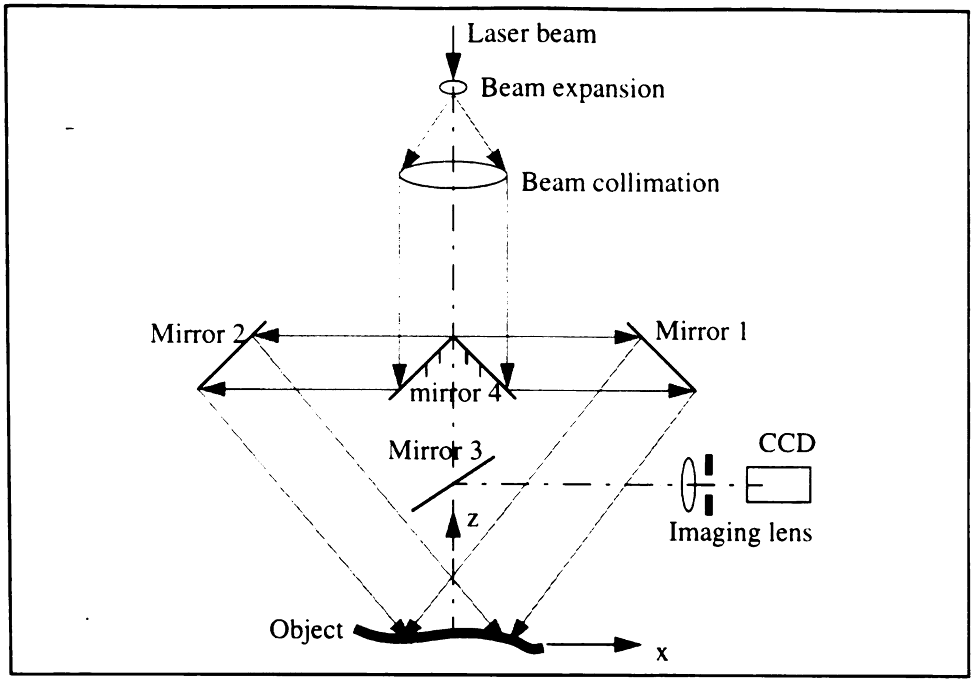

Fig. 2.11 In-plane sensitive setup with two collimated illuminating beams

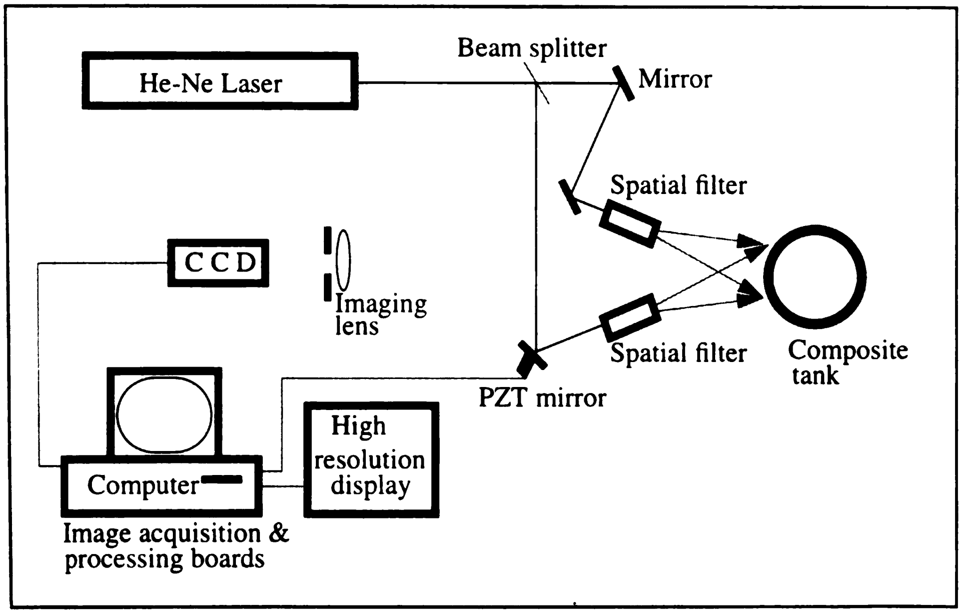

Fig. 2.12 In-plane sensitive setup with two diverging illumination beams.

The setup in Figure 2.12 is a practical setup which is often used. In this setup, diverging beams are used to illuminate the object. Therefore, the out-of-plane displacement-induced phase change will not be totally canceled out between the two beams. The observed fringes are produced by a combination of the in-plane and the out-of-plane displacement components, although the contribution of the out-of-plane displacement may be quite small compared with that of the in-plane displacement.

Other goals in optical system design are to reduce the effects of environmental disturbances on the optical paths. A system which uses feedback control to compensate environmental disturbances and rigid body motions was reported by Sciammarella et al [1993]. Joenathan and Khorana [1993] reported a quasi-equal-path ESPI setup which used a plano-concave lens to provide a reference beam in front of the test object. Phase-stepping was achieved by translating the plano-concave lens.

The trend of the development of the optical systems is towards (1) use of fiber optics and diode lasers to make the system more compact and rugged, (2) multi-functional, (3) more user friendly, (4) better image processing software, (5) fast, and (6) insensitive to environmental disturbances [Albertazzi 1993; Galanulis and Ritter 1993; Sciammarella et al 1993]. To increase the measurement range of ESPI for large deformation measurement, two-wavelength ESPI may be used [Gülker et al 1992].

2.7 ESPI Using Fiber Optics

Fiber optics is becoming widely used in ESPI and ES systems because of advances in optical fibers and the techniques of coupling laser energy into optical fibers. The motivation of using fiber optics in these systems is the following:

- The use of fiber optics can substantially reduce the number of required prisms, mirrors and lenses, etc., and therefore, directly simplify the optical setup, enhance the stability, and reduce the size and weight of the system.
- All unexpanded laser beams are enclosed, making the system inherently safe for, especially, non-skilled users.
- By using in-line connectors and appropriate directional couplers, it is possible to construct a fiber optic system which can use a range of laser sources, and the sources can be changed simply by connecting a fiber optic launched laser into the ESPI system. No adjustments to the optics are necessary, as the fiber optic system remains fully aligned independently of the laser used. This produces a very flexible system. The laser may be placed far away from the rest of ESPI unit.
- Phase-shifting techniques can be applied with low-voltage, thereby eliminating the need for an intermediate high-voltage amplifier.

The first successful demonstration of the use of fiber optics in the study of vibrating objects by time-averaged holographic interferometry was reported by Dudderar et al [1985]. Some applications of using fiber optics in ESPI have been reported by several researchers [Joenathan and Khorana, 1990, 1992a; Peng et al, 1992; Liu et al, 1990, 1992].

Single mode fiber (SMF) and coherent multimode fiber (MMF) may both be used. Overall, SMF offers much better results than does MMF [Taniguchi, Oki, and Takagi 1991]. SMF has been successfully used to carry both object beam and reference beam. SMF is mechanically stable and offers uniform output. The shortcomings are difficulty in coupling the laser radiation into the fiber and low coupling efficiency. The advantages of MMF are ease of coupling and high coupling efficiency. The disadvantages are that the output is speckled and it is susceptible to mechanical disturbances.

When using fiber optics in optical interferometry including ESPI and ES, the following points should be considered.

- If a diode laser is used, an optical isolator may be needed between the laser diode and the launching optics to reduce the back-reflection from the fiber end and ensure single mode oscillation of the diode laser [Andonovic and Uttamchandani 1989; Ohtsu 1992].
- Optic fiber ends should be polished and anti-reflective (AR) coated to reduce back reflection.
- To reduce temperature effects, fiber lengths of reference and object should be kept as close as possible.
- Temperature and mechanical stress can change the phase of the optical wavefront in the fiber.
- When MMF is used, an introduction of a turn of the fiber can substantially suppress the high modes propagating in the fiber. The optimum radius should be determined by trials.
- To couple the laser radiation into the optic fiber, a launching optic device is used. If a diode is used, the output beam should first be collimated and then coupled into the fiber. A tiny graded refraction index (GRIN) lens may be used for the coupling.
- A way to control the ratio of object beam to reference beam is always desired.
- Single-mode fiber can act as a spatial filter, so no additional spatial filters are needed.

A number of fiber optic versions of ESPI optical setups are illustrated in Figures 2.13 through 2.15. Some of these designs follow quite similarly those by Joenathan and

Khorana [1990, 1991, 1992a].

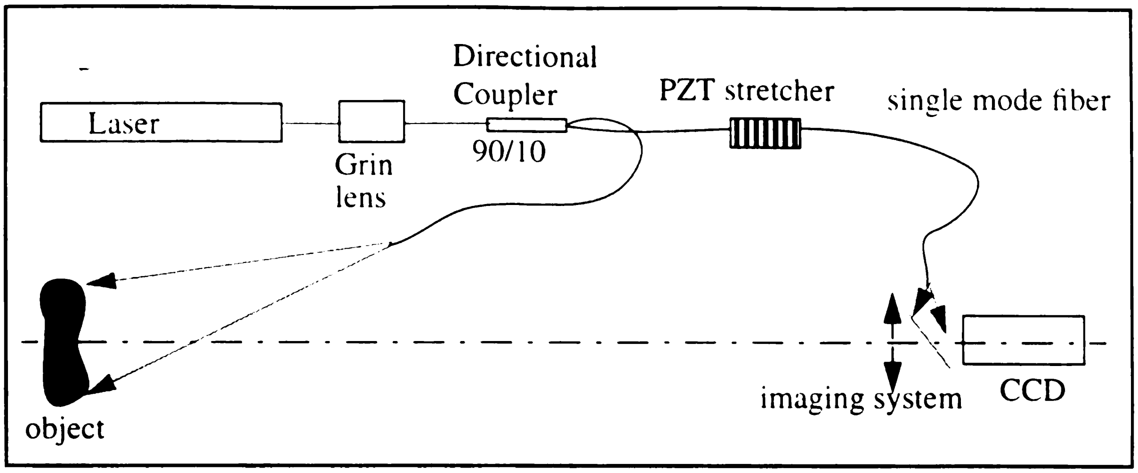

Fig. 2.13 On-axis fiber optic ESPI optical setup.

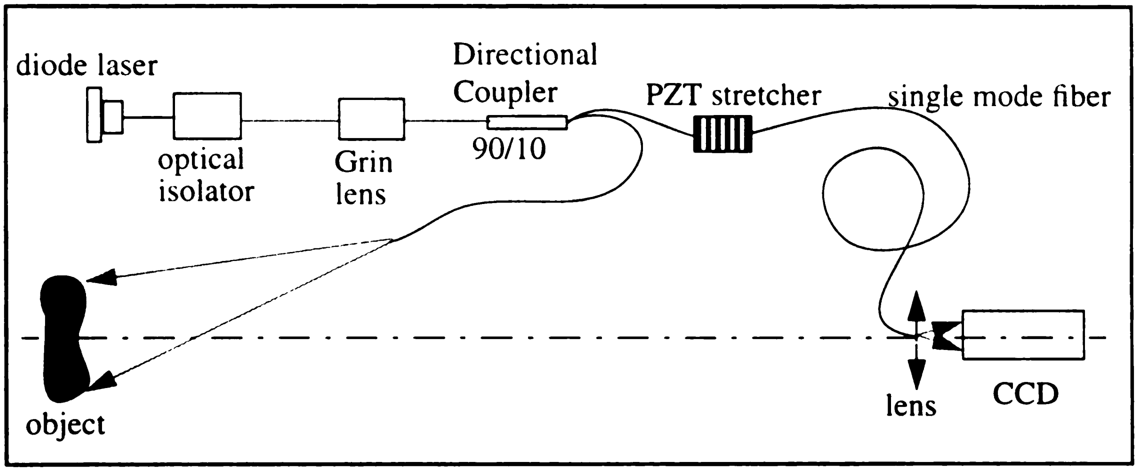

Fig. 2.14 On-axis fiber optic ESPI optical setup using a diode laser.

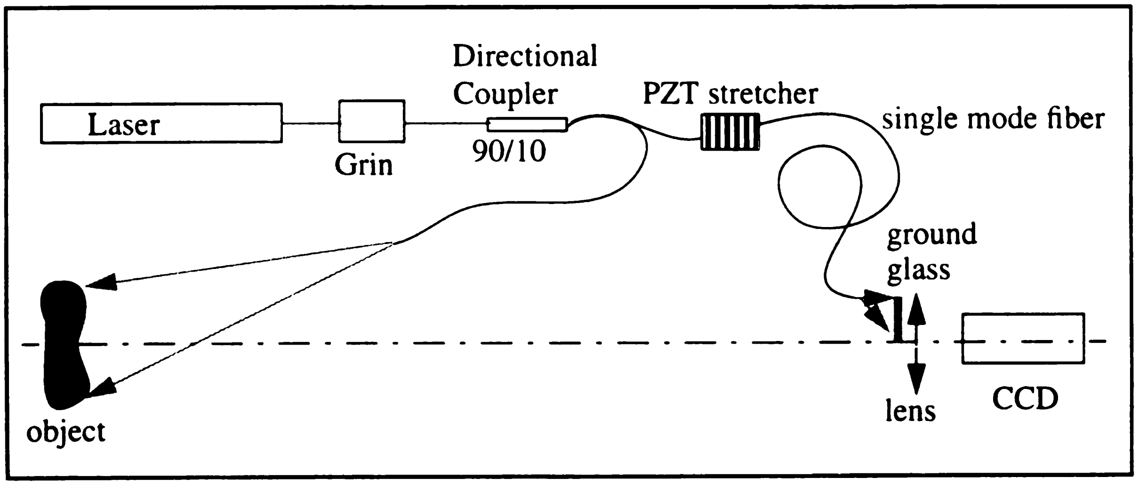

Fig. 2.15 Off-axis fiber optic ESPI optical setup.

An application of fiberized ESPI in the automotive industry was reported by Davies and Buckberry [1989]. In their application, a 600mW argon ion laser was linked to the optical head of an ESPI system by a 40 meters-long optic fiber. The frequency modulation capability of a diode laser can be used to obtain automatic deformation measurements using phase-shifting techniques [Kato et al 1993].

2.8 Some practical issues

(1) Object sizes under test

The maximum area which can be inspected in one view is limited by the laser power available and the sensitivity of the receiving device (normally a CCD). But as the size of the object, especially the depth of the object, increases, the mechanical stability of the measuring setup and the coherence of the laser should also be considered.

A relatively large deforming force must be applied in order to observe fringes on a small area caused by mechanical loading, and this is likely to give rise to rigid body translations and rotation, which cause speckle decorrelation and hence a reduction in fringe visibility. Decorrelation and memory loss (essentially decorrelation) for given in-plane translations and rotations increase as the magnification of the viewing system is increased. Decorrelation of the speckles can cause a reduction in fringe visibility and this is more likely to occur when ESPI is used at high magnification.

Because the ESPI system must use a high *f*-number (small aperture) viewing system, the depth of field of the system is high, so the depth of field is generally not a restriction.

(2) Object surface condition and treatment

When the light scattering ability of the test object is weak, as is normal for an object having a dark surface, the object surface may treated to increase scattering by spraying the surface lightly with white paint, wheat flour, or baby powder. This is especially true when in-plane displacement is being measured using double illumination interferometry. Owing to the high angles of incidence of the two illuminating beams, it is evident that the surface being studied must be totally diffusing, with no enhanced scattering in the specular direction.

The surface under examination should not alter microscopically during the course of the measurement. If it does so, through oxidation, re-crystallization, or other factors, decorrelation of the speckle will result. This can totally eliminate the fringes.

(3) Polarization problem

Since the measurement of phase information relies upon the formation of interferometric fringes formed by the constructive and destructive interference between the object and reference beams, the light in the two beams should have the same polarization. Laser beams polarized orthogonally to each other will not interfere. If the beams are not in the same plane the fringe visibility will be reduced. Most lasers are linearly polarized and this can, in some instances, cause problems in recording speckle patterns. Although both beams are derived from the same source, polarization changes can occur as a result of reflections or scattering. Fortunately, most diffuse objects scatter light in randomly polarized fashion, and there will always be components having the same polarization as the reference beam. In our study, we found that carbon and glass fiber composites do not depolarize light; the light scattered has the same polarization as the reference light. Light scattered from white carton board will be partially depolarized. If a polarization problem exists, it can be rectified by some optical methods or by surface treatment.

(4) Optimization of light intensity

For a given type of video camera, a certain minimum intensity is required to create a voltage output which can be detected above the background electronic noise. An increase in the incident intensity gives an increased output voltage from the camera until the intensity reaches the camera saturation level, beyond which the output voltage remains constant for any further increase in incident intensity.

The intensity of the speckle pattern varies randomly across the image, and, to avoid losing information from the speckle pattern, the overall intensity should be below the saturation level of the camera for all of the useful picture area. If the mean value and the standard deviation of the speckle pattern are given by $\langle I_t \rangle$ and σ_t, then, when

$$\langle I_t \rangle + 2\sigma_t < I_{sat} \tag{2.10}$$

the intensity will be less than the saturation level of the camera for 95% of the image. Here I_{sat} is the camera's saturation intensity [Jones & Wykes, 1989].

The amount of light collected by the CCD device is inversely proportional to the *f*-number of the imaging system. The optimum setting is determined by the laser power available, the scattering properties of the object surface, the spatial resolution and the sensitivity of the video system. There is a trade-off between the speckle size and the amount of light passing through the imaging lens. Actually, speckles do not need to be fully resolved by the CCD device to produce acceptable fringe patterns. Experimentally, we have found that an *f*-number which is 1/3 smaller than the one theoretically required still can give satisfactory fringe visibility. This is in agreement with the analysis by Wykes [1987]. Similar results were also obtained by Owner-Petersen [1991b] with the considerations of speckle decorrelation. In practice, we derived an empirical formula which may be used to determine the minimum value of the *f*-number. This formula is expressed by

$$F = \frac{S_{CCD}}{3.66(1+M)\lambda} \tag{2.11}$$

where F is the *f*-number, S_{CCD} is the size of a single sensing element in the CCD sensing array, M is the magnification of the imaging lens, and λ is the wavelength.

For the case of a smooth reference beam and a speckled object beam as in out-of-plane sensitive ESPI, the optimal reference-to-object intensity ratio is determined by the optical and electronic noise. The optimum is obtained by increasing the reference-to-object intensity ratio until the optical object noise is reduced to the level of the optical reference noise. However, this optimum setting will be modified by the electronic noise. When the electronic noise is much larger than the optical noise, the optimum will be determined by the electronic noise. For example, under fully resolved speckle condition, the maximum signal to noise ratio (SNR) is obtained when we have the object beam intensity $I_o = 0.15 I_{sat}$ and $I_r = 1.7 I_o$ [Wykes 1987]. In fact, a reference-to-object ratio much greater than one, say 5:1, may be used. In this case, a 50% reduction in the aperture will not affect the final result in a significant way. To illustrate this point, Figure 2.16 and Figure 2.17 are the output interferograms from our CCD camera at aperture settings *f*/11 and *f*/22 respectively. The mean intensities for aperture settings 11 and 22 are 150.5618 and 147.8826 respectively.

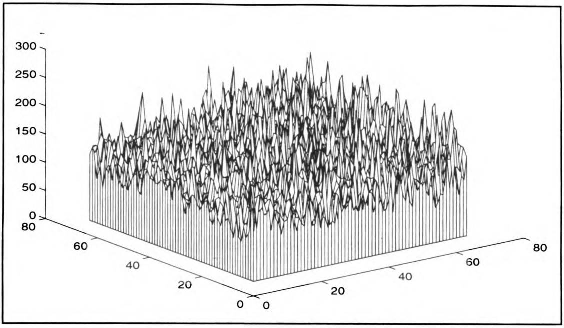

Fig. 2.16 Interferogram at aperture setting *f*/11.

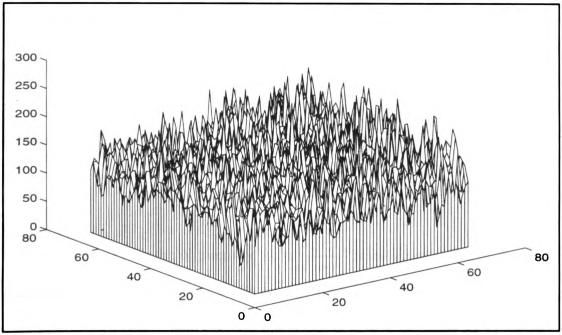

Fig. 2.17 Interferogram at aperture setting *f*/22.

When two speckled beams are employed as in an in-plane sensitive ESPI setup or in electronic shearography, the mean intensities of the two beams at the image plane should be equal, and the combined peak intensities should be just below the camera saturation intensity.

2.9 Automatic quantitative fringe analysis

To determine the quantitative surface deformation of the object using ESPI, phase measuring techniques are used. Specifically, the temporal phase measurement method is normally used. The phase measuring technique directly measures the wavefront phase in an interferometer corresponding to the relative difference between the object and reference optical paths. The technique has been known for almost thirty years [Carré 1966; Bruning et al. 1974; Hariharan et al 1982; Robinson 1983; Creath 1985]. A rather comprehensive presentation of this technique was given by Creath [1988].

For convenience, equation 2.1 is rewritten in the following form

$$I = I_0[1 + \gamma_0 \cos\phi_0] \tag{2.12}$$

after deformation/displacement, we have

$$I = I_0[1 + \gamma_0 \cos\phi] \tag{2.13}$$

where $I_0 = I_r + I_o$ is the dc intensity, $\gamma_0 = \frac{2\sqrt{I_r I_o}}{I_r + I_o}$ is the fringe visibility, ϕ_0 is the initial phase between the two beams, and $\phi = \phi_0 + \Delta\phi$ is the phase between the two beams after deformation. There are three unknowns in each of the above two equations, namely, I_0, γ_0 and ϕ_0 or ϕ. In order to obtain the displacement-induced phase change $\Delta\phi$, three equations at each stage are required for solving for the phases ϕ_0 and ϕ. To obtain these equations, phase-stepping or phase-shifting techniques are used. The idea is to introduce a number of known phase changes in one of the two beams which interfere with each other, and then record the corresponding interferograms (TV frames). The known phase changes are normally introduced in the reference beam for convenience. Let α_i be the amount of phase change introduced into one of the beams, Eq. (2.12) becomes

$$I = I_0[1 + \gamma_0\cos(\phi_0 + \alpha_i)] \tag{2.14}$$

Note that there is no upper limit for the number of α_i introduced. The least number is three for a complete solution. I_0, γ_0 and ϕ_0 are assumed unchanged during the phase measurement process. This assumption is satisfied by maintaining a constant laser output and a stable environment during measurement.

After $\Delta\phi$ is obtained, "phase unwrapping" is performed to remove modulo 2π phase discontinuity. Finally, the entire displacement map of the object is obtained. Phase shifting and phase unwrapping techniques will be discussed in the following sections. In the case of parallel illumination and observation, the out-of-plane displacement is given by

$$\Delta d_s = \frac{\lambda}{4\pi}\Delta\phi. \tag{2.15}$$

2.9.1 Phase-stepping and phase-shifting methods

Phase measurement can be carried out in two different ways in terms of introducing phase changes. The first is: (1) the phase-stepping method, as shown in Figure 2.16, where a number of discrete phase steps are used so that the phase is constant during each TV-frame. The second is the phase-shifting method, as shown in Figure 2.18, where the phase is linearly and continuously shifted during each TV-frame. There is a difference between these two techniques. Detectors do not measure instantaneous irradiance, they measure time-averaged irradiance. In the case of the phase-stepping method, the modulation phase is constant during each TV frame as shown in Figure 2.18(a). In the phase-shifting method, the modulation phase is not static, it is linearly ramping during each TV frame time as shown in Figure 2.18(b). As a consequence, the intensity in the phase shifting method is modulated by a sine function as shown in Figure 2.19.

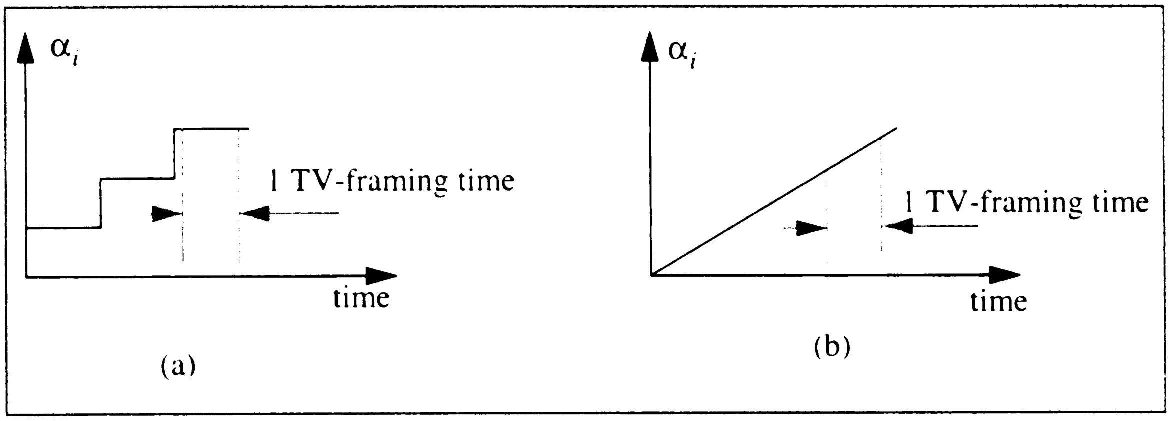

Fig. 2.18 Schematic of phase-stepping and phase-shifting.

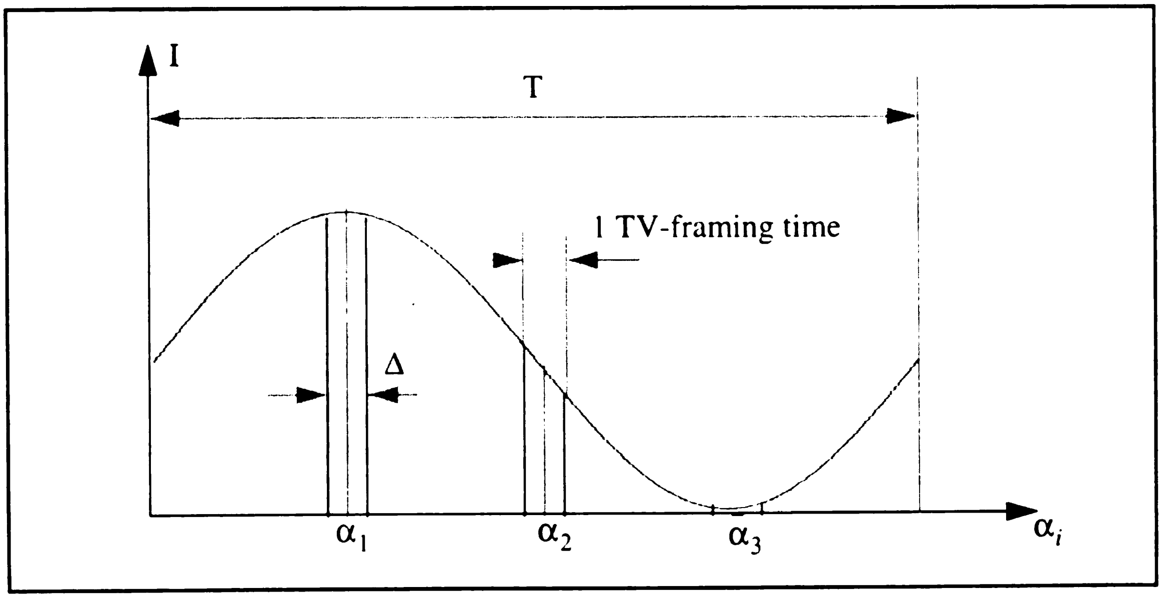

Fig. 2.19 Intensity modulation due to phase-shifting.

In Figure 2.19, T is the modulation period, Δ is the amount of phase-shifting in one TV-frame about a center phase value α_i.

Due to phase-shifting, the average intensity integrated during one TV frame is given by

$$\begin{aligned} I_i &= \frac{1}{\Delta}\int_{\left(\alpha_i-\frac{\Delta}{2}\right)}^{\left(\alpha_i+\frac{\Delta}{2}\right)} I_0[1+\gamma_0\cos(\phi_0+\alpha_i)]d\alpha \\ &= I_0\left[1+\gamma_0\left(\operatorname{sinc}\left(\frac{\Delta}{2}\right)\cos(\phi_0+\alpha_i)\right)\right] \\ &= I_0[1+\gamma\cos(\phi_0+\alpha_i)] \end{aligned} \tag{2.16}$$

where γ is the modified fringe visibility. In comparing equation 2.14 and equation 2.16, we note that the only difference between integrating the phase and stepping the phase is a reduction in the fringe visibility. When $\Delta = 0$, equation 2.16 becomes equation 2.14. If Δ increases, $\operatorname{sinc}\left(\frac{\Delta}{2}\right)$ decreases. When $\Delta = 2\pi$, there would be no modulation of the intensity. Apart from this difference, a time delay is required between steps in the phase-stepping method to damp out any oscillation caused by the sudden steps in phase. Therefore, phase-stepping is slower than the phase-shifting technique.

We will see, in the following section, that the intensity and the fringe visibility terms cancel out in the phase calculation. Therefore, the real effect of the visibility reduction is to reduce the measurement signal-to-noise ratio (SNR), which may have an effect on the subsequent phase unwrapping.

2.9.2 Phase extraction algorithms

As mentioned before, N (N>3) number of frames may be used to determine all the phase information. Many algorithms for extracting the phase have been developed. Generalized algorithms can be derived from the least-squares method [Greivenkamp 1984; Morgan 1982; Lai & Yatagai, 1991]. Some of the commonly used algorithms are summarized below.

(1) Three-frame techniques

(a) For a three discrete phase-stepping method [Wyant et al. 1984; Bhushan et al, 1985], one substitutes $\alpha_i = \frac{\pi}{4}, \frac{3\pi}{4}$, and $\frac{5\pi}{4}$ (i = 1, 2, 3) into equation 2.14, respectively, to obtain three equations,

$$I_1 = I_0\left[1 + \frac{\sqrt{2}}{2}\gamma_0(\cos\phi - \sin\phi)\right] \tag{2.17}$$

$$I_2 = I_0\left[1 + \frac{\sqrt{2}}{2}\gamma_0(-\cos\phi - \sin\phi)\right] \tag{2.18}$$

$$I_3 = I_0\left[1 + \frac{\sqrt{2}}{2}\gamma_0(-\cos\phi + \sin\phi)\right] \tag{2.19}$$

Solve the above three equations for ϕ to obtain

$$\phi = arc\tan\left(\frac{I_3 - I_2}{I_1 - I_2}\right) \tag{2.20}$$

Note that only the intensities are involved in the determination of phase information. During this process, the fringe visibility γ_0 is also calculated for use later in the phase unwrapping process. γ_0 is given by

$$\gamma_0 = \frac{\sqrt{(I_3 - I_2)^2 + (I_1 - I_2)^2}}{\sqrt{2}I_0} \tag{2.21}$$

(b) For the corresponding phase-shifting method, as mentioned previously, the difference is a reduction in the fringe visibility. Phase ϕ is calculated using the same equation 2.20. Suppose $\frac{\pi}{2}$ is chosen as the phase shift per frame, then $\Delta = \frac{\pi}{2}$. The modified fringe visibility γ becomes, from equation 2.21

$$\gamma = \mathrm{sinc}\left(\frac{\Delta}{2}\right)\gamma_0 = \frac{\sin\left(\frac{\pi}{4}\right)}{\frac{\pi}{4}}\gamma_0 \approx 0.9\gamma_0 \tag{2.22}$$

The visibility reduction is 10%.

Other values of α_i can also be used. For example, when $\alpha_i = 0, -\frac{\pi}{2}$, and $\frac{\pi}{2}$, ϕ will be given by

$$\phi = arc\tan\left(\frac{I_3 - I_2}{2I_1 - I_1 - I_3}\right). \tag{2.23}$$

γ will also take a different form.

(2) Four-frame technique

In this case, α_i takes the values of 0, $-\frac{\pi}{2}$, π, and $\frac{3\pi}{2}$. Following the same procedure as in the three-frame technique, the phase ϕ and the fringe visibility γ_0 can be expressed as

$$\phi = arc\tan\left(\frac{I_4 - I_2}{I_1 - I_3}\right), \qquad (2.24)$$

and

$$\gamma_0 = \frac{\sqrt{(I_4 - I_2)^2 + (I_1 - I_3)^2}}{2I_0}. \qquad (2.25)$$

Again, if the phase is integrated over a $\frac{\pi}{2}$ phase shift per frame, $\Delta = \frac{\pi}{2}$. We have, for a corresponding phase-shifting technique, $\gamma \approx 0.9\gamma_0$. This algorithm was implemented in ESPI out-of-plane and in-plane, and in ES by Nakadate and Saito [1985].

(3) Five-frame technique

This is the commonly used algorithm implemented in some commercial interferometers [Surrel 1993]. The algorithm was developed by Hariharan et al [1987] to reduce phase calibration errors and errors due to deviation from linearity of the phase-shifting device. When α_i takes the values of $-\pi$, $-\frac{\pi}{2}$, 0, $\frac{\pi}{2}$, and π, the phase and the visibility may be expressed as,

$$\phi = arc\tan\left[\frac{2(I_2 - I_4)}{2I_3 - I_1 - I_5}\right] \qquad (2.26)$$

$$\gamma_0 = \frac{\sqrt{[2(I_2 - I_4)]^2 + (2I_3 - I_1 - I_5)^2}}{4I_0} \qquad (2.27)$$

(4)

Kno

inde

Exa

Cre

The

Solving

Note that th

(4) Carré technique

In all the previous phase calculation algorithms, the introduced phase values α_i are known and the phase shifter is calibrated to generate those values. A technique which is independent of the magnitudes of the phase changes was developed by Carré [1966]. Examples of using this algorithm can be found in the papers by Chang et al [1985] and by Creath [1985]. This technique uses four frames with a phase change of $\delta\alpha$ between them. The four equations are

$$I_1 = I_0\left[1 + \gamma\cos\left(\phi - \frac{3\delta\alpha}{2}\right)\right] \tag{2.28}$$

$$I_1 = I_0\left[1 + \gamma\cos\left(\phi - \frac{\delta\alpha}{2}\right)\right] \tag{2.29}$$

$$I_1 = I_0\left[1 + \gamma\cos\left(\phi + \frac{\delta\alpha}{2}\right)\right] \tag{2.30}$$

$$I_1 = I_0\left[1 + \gamma\cos\left(\phi + \frac{3\delta\alpha}{2}\right)\right] \tag{2.31}$$

Solving the above equations, we obtain for the phase and fringe visibility

$$\phi = arc\tan\frac{\sqrt{(I_1 + I_2 - I_3 - I_4)[3(I_2 - I_3) - (I_1 - I_4)]}}{I_2 + I_3 - I_1 - I_4} \tag{2.32}$$

$$\gamma = \frac{1}{2I_0}\sqrt{\frac{(I_1 + I_2 - I_3 - I_4)^2 + (I_2 + I_3 - I_1 - I_4)^2}{2}}\,. \tag{2.33}$$

Note that this algorithm assumes that $\delta\alpha$ is near $\frac{\pi}{2}$ and it requires that the phase mod

non-

disad

phase

D

enviro

condi

numbe

compu

in phas

Be

speciai

Schwid

deviatio

calculat

miscalib

obtain ac

A numbe

Creath 19

A sub

shifted by

changing th

frequency c

second), the

modulation is linear with time. The Carré technique has the advantages of working with a non-parallel beam where the amount of phase shift varies across the beam. The disadvantage is that the phase calculation is more complicated and the determination of phase modulo 2π is more involved [Creath 1985].

Determining which one of the algorithms to use depends upon the measurement environment, the phase-shifting device, and the optical layout. If the measurement condition is unstable or if the application is time dependent, the technique with the fewest number of measurements is preferred. Because the signal-to-noise ratio (SNR) of the computed phase increases as $\sqrt{N}$ [Bruning 1987], where N is the number of frames used in phase calculation, the errors tend to be minimized when more frames are used.

Besides the algorithms described above, there are other algorithms, each with its own special abilities. A new compensating four-frame algorithm was recently reported by Schwider et al [1993], and it can eliminate the errors caused by linear adjustment deviations of the reference phase in the interferometer. Another recently developed phase calculation algorithm can eliminate most of the errors caused by phase-shifter miscalibration and has the possibility of achieving high SNR [Surrel 1993]. However, to obtain accurate phase measurement, the phase shifting device should always be calibrated. A number of workers have made contributions in this area [e.g. Cheng and Wyant 1985; Creath 1988].

A subtle point may be worth comment. In the phase-shifting techniques, the phase is shifted by, for example, translating a mirror. When the mirror is moving, apart from changing the phase of the beam, it will also cause a Doppler effect which changes the frequency of the light. However, because the speed of the mirror is rather slow (~8λ per second), the phase change due to Doppler effect over one meter is only about $6x10^{-5}$

deg

the l

the t

into

where

frequ

The s

inform

freque

amoun

the tec

the loc

decide

2.9.3 P

To i

introduc

transduc

plate [Cr

using fibe

degree, and it can be neglected.

Note that phase measurement can also be realized through changing the frequency of the light [Wizinowich 1990; Kato, Yamaguchi, and Ping 1993]. In the above discussion, the time term in the interference equations has been omitted. Inserting the time term back into equation 2.2, we obtain

$$I = I_0[1 + \gamma_0\cos(\phi + \omega t)] \tag{2.34}$$

where ω is the angular frequency of the light. For the frequency shifting technique, the frequency ω is varied to introduce a phase difference between the two interfering beams. The same phase calculation algorithms can be employed to calculate the phase information as in the optical path-length modulation technique. A problem with the frequency-shifting technique is that the introduced phase change depends not only on the amount of frequency shift, but it also depends on the optical path-lengths, and this makes the technique inconvenient. To avoid this difficulty, a technique was developed to detect the local intensity of interference fringes through a fixed window as a phase-shift signal to decide the recording time of the fringe pattern [Kato et al., 1993].

2.9.3 Phase-shifting devices

To implement phase measurement techniques, some type of device is necessary to introduce the phase changes. A number of ways may be used, such as a piezoelectric transducer (PZT) mirror, polarization phase shifter [Jin and Tang, 1992], or a tilting glass plate [Creath 1988]. Of these possibilities, PZT-mirrors are most widely used. In ESPI using fiber optics, the phase shifting is normally carried out by stretching the fiber. To do th

ap

2.9

calc

to be

assig

for an

Aft

The purp

modulo

corrected

phase grad

this, the fiber is wrapped on a PZT cylinder or disk which expands when a voltage is applied [Joenathan and Khorana, 1992a].

2.9.4 Phase unwrapping

First, the modulo 2π phase has to be resolved. When the phase information is calculated, because of the nature of the trigonometry functions, the modulo 2π phase has to be obtained by considering the signs of sine and cosine functions. The criterion for assigning the calculated phase to one of the four quadrants are illustrated in Figure 2.20 for all algorithms except for the Carré technique [Creath 1985].

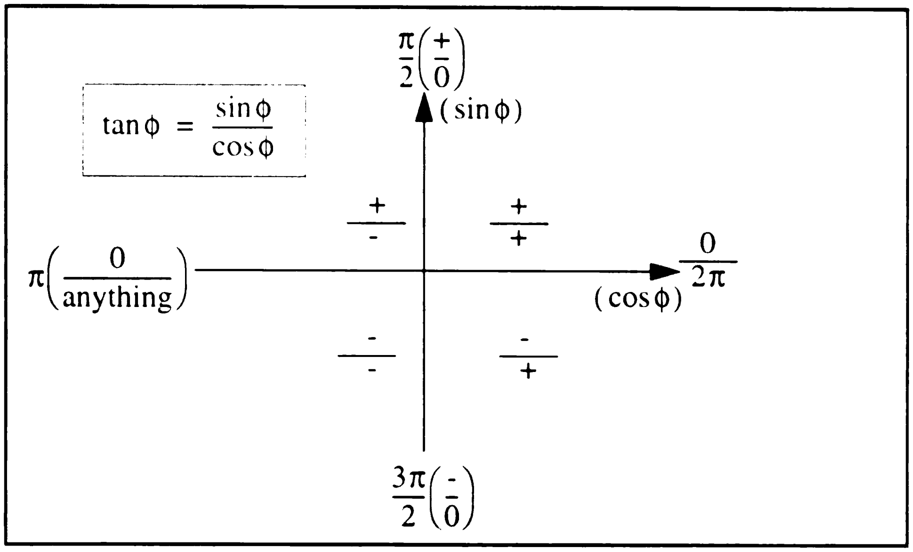

Fig. 2.20 Phase modulo 2π determination.

After the modulo 2π phase is obtained, phase unwrapping can then be carried out. The purpose of phase unwrapping is to remove the phase ambiguities owing to the phase modulo 2π calculation [Ghiglia, Mastin, and Romero 1987]. The phase ambiguities are corrected by comparing the phase difference between adjacent pixels. At each pixel the phase gradient is calculated by taking the phase difference between it and its neighboring data po

where

thresho

adding

then is

entire p

an exag

we can

unwrap

For

pixels m

way of k

shows ar

data point:

$$\Delta\phi_{mn} = \phi_{mn} - \phi_{m(n-1)} \tag{2.35}$$

where m is the row number and n is the column number. If $|\Delta\phi_{mn}|$ is greater than a certain threshold (normally π), then a fringe edge is detected. This phase jump is corrected by adding or subtracting 2π to make the difference less than π. A fringe order number N then is recorded such that the phase at that point is given by $\phi_{mn} + 2N\pi$. Finally, the entire phase map is obtained by counting all of the unwrapped fringes. Figure 2.21 shows an exaggerated illustration of phase unwrapping and fringe counting. From equation 2.35, we can see that various scanning paths (horizontal, vertical...) may be used for phase unwrapping.

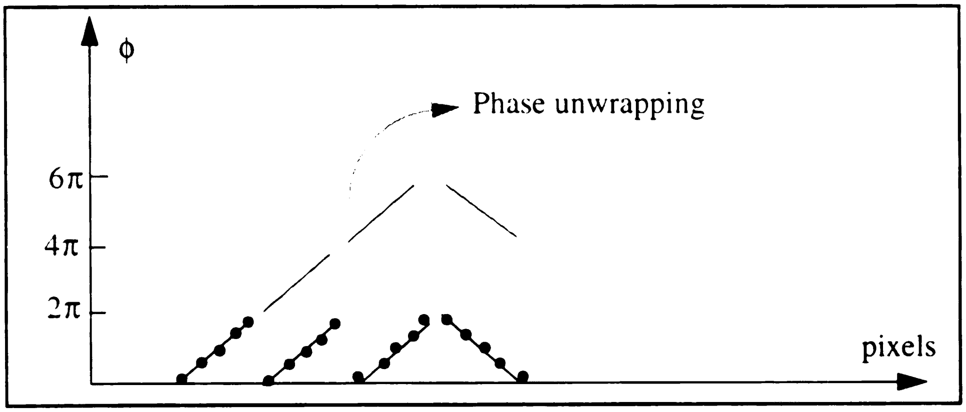

Fig. 2.21 An illustration of phase unwrapping.

For reliable removal of the ambiguities, the phase difference between two adjacent pixels must be less than π. If the difference is greater than π, for some cases, we have no way of knowing if the angle has progressed clockwise or counterclockwise. Figure 2.22 shows an illustration of this ambiguity.

The
accurat
adequat
line by
subtract
present
Noise ca
sampling
addition
the desig

In or
before g
can resul
very imp
median fil
the data.
informatio

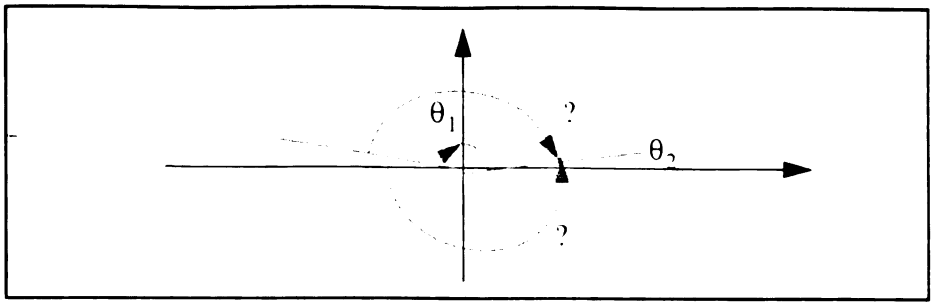

Fig. 2.22 π phase ambiguity between two adjacent pixels.

The most important factor for reliable and accurate phase unwrapping algorithms is to accurately recognize the 2π phase jumps. If the raw phase data is free of noise and is adequately sampled, then accurate phase unwrapping will easily be achieved. A simple line by line scan through the data will be adequate to integrate the phase by adding or subtracting 2π at the phase jumps. Unfortunately, in most real applications, noise is present in the raw phase data. This noise can result in false detection of phase jumps. Noise can come from electronics, optical components, low modulation, violation of the sampling theorem, and environmental disturbances (air turbulence, vibration...). In addition to noise, physical holes and other discontinuities may also bring difficulties into the design of the phase unwrapping algorithms.

In order to eliminate uncertainties as much as possible, data-conditioning is necessary before going to the phase unwrapping process. Good preparation of the raw phase data can result in simple and fast phase unwrapping algorithms. Thus, data preprocessing is very important just like the pre-processing in a finite element analysis. Low-pass filtering, median filtering, FFT, and identification of poorly modulated pixels are used to improve the data. Low-pass filtering smooths the data, but it can also cause loss of useful information [Vikhagen, 1991]. The choice of filter will always be a compromise between

noise s
be flag
pixels
perforn

Th
autom
as the
to the b
the dat
unwrap
phase g

Sor
and Be
Maas [
step wa
algorith
comput
overloo

2.9.5 D

As d
section p
an ESPI

noise suppression and the elimination of valid fringe data. Poorly modulated pixels may be flagged as being invalid data and ignored in the phase unwrapping process. The flagged pixels can be replaced with a local average of valid pixels by a smoothing process performed on the final unwrapped phase data.

The starting point for phase unwrapping may be selected either manually or automatically. The center of the largest area with good modulated data is normally chosen as the starting point. Typically, the 2D array (pixels) is unwrapped from this starting point to the bottom of the frame and then from the starting point again to unwrap the top half of the data. Region by region unwrapping is also possible. Good regions should be unwrapped before trying to tackle the bad regions. Good regions are those with small phase gradient and low noise.

Some recent algorithms for unwrapping noisy phase data were reported by Quiroga and Bernabeu [1994], Andrä et al [1991], Owner-Petersen [1991c], and Vrooman and Maas [1991]. An interesting phase calculation algorithm which uses only a single-phase-step was developed for fast data acquisition [Kerr et al, 1990]. Experimentally, this algorithm showed a significant improvement in environmental stability and reduced computational effort. However, an obvious error in the derivation of the algorithm was overlooked and no explanation was given.

2.9.5 Data conditioning of the speckle images

As discussed in the above section, image data conditioning is very important. This section presents and discusses some image processing techniques which may be utilized in an ESPI system. Matlab software was used for the image processing presentations in this section.

Im

data to

images

images

so on.

noise.

and sub

operatio

Ima

namely

which a

can be

images.

the inte

spatial

looks n

brightne

reduce

Digi

images.

translate

center of

filtering o

section.

Image processing is a general term applied to a range of operations that alter frame data to extract more meaningful information. These processing techniques can manipulate images in a number of ways such as enhancing images, restoring images, combining two images, emphasizing or de-emphasizing details, highlighting edges, rotating images, and so on. In ESPI, image processing may be used to filter out unwanted components, remove noise, restore images, and detect fringe edges etc. For example, simple image addition and subtraction are used to extract useful information in time-average and real-time ESPI operations respectively.

Image processing operations can be classified into two broad categories [Jähne 1993], namely, those which are performed on individual pixels (pixel point processing), and those which are performed on groups of pixels (pixel group processing). Pixel point processing can be further divided into operations performed on a single image, and on two or more images. Note that both single image and multi-image pixel point processing affect only the intensity content of a frame, that is the frame can be made brighter or darker. The spatial content of the image is not changed. Pixel group processing, on the other hand, looks not just at the individual pixels, but also at the neighboring pixels to determine brightness trends. Trend information can be used in spatial filtering to emphasize or reduce image details and to enhance/restore images.,

Digital image filtering techniques is very important in the processing of ESPI and ES images. To implement a digital filtering process, the impulse response matrix is first translated into a convolution kernel by rotating the impulse response matrix 180^0 about the center of the matrix (if the matrix is symmetrical this process can be omitted). Then, the filtering operation is accomplished by a convolution process of the image matrix and the filter matrix. Mathematically, this process can be expressed by

$$\begin{aligned} B(n_1, n_2) &= A(n_1, n_2) \otimes k(n_1, n_2) \\ &= \sum_{l_1} \sum_{l_2} A(l_1, l_2) k(n_1 - l_1, n_2 - l_2) \end{aligned} \tag{2.36}$$

where $A(n_1, n_2)$ is the image matrix and $k(n_1, n_2)$ is the convolution kernel. l_1 and l_2 are the row and column numbers. Some examples of image filtering are illustrated below.

(1) Highpass filtering: Highpass filtering emphasizes the high-frequency components of a signal while reducing the low-frequency components. Because edges or fine details of an image are the primary contributors to the high frequency components of an image, highpass filtering often increases the local contrast and sharpens the image. The impulse response matrix of a highpass filter used for contrast enhancement is shown in Figure 2.23, and its frequency response is plotted in Figure 2.24.

-1	-1	-1
-1	9	-1
-1	-1	-1

Fig. 2.23 The impulse response of a highpass filter.

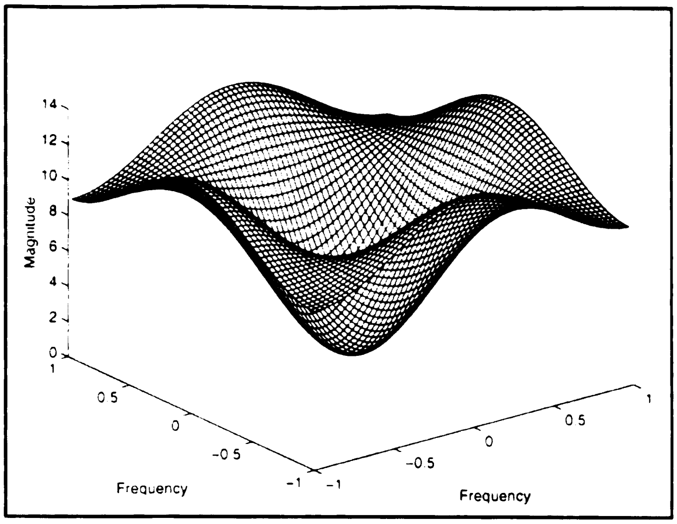

Fig. 2.24 The frequency response of the filter shown in Figure 2.23.

(2) Lowpass filtering: The energy of a typical image is primarily concentrated in its low-frequency components. This is due to the high spatial correlation among neighboring pixels. The energy of certain forms of image degradation, such as wideband random noise, is typically more spread out over the frequency domain. By reducing the high-frequency components while preserving the low-frequency components, lowpass filtering reduces a large amount of noise at the expense of a small amount of signal. Therefore, lowpass filtering may be used for noise smoothing. The impulse response of a typical lowpass filter is shown in Figure 2.25, and its frequency response is plotted in Figure 2.26.

$$\frac{1}{9} \bullet \begin{array}{|c|c|c|} \hline 1 & 1 & 1 \\ \hline 1 & 1 & 1 \\ \hline 1 & 1 & 1 \\ \hline \end{array}$$

Fig. 2.25 The impulse response of a lowpass filter.

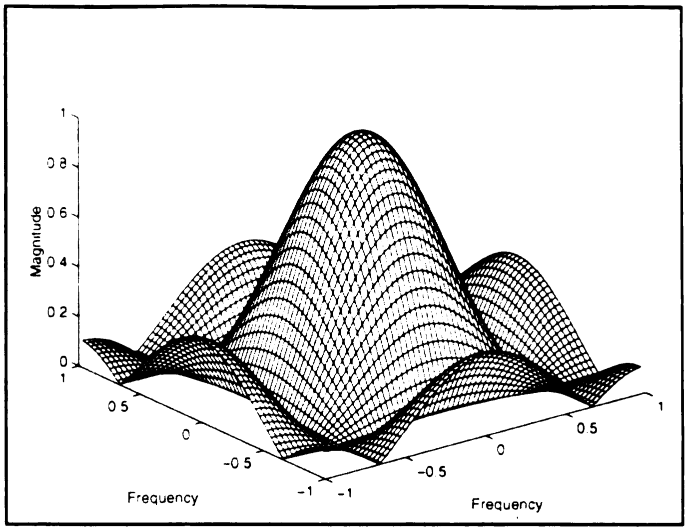

Fig. 2.26 The frequency response of the filter shown in Figure 2.25.

An example of the highpass and lowpass fringe filtering is shown in Figure 2.27.

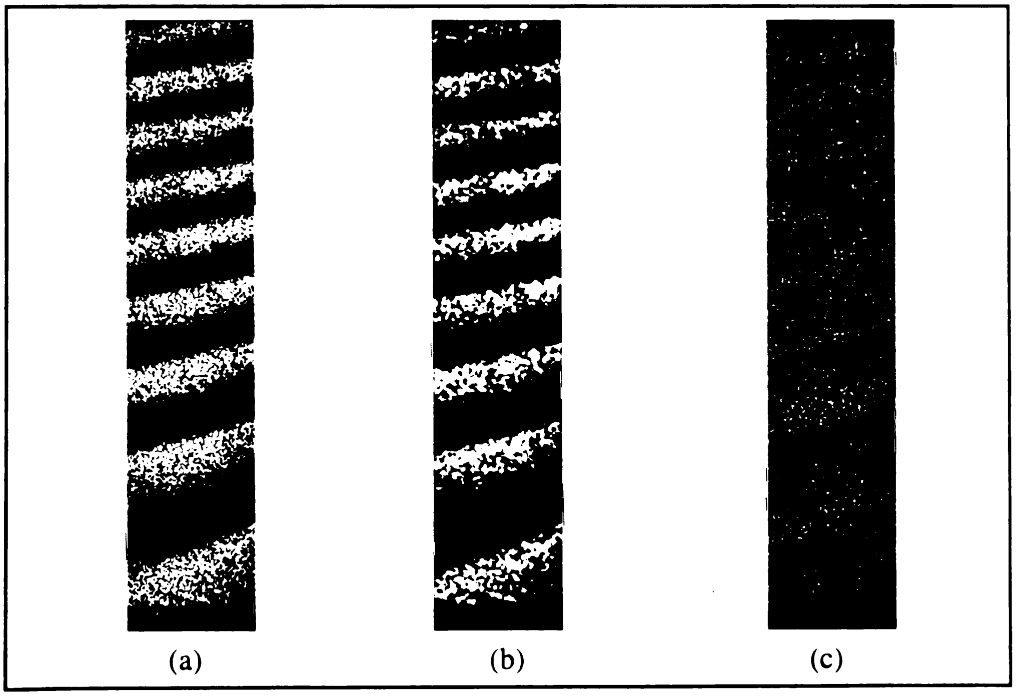

Fig. 2.27 Example of digital image filtering, (a) the original fringe pattern, (b) the lowpass filtered fringe pattern, and (c) the highpass filtered fringe pattern.

(3) Edge detection: An edge in an image is a boundary or contour at which a significant change occurs in some physical aspect of an image. The objective of an edge detection algorithm is to locate the regions where the intensity is changing rapidly. Noise reduction prior to edge detection is very desirable in processing images with background noise. An example of the impulse response of a Laplacian-based filter is shown in Figure 2.28.

1	1	1
1	-8	1
1	1	1

Fig. 2.28 The impulse response of a Laplacian edge detection filter.

(4) Median Filtering: Median filtering is a nonlinear process useful in reducing impulsive, or salt-and-pepper noise. Figure 2.29 shows the removal of the "salt-and-pepper" noise by a 3 by 3 median filter. It is also useful in preserving edges in an image while reducing random noise. In a median filter, a window slides along the image, and the median intensity value of the pixels within the window becomes the output intensity of the pixel (normally the center pixel) being processed.

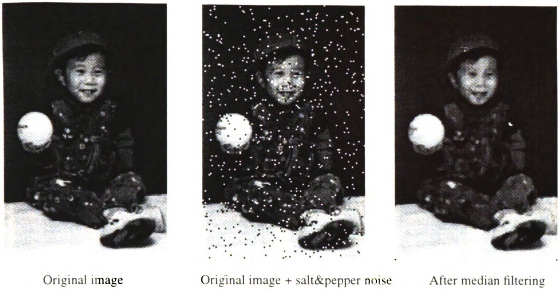

Fig. 2.29: The remove of salt-and-pepper noise by a 3 by 3 median filter.

Like lowpass filtering, median filtering smooths the image and is thus useful in reducing noise. Unlike lowpass filtering, median filtering can preserve discontinuities in a step function and can smooth a few pixels whose values differ significantly from their surroundings without affecting the other pixels.

The choice of the size of the median window depends on the context. Because it is difficult to choose the optimum window size in advance, it may be useful to try several median filters of different window sizes (in pixels) and choose the best of the resulting images, or the image may be filtered more than one time using the same window size. One method that tends to preserve 2-D step discontinuities well is to filter a 2-D signal along the horizontal direction with a 1-D median filter and then filter the result along the vertical direction with another 1-D filter. This method is called separable median filtering, and is often used in 2-D median filtering applications [Lim 1990].

Figu

is show

beam

filters

(5) Tem

its poten

temporal

image fra

Figure 5.30 is a demonstration of applying median filters. The original fringe pattern is shown in Figure 5.27(a). This fringe pattern was produced by ESPI from a cantilever beam fixed at the bottom and point loaded at the top end. Three different sizes of median filters were implemented on the original fringe pattern.

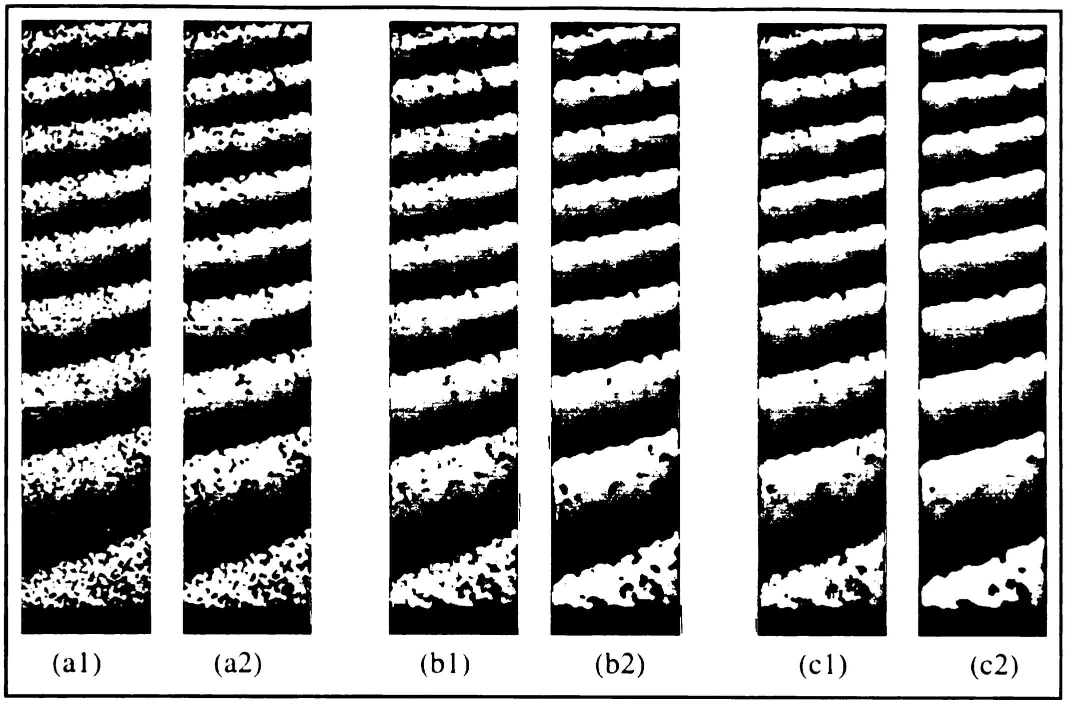

Fig. 2.30: Fringe processing by median filtering, (a1) and (a2) are the results from single 3 by 3 and double 3 by 3 median filtering respectively, (b1) and (b2) are the results from single 5 by 5 and double 5 by 5 median filtering respectively, and (c1) and (c2) are the results from single 7 by 7 and double 7 by 7 median filtering respectively.

(5) Temporal filtering: One major advantage of temporal filtering over spatial filtering is its potential of reducing degradation without signal distortion. The simplest method of temporal filtering is frame averaging, which is very effective in processing a sequence of image frames in which the image does not change from frame to frame but the degradation

does.

In dig

median fi

poorly m

stage to r

2.9.6 A

A pr

ESPI sy

(a) Obt

speckle

does.

In digital ESPI and ES systems, among the above described filtering operations, median-filtering seems best suited for the reduction of "salt and pepper" type of noise and poorly modulated pixels. Temporal filtering process may be used at the image acquisition stage to reduce image degradation.

2.9.6 An example of ESPI information processing flow

A pictorial illustration of phase information processing typically implemented in an ESPI system is shown here.

(a) Obtaining fringes -- Figure 2.31 shows the raw fringes from the subtraction of two speckle patterns corresponding to two states of the test object.

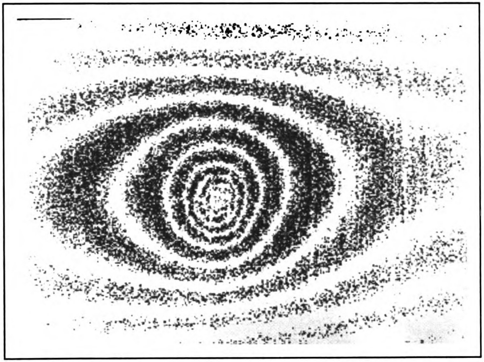

Fig. 2.31 Fringe pattern from subtraction of two speckle patterns.

(b) Modulo 2π phase calculation -- Figure 2.32 is a picture of the calculated modulo 2π phase map of the fringe pattern from Figure 2.31.

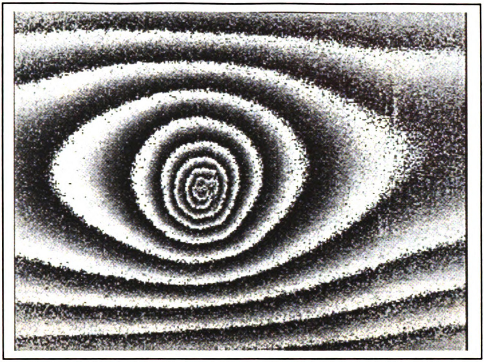

Fig. 2.32 Modulo 2π phase map of the fringe pattern from Figure 2.31.

(c) Data conditioning -- After applying median filtering on the phase map shown in Figure 2.32, some noise is removed and the result is shown in Figure 2.33.

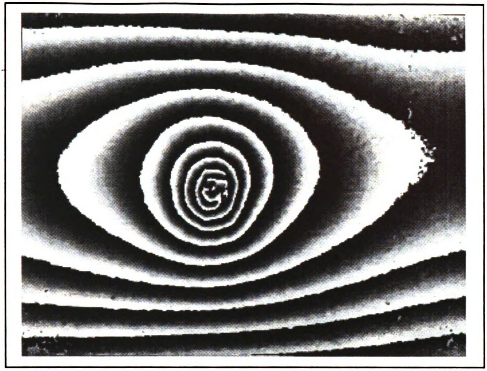

Fig. 2.33 Median filter filtered modulo 2π phase map.

(d) Fringe unwrapping (fringe counting) -- Figure 2.34 shows the unwrapped phase map from Figure 2.33.

th

Ny

pe

dec

rea

four

may

about

CCD

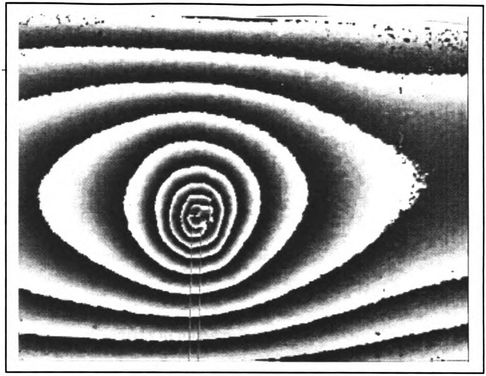

Fig. 2.34 The phase map after phase unwrapping (fringe counting).

Note that there are two vertical lines in this picture, which indicate error flags during the phase unwrapping process.

In acquiring interferograms using CCD arrays, to avoid loss of information, the Nyquist sampling theory frequency must be satisfied. This means that at least two pixels per fringe are required. Jones & Wykes [1989] pointed out that, owing to the speckle decorrelation, the number of speckles per fringe should be greater than five to give reasonable clear fringes in ESPI. Their analysis is close to the practical cases where we found that, for a CCD having 512 x 512 pixels, the maximum number of clear fringes that may be obtained from a good specimen (flat rough surface) is around 60, which means about 10 pixels per fringe. The average speckle size is assumed to be equal to the size of a CCD pixel.

m

acc

Fas

high

are

calc

2.9.7

- In

  th

  th

- Fr

  sli

- Re

  and

  eli

- De

  con

- Env

  acou

  distu

Phase measuring interferometry can measure a wave front with a repeatability of $\frac{\lambda}{500}$ rms [Lai and Yatagai, 1991] and an accuracy of $\pm 1''$ [Chang et al, 1985]. The speed and accuracy of the phase measurement technique will be further improved in the future. Faster CCD cameras with higher spatial resolution, higher sensitivity, lower noise, and higher dynamic range are under continuous development. CCDs with 2048 x 2048 pixels are available now. Phase shifting devices are becoming better. Algorithms for phase calculation and phase unwrapping will also be improved.

2.9.7 Possible error sources in phase measurement

- Intensity instability of the light source: The light source intensity during recording of the frames may vary from one frame to another. When the laser is already warmed up this error should be negligible.
- Frequency instability of the light source: This instability may cause λ to change slightly, but this effect is usually very small and negligible.
- Reference phase error: This is the deviation for the *i*th shift or step between the actual and desired values of α_i. By carefully calibrating the PZT used, this error can be eliminated.
- Detector nonlinearity: For CCD detectors the nonlinearity is negligible, but it can be considerable for vidicon tubes.
- Environment disturbances: These include air turbulence, floor vibration, and acoustically induced oscillation. By looking at live correlation fringes, we can see the disturbances; if they do not affect the fringe pattern, then they do not matter.

- Electronic and quantization errors: For a CCD camera this is very small and negligible.

2.10 Measurement of dynamic events

Measurement of dynamic movements, harmonic, nonharmonic, and transient, have been a popular area of study by using holographic interferometry [Vest 1979]. The most popular application is vibration mode shape measurement and analysis. Generally, the same studies can be made using ESPI in a much more convenient way.

A paramount reason for using optical methods is that they are noncontacting, therefore, the true characteristics of the object under study will not be altered by the measuring devices. Many structures are not tolerant of mass loading by transducers, which modify their modal response resonant frequencies and corresponding modes of vibration. Moreover, conventional approaches identify resonant frequencies, damping, mode shape, phase, and amplitude by discrete structural response measurements that approximate the continuous dynamic characteristics of the structure.

With ESPI, vibration mode shapes can be observed instantly as the frequency varies. The amplitude and phase may also be determined automatically. There are three basic methods to be used to extract the information of dynamic events. They are: (1) time-average, (2) stroboscopic, and (3) pulsed laser. These techniques are discussed below.

2.10.1 The time-average method

For vibration study, the simplest and most common method uses a continuous wave (cw) laser, so that the interferometer produces a time-averaged image of the illuminated target for each video frame. For a sinusoidally vibrating object, the time-average yields a fringe pattern having a Bessel function intensity profile in which the brightest (zero order) fringe corresponds to stationary regions. Figures 2.35 and 2.36 are vibration mode samples of two composite laminate plates made of carbon fiber and epoxy vibrating at 2057 Hz. The two plates are the same except that the one in Figure 2.36 has a cut. We can see that there are some differences in the vibration mode shape due to that cut.

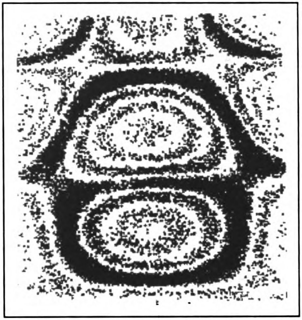

Fig. 2.35 A composite plate vibrating at 2057Hz.

vi

int

Be

obs

pha

sec

illus

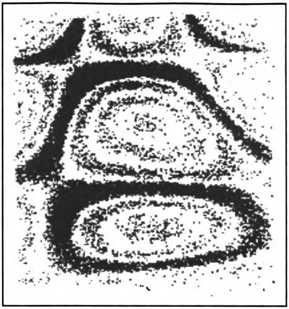

Fig. 2.36 A composite plate with a cut vibrating at 2057Hz.

The benefits of the time-average method are that it gives a good visualization of the vibrating mode shape with easily identified nodes and antinodes. Limitations are that the information containing the phase of vibration is lost in the time-averaging process, and the Bessel function modulation means that only a very limited number of fringes can be observed, especially for large amplitude vibration. The first problem can be overcome by phase-modulating the reference beam to shift the position of the zero order fringes. The second problem is inherent with the time-average process. Figure 2.37 shows an illustration of the time-average operation.

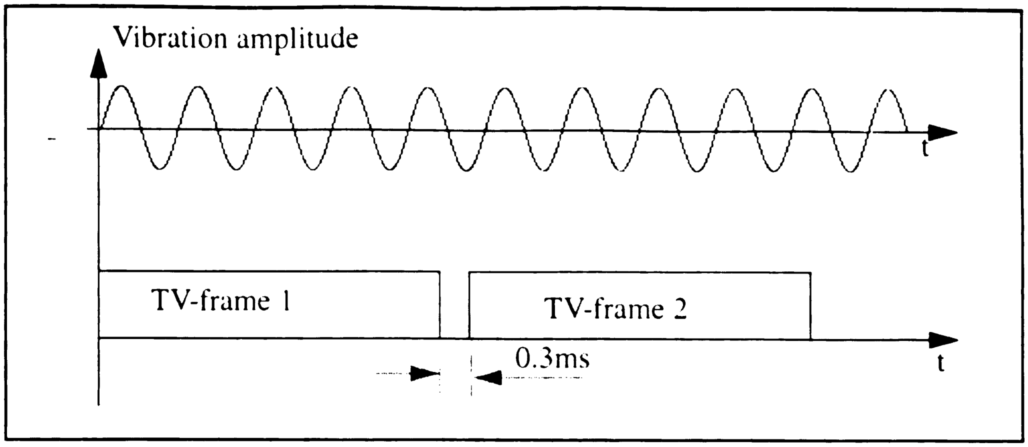

Fig. 2.37 Schematic of the time-average ESPI operation.

In the time-average operation, the instantaneous light intensity on the image plane (CCD target) can be written as

$$I(x, y, t) = I_o + I_r + 2\sqrt{I_o I_r}\cos(\vec{K} \bullet \vec{L} + \phi_0) \tag{2.37}$$

where $\vec{K}$ is the sensitivity vector of the optical layout of the measurement, $\vec{L}$ is the displacement vector, and ϕ_0 is the initial phase difference between the object beam and reference beam or between two object beams as for in-plane measurement.

For vibration analysis with ESPI operating in its time-average mode, the intensity is averaged over the TV-frame period τ. Equation 2.36 becomes

$$I(x, y) = I_o + I_r + \frac{2}{\tau}\sqrt{I_o I_r}\int_0^{\tau}\cos(\vec{K} \bullet \vec{L} + \phi_0)dt\,. \tag{2.38}$$

For a harmonically vibrating object with circular frequency ω, the displacement is given by

$$\vec{L} = \vec{a}_o(x, y)\sin(\omega t) \ . \qquad (2.39)$$

When the vibration period is much less than the frame exposure time (1/30 sec), or when the exposure is equal to the vibration period or a multiple of it [Løkberg 1979], the time-average intensity is then obtained by integrating equation 2.37, which results in

$$I(x, y) = I_o + I_r + 2\sqrt{I_o I_r} J_0[\vec{K} \bullet \vec{a}_o(x, y)]\cos\phi_0 \ , \qquad (2.40)$$

where J_0 is the Bessel function of first kind and order zero, and the term $\cos\phi_0$ represents the high frequency speckle noise. If the vibration period condition is not satisfied, there will be some deviation from the J_0 function. After DC filtering and full-wave rectification, the video signal which will be displayed on the monitor is proportional to:

$$I(x, y) = 2\sqrt{I_o I_r}\left|J_0[\vec{K} \bullet \vec{a}_o(x, y)]\cos\phi_0\right| \ . \qquad (2.41)$$

for normal illumination and observation, and for out-of-plane vibration, equation 3.40 becomes

$$I(x, y) = 2\sqrt{I_o I_r}\left|J_0\left[\frac{4\pi}{\lambda}a_o(x, y)\right]\cos\phi_0\right| \qquad (2.42)$$

A typical example of a time-average ESPI image is shown in Figure 2.23. The brightest fringes represent zero order fringes, $J_0(0)$, and their centers correspond to the nodal lines where the vibrational amplitude is zero. The other fringes are called antinode fringes, and they depict the isoamplitude contours. The amplitude at those fringes may be found by inverting the Bessel function. For example, when a He-Ne laser is used ($\lambda = 0.6328$), the first order dark fringes correspond to $a = 0.12$ μm, the first bright fringes correspond to $a = 0.19$ μm and so on.

Note that the fringes are modulated by a $|J_0|$ function in digital ESPI instead of a J_0^2 function as in the early generation of ESPI based on analog signal processing and in time-average HI [Vikhagen 1989; Lu et al., 1989]. Because the envelope of $|J_0|$ falls much slower than that of the J_0^2, more fringes may be seen in digital ESPI than in HI or analog ESPI.

In many cases, the spatial frequency of $|J_0|$ is also rather low, therefore, a practical DC filter that will remove the DC component is difficult to design. To reveal vibration mode shapes, the better way is to use the subtraction technique.

There has been a flurry of work to enhance the fringe visibility by various techniques including: (1) time-average subtraction techniques [Lu et al., 1989], (2) phase stepping and digital image processing by max-min fringe scanning and a normalized max-min scanning technique to reduce speckle noise [Vikhagen 1989], (3) four phase steps with each step $\frac{\pi}{2}$ to reduce speckle noise [Bushman 1989], (4) introducing additional phase steps of 0, $\frac{\pi}{6}$, and $\frac{\pi}{3}$ to the $\frac{\pi}{2}$ phase step time-average subtraction method in order to eliminate speckle noise and enhance fringe visibility [Lu et al., 1990], and (5) by sequential averaging of a large number of decorrelated speckle patterns [Slettemoen 1980; Montgomery and Berquist 1985]. A quantitative analysis has been carried out to evaluate the improvement in the contrast of the fringes obtained from various techniques by Joenathan and Khorana [1992c] and Joenathan [1991c]. A number of vibration observation techniques using ESPI were also discussed and compared by Creath and Slettemoen [1985]. The major purpose of these techniques is to improve the fringe quality.

Compared with the ESPI real-time subtraction mode as used in the static cases, the time-average mode of ESPI is more tolerant of object instability and environmental disturbances. Measurements with both the object and ESPI on the ground without a vibration isolation table can be achieved [Malmo and Vikhagen 1988a; Løkberg and Malmo 1988]. Time-average ESPI is characterized by good environmental noise protection, and real-time subtraction is characterized by good fringe quality.

To reduce the speckle noise and improve fringe quality, the time-average subtraction method was developed [Lu et al., 1989, 1990]. In this approach, a time-average image is stored, then another time-average image with a phase shift in the reference beam or object beam is recorded and subtracted from the first image. Time-invariant noises will be removed by the subtraction process.

Assume that the phase of the reference beam is shifted between frames by $\Delta\phi_r$, we have from equation 2.39,

$$I_2(x, y) = I_o + I_r + 2\sqrt{I_o I_r} J_0[\vec{K} \bullet \vec{a}_o(x, y)] \cos(\phi_0 + \Delta\phi_r) \quad . \tag{2.43}$$

where I_2 is the intensity with the phase shift $\Delta\phi_r$. Rewrite equation 2.39 as

$$I_1(x, y) = I_o + I_r + 2\sqrt{I_o I_r} J_0[\vec{K} \bullet \vec{a}_o(x, y)] \cos\phi_0 \tag{2.44}$$

Subtract equation 2.42 from equation 2.43; the result is

$$\begin{aligned} I(x, y) &= I_1(x, y) - I_2(x, y) \\ &= 4\sqrt{I_o I_r} J_0[\vec{K} \bullet \vec{a}_o(x, y)] \sin\left(\phi_0 - \frac{\Delta\phi_r}{2}\right) \sin\left(\frac{\Delta\phi_r}{2}\right) \quad . \end{aligned} \tag{2.45}$$

When the phase shift $\Delta\phi_r$ is π, $\sin\left(\frac{\Delta\phi_r}{2}\right)$ takes its maximum value of 1, which results in maximum signal value. This result is in agreement with the fringe contrast analysis by

Joenathan [Joenathan 1991c]. A wrong result of $\frac{\pi}{2}$ was obtained by Lu et al for the highest visibility [Lu et al., 1989].

Based on their time-average subtraction method, Lu et al. proposed another technique which introduces additional phase shifts to several time-average images in order to remove the speckle noise [Lu et al., 1990a]. In their theoretical analysis a rather poor approximation $|\cos x| \approx (\cos x)^2$ was used, and this resulted in a 'complete removal' of the high frequency speckle noise. Nevertheless, according to their experiment results, the fringe smoothness was obviously improved. The time-average subtraction method along with the speckle averaging technique can produce good visibility fringes even in a non-vibration-isolation condition [Montgomery and Bergquist, 1985]. Good results are shown in the paper by Lu et al. [1990].

In order to extend the measurement range of vibration amplitude and to extract the phase information. Phase modulation techniques may be used. Phase modulation can be achieved through amplitude modulation and frequency modulation. The following is a description of the two methods.

(a) Amplitude modulation by reference beam

Reference wave modulation is a well known technique from holography [Aleksoff 1974]. This theory can be applied directly to ESPI. The amplitude range for vibration measurement by time-average recording of ESPI can be extended by sinusoidal phase modulation of the reference wave, and the amplitude and phase of the vibration may be determined from this technique [Løkberg and Høgmoen, 1976]. With reference wave modulation equation 2.40 becomes

$$I(x,y) = 2\sqrt{I_o I_r}\left|J_0\left\{\frac{4\pi}{\lambda}[a_o(x,y)^2 + a_r^2 - 2a_o(x,y)a_r\cos(\phi_o(x,y) - \phi_r)]^{\frac{1}{2}}\right\}\cos(\phi_0)\right|, \qquad (2.46)$$

where $\bar{a}_o(x,y)^2$ is the amplitude and $\phi_o(x,y)$ is the phase of the vibrating object, and a_r and ϕ_r are the amplitude and phase of the vibrating mirror used to modulate the reference beam respectively. Equation 2.46 shows that the argument of the function which originally contained only the object amplitude has been replaced by the vectorial difference between the object and reference movement vectors. The fringe pattern is determined by the amplitudes and phases of both the object and reference waves. The positions of the zero order fringes no longer represent the nodal regions of the object, but they show the regions vibrating at the same amplitude and phase as the reference mirror. This technique has been automated to obtain the amplitude and phase of vibrating object, where the amplitude or phase was scanned to yield a phase map [HØgmoen and LØkberg 1976; Stetson and Brohinsky 1988; Vollesen 1990]. Phase modulation was also used to detect very small vibration [HØgmoen and LØkberg, 1977; Ellingsrud and Rosvold 1992]. Moreover, a phase modulation technique has been extended to combine ESPI with laser velocimetry (LV) for compensation of random out-of-plane motion and extending the vibration measurement range [Valera, Harvey, and Jones 1992]. In this technique, automatic heterodyning of the ESPI was obtained. The zeroth order Bessel fringe in time average ESPI overlapped the point probed by the LV [Vlera, Doval, and Jones 1993].

(b) Frequency modulation in reference beam

The Bessel function has a useful property which can be taken advantage of. This property is that the primary maximum of the Nth-order Bessel function (corresponding to the brightest area in the fringe pattern) occurs for larger and larger values of the argument as the order of the Bessel function increases. Thus any number of fringes corresponding to the smaller amplitudes can be eliminated by using the proper higher-order Bessel function [Aleksoff 1974]. This property can be realized by frequency translation techniques using, for example, traveling wave ultrasonic modulators. The output signal from a traveling wave ultrasonic modulator is translated either up or down in frequency by an amount equal to the ultrasonic frequency. Frequency translation in the range of 1MHz to 100 MHz is obtainable. When there is no modulation in the reference beam, the intensity of the fringe pattern is modulated by the zero order Bessel function. Nodal location in the vibration mode shape can easily be identified, which provides useful information for some practical applications. If the frequency translation is $N \cdot \nu$ where N is a integer and ν is the vibration frequency of the test object, then the Nth-order Bessel function will be the intensity modulation function of the fringe pattern.

2.10.2 The stroboscopic method

If the illumination is changed so that the target is viewed at one or two discrete time points on its vibration cycle (equivalent to a static displacement case), then the fringe pattern has a cosinusoidal intensity profile instead of J_0 profile, and it also retains the vibration phase information [Pedersen, LØkberg, and FØrre 1974]. Stroboscopic illumination can be achieved by using a device such as a mechanical chopper or an acousto-optic modulator, provided that the duration of each illumination period is very small compared to the period of vibration. This method gives poor laser power efficiency, because most of the energy is wasted. It is difficult to study an object having large size

without access to high power lasers. Pulsed lasers may be used to advantage for this problem. Q-switching can produce pulses of very short duration which yield true cosinusoidal fringe patterns even for very high frequency vibrations, and the firing of the laser pulses can be accurately synchronized to the object vibrations. Consecutive laser pulses can also be shifted to enable phase stepping analysis for automatic phase determination. Because the pulse timing and separation can be varied, Q-switching also enables non-steady-state vibrations to be sampled and analyzed. Figure 2.38 illustrates the stroboscopic process.

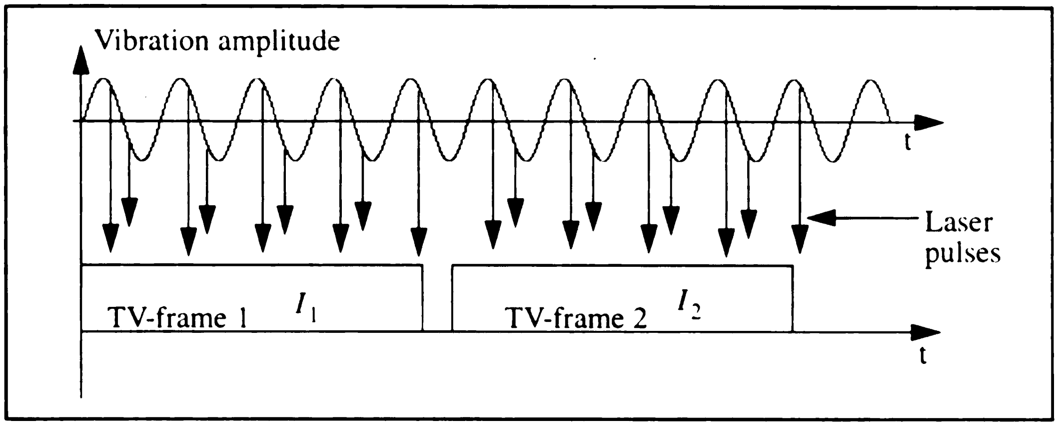

Fig. 2.38 Schematic of stroboscopic ESPI operation.

Uniform fringe contrast is an advantage of the stroboscopic technique. In order for this technique to work, the path-length difference between the object and reference beams should be small enough to avoid any significant time delays between the two beams.

The most common type of strobing is a series of rectangular pulses with a strobe frequency at some multiple of the object vibration frequency. Typically a strobing frequency of twice the vibration frequency is used, and the strobing coincides with the two turning points of the vibration cycle. The pulse width τ controls the fringe contrast ir

ta

[F

be

int

im

Kr

ph

norr

uniformity via the $sinc(\tau\nu)$ weighting function, where ν is the vibration frequency. For short pulses the weighting approaches uniformity.

With the advancing technologies of diode lasers and fiber optics, the stroboscopic technique can be implemented more easily and economically; and the systems can be made more compact [Anderson, Valera, and Jones 1993; Preater and Swain, 1990]. The diode laser has many advantages as an optical source for ESPI; they are compact, rugged and inexpensive, and compatible with single-mode optical fibers. Diode lasers offer the advantage of easy modulation via control of their injection current.

We now discuss two important variations of the technique.

(1) Two strobes per vibration cycle method

Like the continuous wave (cw) time-average method, the subtraction operation can be used to reduce noise in the fringe pattern for strobing techniques. Recently, two techniques were proposed for reducing environmental disturbances in the fringe pattern [Pouet and Krishnaswanmy 1993]. These methods used a ground glass in the reference beam for decorrelating the two frames to be subtracted. If a PZT mirror is used to introduce a known phase shift in the uniform reference beam, the fringe quality should be improved. The following treatment of this method is similar to that of Pouet and Krishnaswanmy, but it is easier to understand and it develops mathematically the best phase shifting value required in the subtraction operation. In this method, strobing normally occurs at the two extrema of each vibration cycle as illustrated in Figure 2.39.

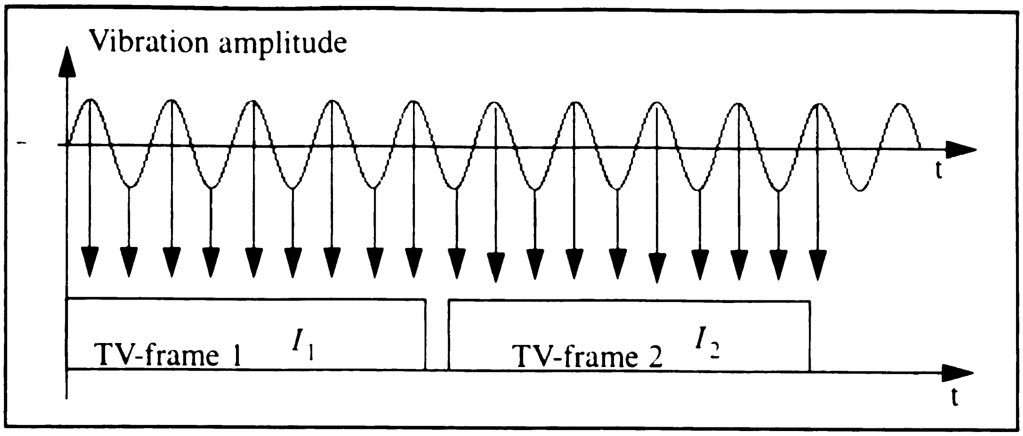

Fig. 2.39 Schematic of two strobes per vibration cycle method.

In order to remove noise and at the same time retain the useful fringes, a phase shift $\Delta\alpha$ needs to be introduced between two consecutive frames (speckle patterns). The light intensities of the two speckle patterns can be expressed as

$$I_1 = N\{2(I_r + I_o) + 2\sqrt{I_r I_o}[\cos(\phi_o) + \cos(\phi_o + \Delta\phi)]\} \tag{2.47}$$

$$I_2 = N\{2(I_r + I_o) + 2\sqrt{I_r I_o}[\cos(\phi_o + \Delta\alpha) + \cos(\phi_o + \Delta\phi + \Delta\alpha)]\} \tag{2.48}$$

where N is the number of pulse pairs fired in each TV-frame. $\Delta\phi$ is the phase difference between the two extrema. The subtraction of I_1 and I_2 yields

$$I = I_1 - I_2 = 8N\sqrt{I_r I_o}\sin\left(\phi_o + \frac{\Delta\phi}{2} + \frac{\Delta\alpha}{2}\right)\cos\left(\frac{\Delta\phi}{2}\right)\sin\left(\frac{\Delta\alpha}{2}\right). \tag{2.49}$$

If no phase shift is introduced, $\Delta\alpha$ is zero, so the subtraction result will be zero because the two TV-frames are identical. No fringes will be seen. However, when the phase shift $\Delta\alpha$ takes a value of π, the optimum result is obtained. Equation 2.49 becomes

P

in

wh

bet

$$I = I_1 - I_2 = 8N\sqrt{I_r I_o}\cos\left(\phi_o + \frac{\Delta\phi}{2}\right)\cos\left(\frac{\Delta\phi}{2}\right) \tag{2.50}$$

(2) One strobe per vibration cycle method

In this method, the two successive TV-frames contain pulses fired at different turning points of the vibration cycle. One frame is exposed only to pulsed fired at the maximum turning point, and the other is exposed only to pulses fired at the minimum turning point. Figure 2.40 illustrates this process.

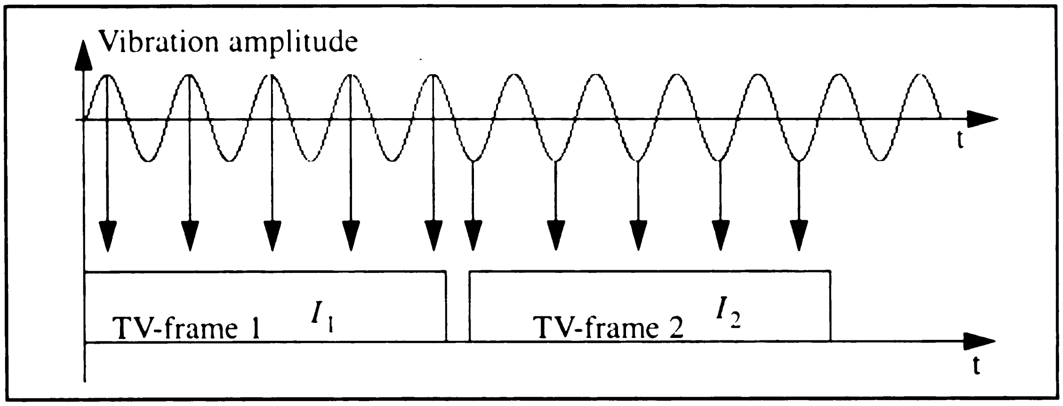

Fig. 2.40 Schematic of one strobe per vibration cycle method.

In this case, because the two frames correspond to different displacement positions; no phase shift needs to be introduced to the frames for the subtraction process. The intensities of the two speckle patterns are given by

$$I_1 = N[I_r + I_o + 2\sqrt{I_r I_o}\cos(\phi_o)] \tag{2.51}$$

$$I_2 = N[I_r + I_o + 2\sqrt{I_r I_o}\cos(\phi_o + \Delta\phi)] \tag{2.52}$$

where N is the number of pulses fired in each frame. $\Delta\phi$ again is the phase difference between the two extrema. The subtraction of the two frames yields

$$I = I_1 - I_2 = 4N\sqrt{I_r I_o}\sin\left(\phi_o + \frac{\Delta\phi}{2}\right)\sin\left(\frac{\Delta\phi}{2}\right). \qquad (2.53)$$

which has the same form as double exposure subtraction for static measurement. Note that in both of the methods, I_1 can be taken when the object is not vibrating. In comparison with equation 2.50, the fringe intensity in this case is reduced by a factor of two and there is a $\frac{\pi}{2}$ phase difference between the fringe patterns.

2.10.3 The pulsed laser method

Pulsed lasers have been used quite often in both HI and ESPI [Parker and Jones 1988; Santoyo, Shellabear, and Tyrer 1991a; Santoyo et al. 1994; Spooren, 1992a, 1992b]. They allow for the analysis of large amplitude and nonharmonic vibrations, high-speed phenomena, and also random and transient processes. Using a pulsed laser greatly reduces instability problems. Q-switching can produce pulses of very short duration which yield true cosinusoidal fringe patterns even for vibrations of very high frequency. Consecutive laser pulses can also be shifted to enable phase stepping analysis for automatic phase determination. Because the pulse timing and separation can be varied, this method also enables non-steady state vibrations to be sampled and analyzed.

In the double exposure mode, the fringe pattern contours the change in shape between the two exposures. The two laser pulses are normally timed to occur during a single vibration cycle. Short pulses (~10ns) can freeze all but the most violent of ambient vibrations and movements. However, pulsed lasers do not always remove the need for vibration isolation. When a long time interval is required between the two exposures, it is important that the object not move between exposures, or error fringes will appear in the final fringe pattern.

A frequency-doubled diode seeded Nd:YAG laser, Q-switched to produce pulses of approximately 15 nanoseconds at a wavelength of 0.532 μm was used to study out-of-plane and in-plane vibration problems [Santoyo et al. 1991a, 1991b]. This laser was capable of operating at a repetition rate of 50 pulses/sec or 50 twin pulses/sec in a single or twin pulse mode. A double-pulsed 2 x 0.5 J ruby laser (~30 ns exposure) was used to generate better fringes in a vibration study where the fringes are cosine fringes instead of the zero-order Bessel fringes [Fällström 1991b].

Quantitative vibration mode shape can be obtained using phase shifting techniques. To present the results in a more usable form, the amplitude distribution of the vibration can be plotted in an isometric wire-mesh form after unwrapping the phase data [Shellabear et al., 1990]. The single phase step algorithm was used in this process.

In-plane vibration can also be analyzed using a pulsed laser with in-plane sensitive ESPI [Santoyo et al. 1991b]. Again, the single phase step algorithm was used to calculate the phase information. In-plane vibration measurements use two speckled beams and therefore require the use of a subtraction process. In this process, a static pattern is stored and then subtracted from the subsequent speckle patterns from the displaced object. The performance of a pulsed laser in ESPI is limited by such parameters as intensity stability, repetition rate, and spectral linewidth [Spooren 1992a].

(1) Single pulse mode

The laser is made to repetitively produce single pulses. For each laser pulse an interferogram is created on the CCD target, and it contains information on the position of the object at the moment of exposure. This is one pulse per frame (30 pulses/sec). By subtracting two successive interferograms on a pixel by pixel basis, a fringe pattern is obtained. This process is basically the same as in cw real-time subtraction ESPI. An illustration for this process is shown in Figure 2.41.

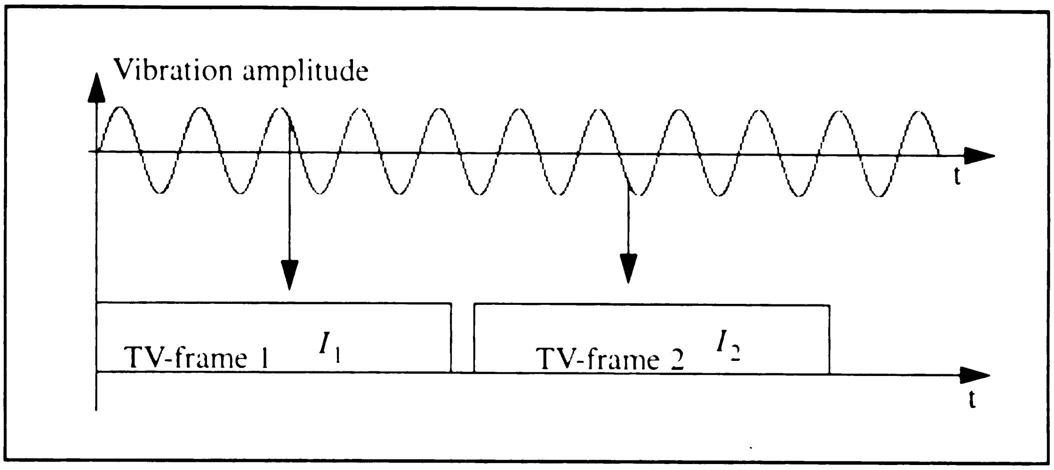

Fig. 2.41 Schematic of single pulse per frame method.

The subtraction of the two frames yields the same fringe pattern as obtained in the double exposure static method. That is

$$I = I_1 - I_2 = 4N\sqrt{I_r I_o}\sin\left(\phi_o + \frac{\Delta\phi}{2}\right)\sin\left(\frac{\Delta\phi}{2}\right). \qquad (2.54)$$

To reduce the noise, the separation between the two pulses should be made as small as possible.

(2) Double pulse addition

The double pulse addition method may be used to shorten the exposure time and, therefore, further reduce the influence of the noise [Moore, Tyrer, and Santoyo 1994]. In this case, two pulses are fired within the same frame. Figure 2.42 depicts this operation.

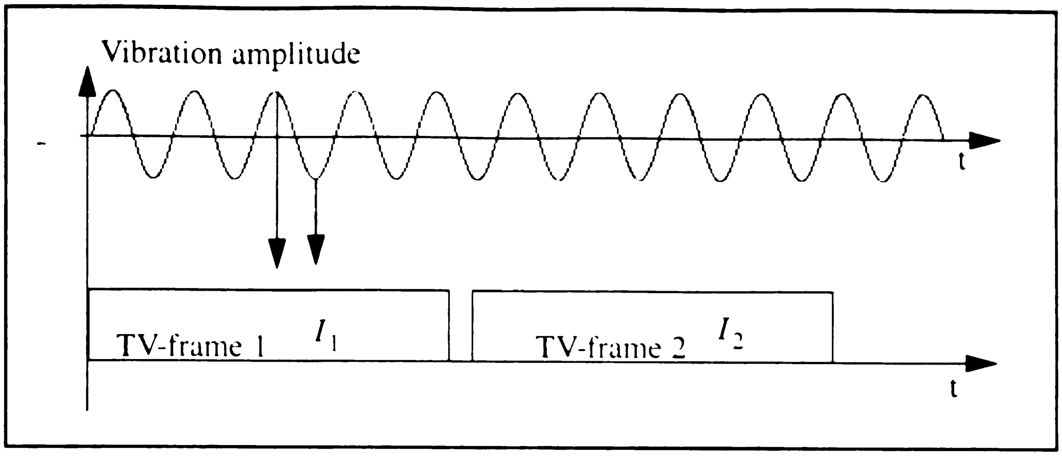

Fig. 2.42 Schematic of double pulse per TV-frame addition method.

The addition result is given by

$$I = I_1 + I_2 = 2(I_r + I_o) + 4\sqrt{I_r I_o}\cos\left(\phi_o + \frac{\Delta\phi}{2}\right)\cos\left(\frac{\Delta\phi}{2}\right). \qquad (2.55)$$

Subtraction can not be implemented in the method. In this case, the fringes are embedded in the self-interference term $2(I_r + I_o)$ along with other noise. The fringes may be revealed by digital filtering process. To remove the high frequency speckle noise, Fourier filtering has been found to be particularly effective [Kerr, Santoyo, and Tyrer 1989]. But some noise is likely to remain. The fringe visibility is, in general, not as good as that from the subtraction method.

3. Double pulse subtraction

An interline-transfer CCD has been used along with pulse-laser operating at double-pulse mode to yield subtraction fringes which have better quality than the addition fringes [Spooren 1992b]. The charge transfer takes much less time ($\sim 1\mu s$) in interline-transfer CCDs compared to frame-transfer CCDs ($\sim 300\mu s$), which makes them better suited for separation of two very close exposures to minimize environmental noise. However, there is a drawback. The spatial resolution is reduced to about half with respect to the frame-transfer CCD. A schematic is shown in Figure 2.43 to illustrate this operation. The fringe equation is the same as in the case for single pulse subtraction.

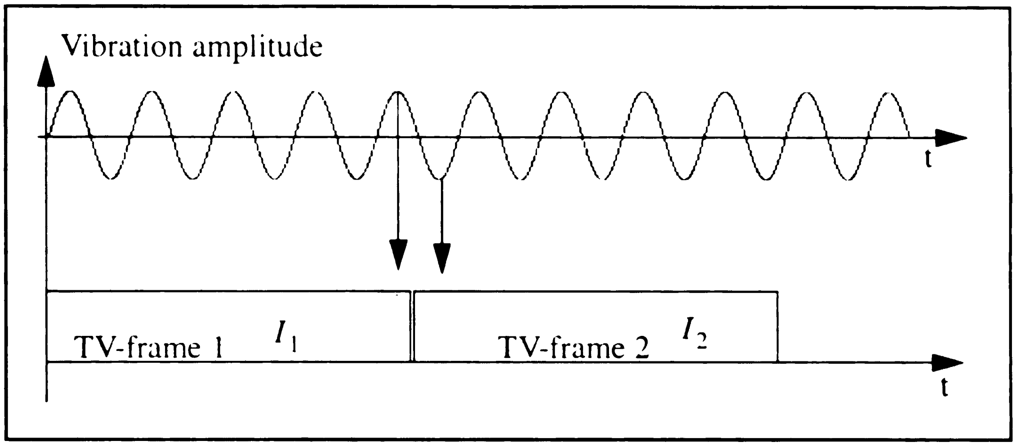

Fig. 2.43 Schematic of double pulse subtraction using interline-transfer CCD.

The choice of which method to use depends on the basis of the available laser power, the degree of noise in the environment, the desired information, and the cost. The depolarization effect is important in vibration measurement. It can result in a decrease in fringe visibility and this is especially detrimental when the time-average and pulse addition methods are used where visibility is low to begin with.

2.11 Electronic hardware and software in ESPI

Electronic hardware and software are used in an ESPI system to control the operation and process information. Related factors are discussed in the following.

2.11.1 Hardware

Electronic hardware used in an ESPI system commonly includes a computer, video input/output and imaging processing boards, a PZT controller, and a graphics display monitor. If stroboscopic techniques or pulsed lasers are used for vibration study, additional electronics are required to synchronize the desired operations.

(1) Video Input

Image acquisition is performed by devices called frame grabbers, which can also store and display the images. Image acquisition converts an image into an array of data points, which can be stored digitally, processed and enhanced, and subsequently displayed on a video monitor. Because the frame grabbers used for ESPI acquire images in real time (30 frames a second), special video-speed A/D converters must be used. The RS-170 (IEEE) standard allows $52.59\mu s$ for each line in a 512 x 480 image to be sampled. In this time, a 512 by 480 frame grabber, for example, must convert 512 pixels, or perform 512 A/D conversions. This requires an A/D converter with a throughput of almost 10 MHz. The system used in the experimental studies employed an 8-bit A/D converter.

The number of picture elements or pixels which make up a digitized frame determines the spatial resolution of the signal - the amount of detail with which shapes in the image are represented. Spatial resolution is analogous to the number of scan lines displayed in a television picture. Spatial resolution of digitized frames is expressed as a matrix: the number of pixels (columns) per line by the number of lines (rows) into which the image is divided. Typically spatial resolutions are 512 pixels by 480 lines, or 640 pixels by 480 lines for 60Hz standard. For 50Hz standard 512 x 512 and 768 x 512 are normally used.

Brightness resolution has to do with how accurately a digital pixel value is represented. Only a monochrome signal is used in ESPI. Brightness resolution is determined by the resolution of the A/D converter that performs the image acquisition. An 8-bit A/D converter is said to have an 8-bit gray scale, and it divides the total signal voltage range, or the intensity spectrum from total black to total white, into 256 shades of gray.

(2) Image Processing

Digital image processing can be implemented either in software or at higher speed using dedicated processing hardware. Software implementations require the use of the computer system in which the image acquisition hardware is installed. In this process, the host computer takes pixel values from the frame memory, performs operations on them, and returns them to the frame memory. Each pixel must travel over the system bus twice, thus tieing up the bus for extended periods of time. Hardware implementation involves specialized image processing hardware, which is either on the same board as the image acquisition hardware, or which connects to the acquisition hardware using separate, dedicated data lines. Image processing hardware varies greatly in sophistication, from simple look-up tables to general-purpose floating-point processors. Depending on the type of processing hardware used, all or most of the pixel processing can be performed without using the host CPU. The simplest processing element is the input look-up table (LUT). Input LUTs are utilized on many frame grabbers. The input LUT maps any data value to any other value in real time, and can be used for thresholding, addition, subtraction, multiplication, division by a constant, and inverse video. Each input LUT uses the digital data value of the pixel as an input or index into the table. Each index value has a corresponding output value. The input-output mappings are determined at the time the LUT is defined. Providing a connection between the output of the frame grabber's frame-store memory and the input LUT adds considerable flexibility. Image data can be passed repeatedly through different look-up tables to accomplish multi-step image processing. LUTs have been used in ESPI [Ganesan, Kothiyal, and Sirohi 1989].

Furthermore, a frame processor with built-in ALU (arithmetic logic unit) permits multi-frame operations to be supported in real time. The frame processor is not general-purpose. It is dedicated to performing specific image processing operations such as frame addition, subtraction, frame averaging, histograms, and convolutions, and can frequently perform them more quickly than less optimized general purpose processors. Some frame grabbers combine a frame grabber and a frame processor on a single board.

(3) Image Display

Most frame grabbers also contain circuity which converts the digital pixel data back into a corresponding compatible signal for display. This lets one view the stored or processed image to check processing or acquisition on a separate analog RGB monitor or on the system monitor.

2.11.2 Software

Menu driven software is normally used to control the information flow of an ESPI system. Major functions should include image acquisition, image processing, control of phase shifting/stepping, calculation of phase/displacement information, display of results in graphical form, and save/retrieve of the measurement results. Additional functions may be needed in the measurement of dynamic events (including vibration).

2.12 Applications

The basic function of an ESPI system is to measure small displacements. Applications using ESPI have been carried out in many areas including industry, science, and medical technology. Figure 2.44 shows a general setup for ESPI applications.

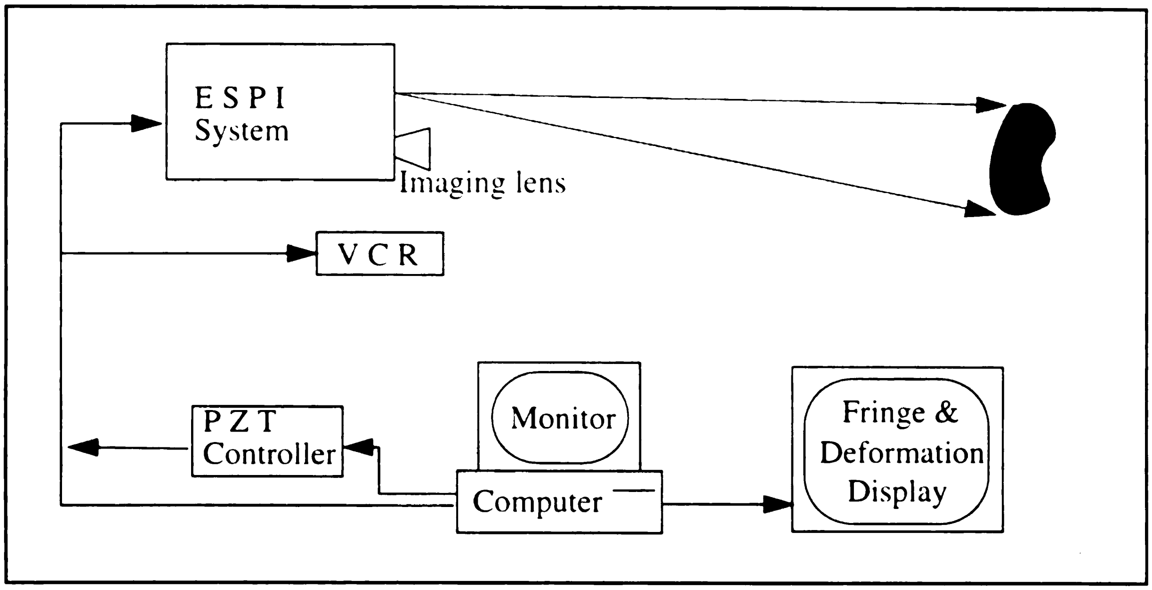

Fig. 2.44 A general setup for ESPI applications.

2.12.1 Industrial applications

ESPI represents a powerful tool for NDE applications, vibration study, materials characterization, experimental mechanics, and validation of numerical methods. The opportunity and challenge in industry is, aside from system development, to integrate CAE (computer aided engineering) methods with experimental methods to optimize structural performance in the design, manufacturing and service stages. For example, the input from the experimental results can make finite element analysis more realistic. In one application, finite element method (FEM) was used along with the experimentally determined boundary conditions to provide information on optimal location of critical components for minimal stressing and maximum fatigue life [Brown 1993]. ESPI can be used as an integral part of an iterative process to place sensors (for pressures, temperatures, flows, and vibrations) on engines as they are developed and to retrofit sensors on established engines [Brown et al. 1993].

ESPI has been used to detect unbonded areas of adhesive joints [Holownia 1988; Cloud et al. 1993], to study vibration in the automotive industry [Buckberry and Davies 1990], to measure the local mass transfer coefficient [Saluja, Button, and Dobbins 1988], to investigate the natural convection phenomena from a horizontal heated tube [He 1991], and for flow research [Bryanston-Cross and Towers 1992].

Several specific application areas are described in the following section.

(1) Nondestructive evaluation/testing

Nondestructive testing is the detection of flaws and damage in materials or structures by procedures which do not require destruction or significant alteration of the component under test. Usually the objective of the detection is to determine the location and the size of the flaws and damage. These defects may be cracks, voids, debondings, inhomogeneous material properties, residual stresses, imperfect fits, delaminations, fiber breakage, matrix cracking and so on. The flaws and damage are normally shown in the fringe pattern as fringe anomalies such as "bull-eye", "butterfly", fringe discontinuites, abrupt fringe curvature changes, or sudden fringe density changes. The loading techniques should be designed so that flaws and damage can be revealed as distinctly as possible, and the ideal loading may be the one which simulates the actual working condition of the component. Automatic pattern recognition methods combined with a knowledge based approach can be used for the detection and classification of anomalous fringe patterns [Osten. Jüptner. and Mieth 1993]. This is helpful for an unskilled operator.

There are a number of other NDE techniques that are used in industries and maintenance services [BØving 1989]. However. ESPI possesses many unique capabilities such as allowing real-time measurement. being non-invasive. and offering direct connection to computers.

The interferometric fringes formed are a measure of the amount of surface deformation between two different states of the object under test. The comparison may be between two deformed (stressed) states or between a deformed state and an undeformed (unstressed) state. The method of stressing the object is critical. because the sensitivity of different types of flaws to different loading (stressing) methods is different. The reaction to stressing is a function of physical and material properties with respect to the loading method. Normally. the fringes (deformation contours) on the test object are continuous and smooth. But in the regions of flaws or damage, the response of the surface to the stress is often different, and the flaws manifest as a irregular changes in the fringe pattern. The flaws and damage which affect the structure the most may be detected by employing the loading type which simulates the working condition of the product.

While the changes between frames are permissible and give the real time dynamic display, the rate of change during a single frame period has to be controlled to keep movements to a magnitude small by comparison with the speckle size, so as to avoid blurring out the pattern. Phase-gradients may be calculated to make the defect more distinct in some cases [Vikhagen 1990; Vikhagen and LØkberg 1990].

(2) Materials characterization and mechanics

Young's modulus can be determined from FEM by using an iterative approach with the results from ESPI (both dynamic mode and static mode) and LDV (laser Dopler velocimetry) [Brown and Pryputniewicz 1993]. Methods which use the mode shapes and frequencies measured by ESPI and the mode shapes calculated by FEM to nondestructively determine the material properties (Young's modulus and Poisson's ratio) of anisotropic materials have been demonstrated [Fällström 1991b; Fällström and Jonsson 1991; Fällström and Molin 1987]. ESPI has been used to measure the thermal expansion of a piston by Ratnam et al. [1992]. ESPI was used to monitor strains and crack-propagation paths of rocks in fracture mechanics [Maji and Wang 1992]. Phase transitions in materials may be studied using ESPI [Malmo and Vikhagen 1990]. ESPI was used to study the behaviors of materials at very high temperatures (near 3000 °C). Surface changes due to oxidation or phase transitions may be studied. Crack growth at high temperature also can be studied. Some measures have been taken in dealing with hot objects [Malmo, Løkberg, and Slettemoen 1988]. A 2.5 nm-linewith interference filter was inserted in the imaging path to suppress the background radiation. Further suppression of the background radiation can be achieved by inserting neutral density and infrared filters. A mechanical chopper or an acousto-optic modulator synchronized to the TV-framing rate can be used to shorten the exposure time of the CCD camera and, therefore, to reduce the effect of air turbulence and freeze the microstructure change. An argon laser may be used with detectors which have a relatively low response in the near infrared part of the spectrum.

In-plane sensitive ESPI has been used for analyzing thermal strain on ceramic and composite materials [Höfling et al. 1991]. Because of the anisotropy of fiber-reinforced composites, a change of temperature ΔT will not only cause a uniform expansion or shrinkage but will also result in distortions. The coefficients of thermal expansion and the creep due to the internal stress caused by the mismatch of thermal expansion coefficients can be studied. In-plane sensitive ESPI was used for fracture mechanics testing [Maji, Wang, and Lovato 1991]. In-plane ESPI equipped with a pulsed laser was used to measure the in-plane strain on high speed rotating components [Preater and Swain 1993].

(3) Vibration analysis

Vibration analysis is a popular application area of optical methods including holographic interferometry and ESPI. Applications in vibration analysis previously studied using HI can, in general, be investigated with much ease by ESPI. Like HI, ESPI has been used for modal analysis of musical instruments [Rossing and Hampton 1990]. Some applications using ESPI in the field of vibration analysis have been reported [e.g. LØkberg, HØgmoen, and Holje 1979; Ek and Jansson 1986; Tyrer 1988; Pechersky and Bergen, 1990; LØkberg et al., 1991]. However, much work is needed to widen the applications and convince industrial people that they can benefit from the technique.

(4) Integration with numerical models

ESPI is a fast and powerful system for determining flaws and damage in a structure. The system can measure deformation/strain for a variety of situations. But, the system cannot provide the engineer with a determination of how the structure will react to a changing force which has not been measured. The theoretical model, on the other hand, normally does not have a precise fit to the real structure, and this reduces the model's usefulness. The model needs to be coupled with experimental data to provide a more accurate picture of the actual structure. The practical use of ESPI/ES can be enhanced by integrating its measurements with numerical models, for example, FEM models. One ongoing project in our lab is to integrate the experimental results from ESPI measurements with FEM model to predict the operation life of natural gas tanks.

ESPI is also a very valuable tool for experimental verification of results obtained by numerical methods such as the finite element method (FEM) [Kardestuncer and Pryputniewicz, 1984]. The accuracy of the results obtained from FEM depends on many factors such as: (1) the approximation of numerical formulation of the problem, (2) the accuracy of the imposed boundary conditions, (3) the accuracy of material properties input, and (4) the shape and size of the element used. One of these applications is in vibration analysis [Brown and Pryputniewicz, 1992; Klausbruckner and Pryputniewicz, 1992; Chai et al. 1993].

2.12.2 Medical application

ESPI is potentially useful for many biomedical applications [LØkberg 1991]. Special problems presented in biomedical application for ESPI and HI are: (1) the objects are likely unstable in time, (2) the experimental time may be limited, (3) the fringe quality is normally low. In biomedical objects, the scattering may well be taking place from discrete bodies within the object rather than from the surface of the subject. Moreover, there is a correlation between the color, the wavelength and the degree of speckle fluctuation observed. In general, fluctuations are more pronounced when the color of the laser light is the same as the color of the subject, less so when the colors are complementary. The colors of HeNe laser radiation and Argon ion laser radiation are complementary. There is also an angular effect, the speckle fluctuations being less pronounced around the specular reflection direction [Briers 1991].

ESPI applications in the biomedical area include, for example, imaging through tissue using electronic holography and femtosecond pulses [Leith et al 1991]. ESPI was used for analysis of the damage models of craniofacial regions for human body injury study [Chen 1990]. Bioengineering materials were evaluated using ESPI [Sciammarella, Bhat, and Albertazzi 1991]. ESPI has been tested in hemodynamics to visualize vessel blood flow [Tyrer and Versteeg 1992].

(4) Environmental

Both HI and ESPI have been used for environmental diagnostics of construction and cultural stone monuments [Hinsch 1991]. HI was used to examine the evolution of internal stresses in a composite construction material (bilayered laminate glass/resin) [Wippler et al 1988]. The optical head of a miniaturized ESPI system was attached to the object under test to measure the deformation of the construction material [Gülker et al 1990, 1991]. This system used diode lasers and a 3-D measurement construction. By directly coupling the system to the test object, the rigid body motion of the object is eliminated. The environmental disturbances are minimized due to the very short optical path between the object and the optical head.

(5) Arts

ESPI has been employed for artwork surface inspection to detect defects in deterioration studies of some master-pieces [Paoletti and Spagnolo 1993].

(6) Contouring

Contouring is one of application areas of ESPI: basic references in this topic can be found in the book by Jones and Wykes [1989]. Some recent advances have been involved with optical system development, the use of phase measurement techniques, diode lasers etc [Diao 1992a, 1992b, 1993, Peng 1992a, 1992b, 1993, Zou 1993].

(7) Recent applications of HI

The most powerful advantage of ESPI over HI perhaps is its real-time capability, while the biggest strength of HI is its high spatial resolution. ESPI can not totally replace HI. Therefore, there are still many applications where an HI system is used. Certainly, it may be because an ESPI system is simply not available. For reference purpose, some recent activities in the applications of HI are listed here. HI can be applied in electronics industry as a sensitive and accurate method of locating manufacturing and assembly flaws in a wide range of electronics, from individual components to assembled modules [Wood and Trolinger 1990]. Some practical applications of HI in industry were described by Sollid [1975], Parker and Jones[1988], Gryzagoridis [1992] among others. The fracture process in cement-based materials was studied using HI [Castro-Montero, Shah, and Bjelkhagen 1990]. Small changes in the tilt of an object was studied using the fringe density from HI [Rao et al 1987]. Kasprzak and Sultanova [1994] reported using a simple HI method to investigate the Poisson coefficient and elasticity moduli. Photothermal plastic recording media was used. HI and FEM were used together to study the 3-D displacement and strain of a vibrating plate [Lee et al 1992]. FEM and HI were used in a investigation of a submillimeter cantilever beam of variable cross section for its vibration mode shapes

[Brown and Pryputniewicz 1992]. A variable focus, large aperture microscope imaging lens with a magnification of about 100 was used. Vibrational analysis of an aircraft winglet was accomplished by pulsed laser holographic interferometry using double pulsed ruby laser (10 J) and thermoplastic recording [Caponero 1992]. The effects of cutouts on the dynamic response of curved rectangular composite panels were investigated by Cyr et al [1988]. The residual stresses due to curing in a spin-coating polymide film may be determined using the solution to the problem of a vibrating membrane and the vibration characteristics from HI [Maden and Farris 1991]. Fracture mechanics was studied using HI by Miller et al [1991]. HI was used to observe noninvasively the embryonic behavior in chicks [Rastogi et al 1989]. HI could be used to estimate the displacement at debondings in FRP below submicrometer order and to measure Poisson's ratios of FRP plates [Kimoto et al. 1990]. Vacuum stressing for NDE of composite laminates using HI was carried out by Rubayi and Liew [1989]. Photo thermoplastic film is readily used in real-time HI for NDE applications [Newman 1986]. HI has been used in biomedical research for many years, and there are many advances in this area [Soares et al 1991; Maeta et al 1991; Ebbeni 1991; Kojima et al 1991; Smigielski et al 1992; Silvennoinen et al 1992; Katsuma et al 1992], among others.

CHAPTER III

ES SYSTEMS

3.1 Introduction

Electronic shearography (ES) is an electronic generation of traditional film based shearography. Compared with ESPI, ES is much less susceptible to environmental noise and rigid body motion because it is a common-path interferometer; that is, the object beam and the reference beam share a common-path. Moreover, ES measures the derivative of the displacement, whereas ESPI measures the displacements. However, many techniques used in ESPI such as the phase measurement and image processing techniques are equally applicable to ES. Therefore, these techniques will not be discussed here.

ES employs an image-shearing camera which produces a pair of laterally sheared images in the image plane. Since the object to be tested is illuminated with coherent light, the two sheared images interfere with each other producing a speckle pattern (image). When the object is deformed, this speckle pattern is modified like in ESPI. By comparing the two speckle images before and after deformation, or of two different stress states of the object, a fringe pattern representing the derivative of the out-of-plane displacement with respect to the shearing direction is obtained. One important application of shearography is NDE, for example, the inspection of aerospace and automotive structures. Since flaws in an object can cause strain concentrations when the object is deformed, flaws may be revealed as some anomalies in the fringe pattern. Strain/stress concentration caused by flaws and damage can trigger premature failure of components, especially the stress concentrations on the surface or subsurface.

In comparison with ESPI, the advantages of ES are:

- Much relaxed requirement for vibration isolation.
- Simpler optical setup.
- Much reduced coherence length requirement on the laser.
- Easily controlled range of sensitivity.
- Measures displacement gradients instead of displacement. Rigid body motion does not produce strain, ES is insensitive to rigid body motion. However, rigid body motion can course speckle decorrelation if it exceeds a certain limit.

The disadvantages of ES are:

- Poor fringe visibility (noisier fringes). ES is more sensitive to speckle decorrelation.
- Difficulties in automatic quantitative fringe interpretation.
- The accuracy of the measurement is inversely proportional to the amount of shearing, but the sensitivity of the measurement is proportional to the amount of shearing.

In the following discussion, we will start first with the film-based shearography.

3.2 Film-based shearography

As illustrated in Figure 3.1, the information recording is done by the interference between two sheared images. The two sheared images are produced by a shearing device normally integrated with the imaging lens. Because of the shearing effect, light coming from two separate neighboring points p_1 and p_2 on the object interfere with each other at the image plane.

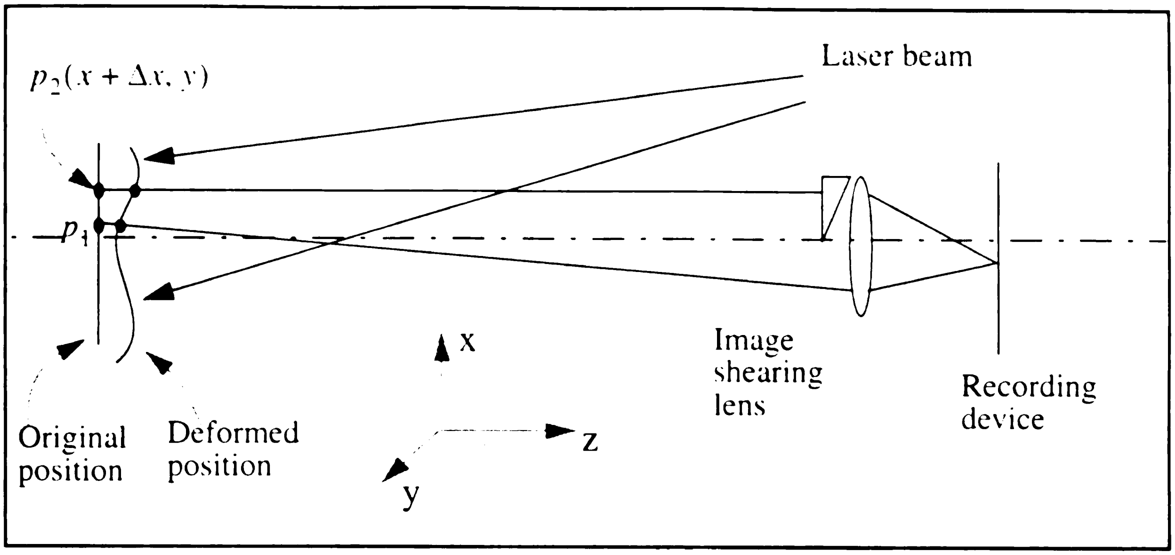

Fig. 3.1 Schematic for a typical shearography setup.

For a lateral shear in the x-axis (direction), the interference speckle pattern produced by the two sheared images is given by

$$I_{before}(x, y) = I_1(x, y) + I_2(x + \Delta x, y) + 2\sqrt{I_1(x, y)I_2(x + \Delta x, y)}\cos\phi \qquad (3.1)$$

where I_{before} is the intensity distribution of the initial image, Δx is the amount of shearing on the object side, and ϕ is the phase difference between I_1 and I_2, which are the intensity distributions of the two speckle patterns produced by the shearing-imaging system. When the two laterally sheared images are identical except for a geometrical mismatch, the shearing is intensity-balanced. Intensity-balanced shearing will result in the best fringe visibility for an ES system.

When the test object is deformed or is further deformed, assuming that I_1 and I_2

remain unchanged individually, the interference combination of I_1 and I_2 will be changed owing to the phase change. We have for the second (deformed) stage

$$\begin{aligned} I_{after}(x, y) &= I_1(x, y) + I_2(x + \Delta x, y) \\ &\quad + 2\sqrt{I_1(x, y)I_2(x + \Delta x, y)}\cos[\phi + \Delta\phi] \end{aligned} \tag{3.2}$$

where I_{after} is the intensity distribution after deformation, and $\Delta\phi$ is the relative phase change due to the relative displacement between points $p_1(x, y)$ and $p_2(x + \Delta x, y)$.

In photographic shearography, a photographic film is doubly exposed sequentially to I_{before} and I_{after}. The total exposure recorded is proportional to the sum I_{sum} of the two intensity distributions, that is

$$\begin{aligned} I_{sum} &= I_{before} + I_{after} \\ &= 2(I_1(x, y) + I_2(x + \Delta x, y)) \\ &\quad + 4\sqrt{I_1(x, y)I_2(x + \Delta x, y)}\cos\left(\phi + \frac{\Delta\phi}{2}\right)\cos\left(\frac{\Delta\phi}{2}\right) \end{aligned} \tag{3.3}$$

where ϕ and $\Delta\phi$ are functions of $(x, y, \Delta x)$. The dark fringes appear when $\Delta\phi = (2n + 1)\pi$, and the white fringes appear when $\Delta\phi = 2n\pi$, where $n = 0, 1, 2, 3, \ldots$.

Note that the fringe information is masked by the DC components of the signal (I_1 and I_2). To reveal the fringes, a high-pass Fourier filtering process is used [Hung and Taylor 1974; Hung 1982]. This setup is shown in Figure 3.2. The developed film is placed in the input plane. In this process, the DC component and the low frequency components are blocked by placing a stop on the axis at the Fourier filtering plane. When reimaged by the imaging lens onto the output-image plane, the fringes are revealed. A white light source is normally used for this process to minimize the speckles in the output fringe pattern. In the past, compared with HI, film based shearography was less used.

One of the reasons is that a Fourier filtering process is required for the readout of fringe pattern, which complicates the experiment and delays the output of the test results.

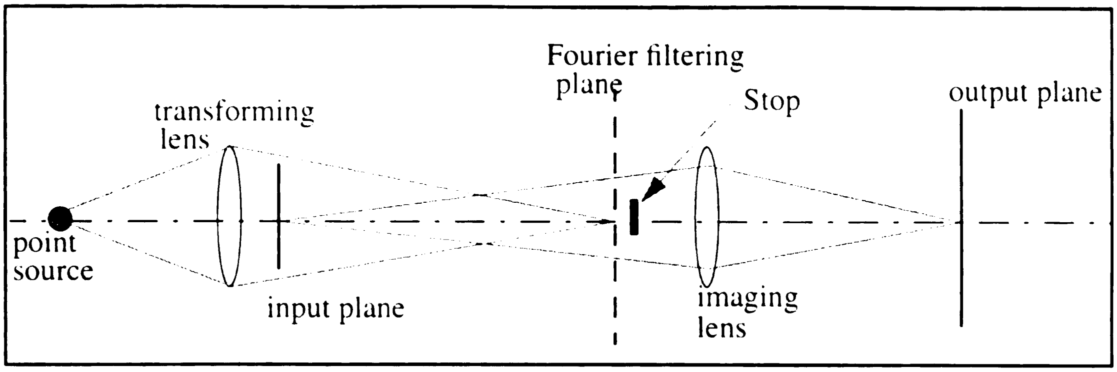

Fig. 3.2 High-pass Fourier filtering for film-based shearography.

3.3 Electronic shearography (ES)

To obtain the fringe formation in ES, as in ESPI, a CCD camera is used as the recording device in Figure 3.1 and the electronic subtraction method is utilized instead of the "addition + Fourier filtering" method used in film based shearography. Similar to ESPI, an initial speckle pattern is taken and stored in a computer. Then the object under test is deformed or further deformed. The subsequent speckle patterns are subtracted from the stored speckle pattern to generate fringes which depict the relative displacement between two neighboring points over the entire viewing area. The subtraction result I_{sub} of the two intensity distributions is given by

$$\begin{aligned} I_{sub} &= I_{after} - I_{before} \\ &= 4\sqrt{I_1(x, y)I_2(x + \Delta x, y)}\sin\left(\phi + \frac{\Delta\phi}{2}\right)\sin\left(\frac{\Delta\phi}{2}\right) \end{aligned} \tag{3.4}$$

In this process, the DC components are removed by the subtraction process. When $\Delta\phi = 2n\pi$, n = 0, 1, 2, 3, ..., we have dark fringes. In comparisoning equation 3.3 and 3.4, note that there is a $\frac{\pi}{2}$ phase difference between the photographically obtained fringes and the electronically obtained fringes. Again, the result (the fringe pattern) is a function of the relative phase change $\Delta\phi$ between two neighboring points and the amount of shearing Δx.

The relationship between observed fringes and the derivatives of displacement requires incorporation of the sensitivity vector. This matter is discussed in section 4.2.

3.4 Image shearing methods

In ES, the interference is between two sheared images. In order to produce these two images, many types of shearing cameras have been developed, ranging from very simple device (a glass wedge) to fairly complex designs.

(1) Glass wedge

In this method, as shown in Figure 3.3, a glass wedge is placed in front of the imaging lens to produce two laterally sheared images [Hung and Liang, 1979]. Possible problems are the sheared images are tilted resulting in a variable defocus across the image field and hence loss of contrast. The amount of shearing on the object plane is given by $\delta x = z(\mu - 1)\alpha$, where z is the object distance from the object to the lens, μ is the refractive index of the wedge and α is the angle of the wedge.

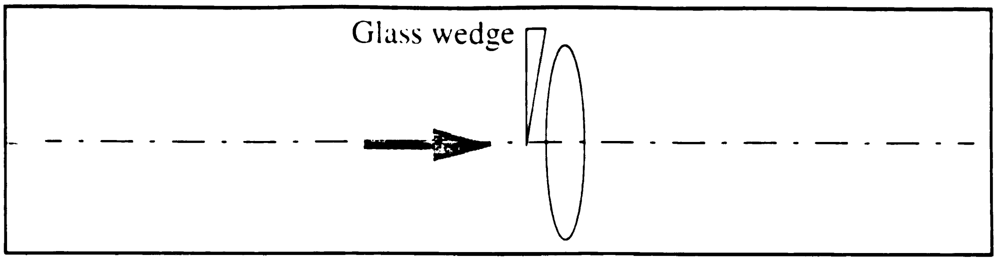

Fig. 3.3 Glass wedge shearing.

(2) Parallel glass plates

The first version of a shearing camera consisted of a lens having two apertures with an inclined piece of glass inserted in front of each aperture [Hung and Taylor, 1974]. See Figure 3.4. An improvement was made to obtain a variable shearing by Klumpp and Schnack [1990]. Note that this two-aperture setup is sensitive to the in-plane displacement of the object while the single-aperture method is not susceptible to in-plane displacement [Iwahashi et al, 1985]. This is because the two-aperture system has two different observation directions.

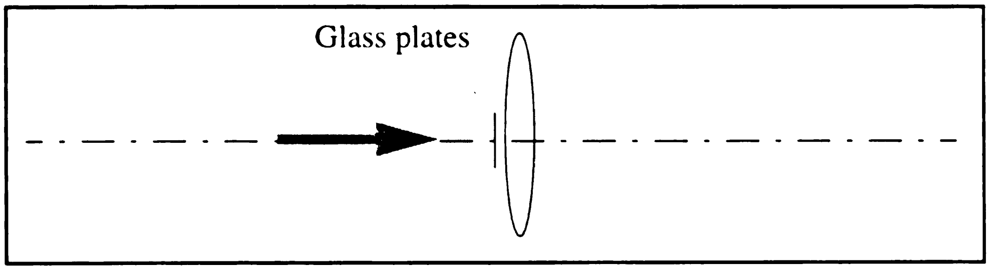

Fig. 3.4 Glass plates shearing.

(3) Fresnel Biprism

A simple and practical shearing method can easily be made by placing a Fresnel Biprism in front of the imaging lens [Nakadate et al, 1980a]. As shown in Figure 3.5, this is closely related to the glass wedge method, The amount of shearing can be calculated from $\delta x = 2z(\mu - 1)\alpha$, where all the parameters have the same meaning as in the case of a glass wedge.

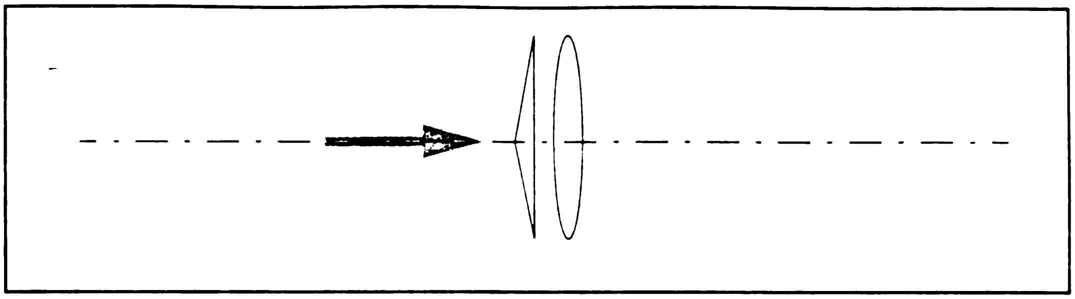

Fig. 3.5 Fresnel biprism shearing.

An advantage of using Fresnel biprism instead of wedge for image shearing is that the modulation effect of in-plane displacement fields on the desired displacement derivative fringes may be suppressed due to decorrelation [Ng and Chau, 1992].

(4) Shearing Michelson interferometer

The shearing Michelson interferometer is obtained by means of a relative tilt between the two mirrors [Leendertz and Butters 1973; Hung 1974; Ganesan et al. 1988]. As evident in Figure 3.6, the amount of shearing can be controlled easily by tilting mirror #1. The phase-shifting technique can also be implemented easily by attaching a PZT device to mirror #2.

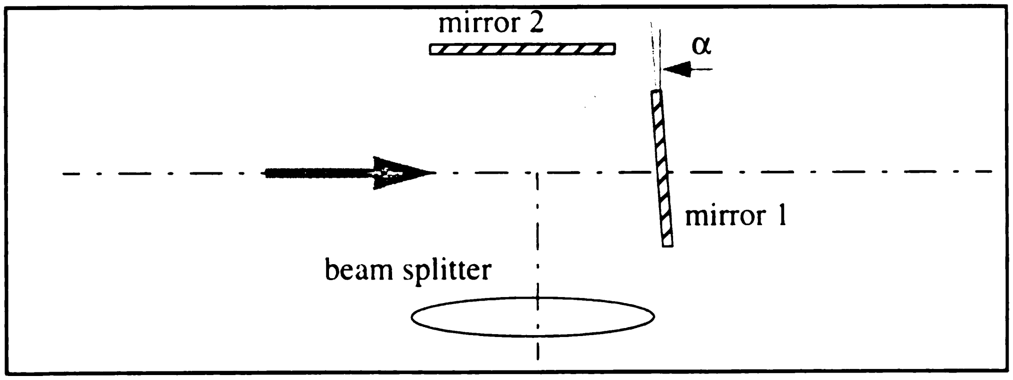

Fig. 3.6 Shearing Michelson interferometer.

(5) Split lens

As shown in Figure 3.7, a lens can be cut along a line of diameter, and then separated to obtain two laterally sheared images [Murthy, Sirohi, and Kothiyal 1982; Joenathan and Torroba 1990]. The amount of shearing at the object plane is given by $\delta x = \frac{d(1+M)}{M}$, where d is the separation of the two half lenses and M is the magnification of the imaging system. The lens serves the dual purpose of imaging and shearing, thus dispensing with additional optical shearing elements. Shear along any direction in the image plane can be achieved by a proper combination of x and y displacements of the lens halves. The displacement of one of the lens segments along the z direction results in radial shear.

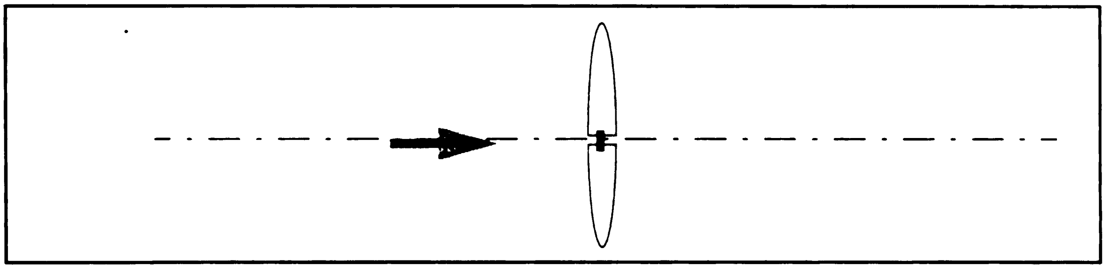

Fig. 3.7 Split lens shearing.

(6) Diffraction gratings

In this system, as shown in Figure 3.8, two different constructions may be used. In the first, two identical diffraction gratings are attached directly to the front of the lens [Hariharan 1975]. With the two gratings in contact and with their rulings parallel to the x axis, the two first-order images coincide; and a single image of the test object is formed in the image plane. If, however, the two gratings are rotated in their own plane in opposite directions through equal small angles $\pm\delta\varphi$, two sheared images are obtained. The amount of shearing between the two images is given by $\delta x = 2d_m \delta\varphi \sin\phi$, where d_m is the distance between the image and the lens. ϕ is the angle of diffraction, which should be large enough to avoid overlap of the first-order diffracted images with the directly transmitted image. In the second construction, a single grating is placed in front of the image plane at a distance away from it. The grating divides the imaging wave coming from the object into two diffracting waves [Iwahashi, Iwata, and Nagata 1984].

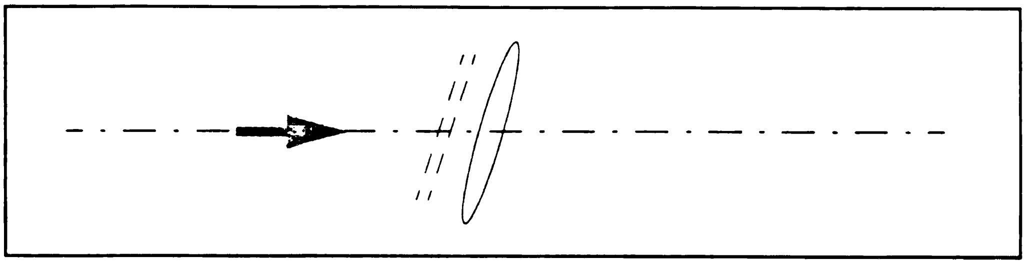

Fig. 3.8 Shearing using diffraction gratings.

(7) Defocus setup

The shearing is obtained by misfocusing and using two apertures [Hung, Rowlands, and Daniel 1975]. This technique is not practical owing to the very poor fringe visibility.

(8) Wollaston prism

In this application, see Figure 3.9, a Wollaston prism is normally used in a reverse way in which two beams separated by a small angle on the left of the prism will meet at the right side of the prism. That is, the shearing device causes two nonparallel beams scattered from two different points on the object surface to become collinear or nearly collinear when they emerge from the prism. As a result, the spatial frequency of the speckle pattern is lowered; and a larger aperture may be used in the CCD camera [Hung 1994]. The device uses the fact that the output from a Wollaston prism is two polarized beams; they are not only separate but also orthogonally polarized from each other [Françon 1966]. The angular shearing is given by $\alpha = 2(n_o - n_e)\tan\theta$, where n_o and

n_e are the refractive indices of the prism (for quartz, $n_o = 1.5443$, $n_e = 1.5534$), and θ is the top angle of the prism. Therefore, the amount of shearing is $\delta x = 2z\tan\left(\frac{\alpha}{2}\right)$, where z is the distance from the object to the lens. Since the two sheared wavefronts transmitted by the two axes of the birefringent crystal are orthogonally polarized, a polarizer Q oriented at 45^0 to the crystal's axes is needed to make the two beams interfere. The amount of shearing may be altered in some degree by translating the prism [Bao, Jin, and Chung 1993]. To employ the phase shifting technique, a rotatable polarizer can be used to make the phase changes between the two interfering beams [Jin, Bao, and Chung 1994].

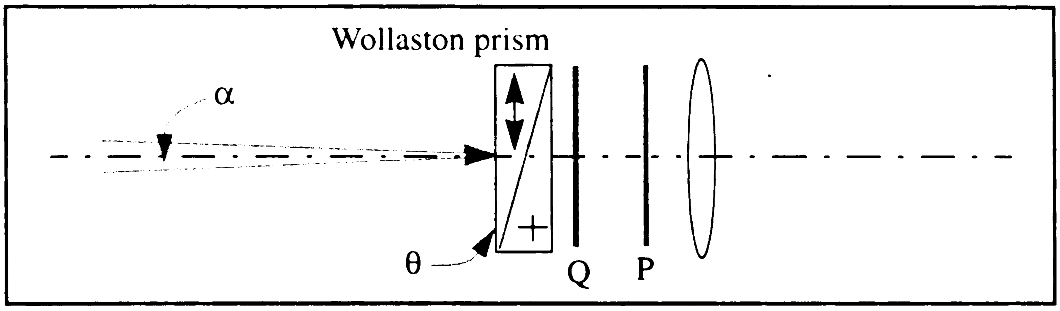

Fig. 3.9 Shearing use a Wollaston prism.

Comments on various shearing methods:

The amount of shearing should exceed the size of the speckles for ES to work. Although ES is not susceptible to rigid body motion, the object deformation-induced speckle decorrelation is more likely to occur than in ESPI. Some of the devices, including the Wollaston prism [Bao et al. 1993], split lens [Murthy et al. 1982], and parallel glass plates [Klumpp and Schnack, 1990], offer variable shearings which provide different measurement sensitivities. Besides lateral shear, some shearing designs can provide a number of shearing types such as radial shear, rotational shear, and folding shear [Ganesan et al. 1988; Murthy et al. 1982].

In Michelson's interferometric arrangement and the methods using wedges, the sheared images are tilted, resulting in a variable defocus across the image field, and this can cause the loss of fringe contrast. To achieve the best fringe visibility for any setup, the two sheared images should have equal intensity distribution.

The first and the second derivative of the displacement may be recorded simultaneously with three-aperture speckle shearing interferometer [Sharma, Sirohi, and Kothiyal 1984].

The fringe contrast in ES is normally not as good as that in ESPI. A way to obtain high contrast fringes is to employ nonlinear processing such as level slicing or level windowing on the subtracted image [Nakadate et al, 1980]. Level slicing maps the gray levels less than a certain threshold into the zero level and the levels greater than or equal to the threshold into the highest level. Level windowing maps the gray levels within the two threshold levels into the highest level and otherwise into the zero level. When nonlinear image processing is used, an aperture larger than that required by the detector resolution can be used [Ganesan et al, 1988]. If sufficiently high fringe density can be obtained, it is possible to obtain second derivatives of plate deflection by the moire effect of two identical fringe patterns superposed and shifted with respect to each other, just like obtaining the first derivative from displacement fringes [Leendertz and Butters, 1973].

3.5 Automatic quantitative fringe interpretation

Phase shifting techniques described in Chapter Two for ESPI are equally applicable for ES. Due to the common-path interferometry design, some of the ES optical setups are not suitable for implementing phase shifting techniques, an example being the Fresnel biprism design. The shearing Michelson interferometer and the Wollaston prism designs are suitable for phase shifting techniques. The automatic quantitative fringe analysis of ES is not as well developed as that of ESPI. Moreover, in comparison with the fringes in ESPI, ES fringes are inherently nosier.

A few reports have been published for the extraction of phase information in ES. Some used spatial phase measurement techniques [Hung et al. 1990b; Templeton and Hung 1989], and others employed temporal phase measurement methods just like the methods used in ESPI [Nakadate and Saito, 1985; Hung 1994a; Toyooka and Kadono, 1990; Jin et al. 1994]. The phase measurement algorithms used in ESPI can be adopted for use in ES. The key to apply these algorithms is to make the appropriate phase shifts. In Nakadate's method, a shearing Michelson interferometer was used. A PZT device is attached to one of the mirrors to create the phase-shifting. Hung's technique obtains the phase shift by tilting the direction of the illumination using a rotational mirror. Tilting the illumination introduces a phase change of linear variation in the wavefront. Since the derivative of a linear function is a constant, a uniform phase change is introduced in the shearogram. It is worth pointing out that a collimated illumination beam has to be used to introduce the uniform phase shift, which was not mentioned in Hung's paper. For diverging illumination, a non-uniform phase shift will be produced. Toyooka's technique used a liquid crystal cell which was inserted in front of the lens. The cell can be controlled to introduce required phase shifts independently into the divided beams in the glass-wedge shearing camera. The problem with this technique is the unexpected phase shift caused by environmental temperature variation. In Jin's method, the phase shift is achieved by using a polarization technique. A Wollaston prism, a quarter-wave plate and a polarizer were used in the system. The rotatable polarizer is controlled by a computer and a step motor to introduce the phase changes.

Due to the interference between two speckle images, the interferogram is deteriorated (more noisy) in comparison with an ESPI interferogram. These interferograms need to be low-pass filtered to reduce speckle noise. Normally, several iterations of median window (normally 3x3 to 11x11) filtering are necessary. A different filtering method utilizing 2-D FFT was suggested by Jin and Tang [1992], and it is superior to the space domain methods but requires longer computation time.

3.6 Applications

ES is sensitive primarily to changes in the derivative of the out-of-plane displacement. The fringe patterns are somewhat more difficult to interpret than those from ESPI. However, fringe patterns of displacement derivatives often can provide more useful information about a structural flaw for many NDE applications [Hung 1989b]. The most important application for ES is, perhaps, NDE. For NDE application, flaws in structures usually cause strain concentrations which will create anomalies in the fringe pattern, especially when the flaw is in the surface or near the surface. Surface flaws are most responsible for premature fracture and fatigue failure.

Some examples of applications in NDE are: (1) Evaluation of the integrity of aircraft and automotive tires. In this testing, the tire is placed in a chamber and a partial vacuum is applied as a means of loading [Hung 1982]. (2) The detection of residual stresses in an industrial environment [Hung et al. 1990a]. The approach is based on measuring the derivative of the out-of-plane displacement relieved by a surface indentation. (3) Some applications of ES are in the aircraft industry, where ES has been used for NDE of fuselage panels and thermal protection shields [Safai 1992, 1993], and airskin structures

[Deaton and Rogowski, 1993]. (4) Shearography has also been used for the detection of delaminations and other flaws in composite laminates [Anastasi et al. 1987; Chau et al, 1989; Shang, Lim, and Lim 1991; Hung 1993].

Besides NDE applications, ES has been used in the characterization of microlenses. The system is a modified Michelson shearing interferometer with one mirror mounted on a PZT for using phase shifting technique and another mirror mounted on a rotatable stage for varying the amount of tilt [Sickinger et al. 1994]. Some comparative studies involving ESPI, ES, ultrasound, LDV, and FEA methods have been reported [Moslehy, Mueller, and Davis 1993; Hsu et al., 1993; Pryputniewicz 1992b].

The sensitivity of shearography can be varied by changing the amount of shearing. As the shearing increases, the fringe density also increases. However, the apparent area of the flaw may be expanded in the shearing direction as the shearing increases. When the shearing reaches one half of the size of the flaw, a single flaw would look like two separated flaws in the direction of shearing. Normally, the center of the flaw is located at the geometric center of the flaw-induced fringe anomaly. One must be careful to account for this effect when estimating the actual size of a flaw. Moreover, because the amount of shearing is equivalent to the step-length of taking numerical differentiation, the greater the shearing the less accurate the result (the derivative of the displacement). When shearing is large, the two points which interfere with each other will have very different sensitivity vectors. The approximations in equation 3.14 will not hold correctly. As the amount of shearing is further increased, the optical system will deviate from a truly "common-path" interferometer. A high value of shearing also reduces the tolerance to environmental disturbances. Therefore, there is an optimum amount of shearing for a certain flaw. To increase the versatility of ES, a variable shearing capability is highly desirable.

As with ESPI, one way to maximize the efficiency of the inspection is to increase the field of view, that is to cover a larger test area. However, one should bear in mind that the desire to increase the field of view is at the sacrifice of losing spatial detection sensitivity to resolve the small flaws. The detection resolution is inversely proportional to the area of the inspection. Therefore, the field of view (the covered inspection area) should not be set so large that the number of pixels sampling the flaw profile in the image is reduced to the point where a critical small flaw can no longer be resolved.

As with all speckle interferometry techniques including shearography, a limitation is that the occurrence of rigid body motion produces decorrelation of speckles. This effect will result in deterioration of fringe visibility. If the rigid body motion is excessive, no fringe can be observed. Some research has been done in the area of compensating for the influence of rigid body motion both for ES and ESPI [Hung, Wang, and Hovanesian 1994]. Hung's method is based on translation of camera or digitally shifting one of the speckle patterns.

To improve the fringe quality in ES, besides using digital filtering, a fringe sharpening technique involving recording many frames of the object with the object loaded equally and in increasing steps between exposures has been studied [Ganesan et al.1988]. A continuous deformation may be studied using a real-time interval technique that uses a variable updating reference pattern in the subtraction process.

CHAPTER IV

SENSITIVITY VECTOR ANALYSIS OF THE SYSTEMS

As pointed out in the previous Chapters, the quantities measured in ESPI and ES have a close relationship with the sensitivity vectors of the optical setups in terms of the accuracy of the measurements and the sensitivities of the systems to the quantities being measured. In this chapter, we will discuss in detail the sensitivity vectors of various optical setups related to ESPI and ES systems. A coordinate system that is found to be the best suited to the purpose will be introduced for systematically analyzing the sensitivity vectors.

4.1 Analysis for ESPI systems

In Chapter Two we discussed a number of possible error sources in the measurements. These errors may come from light source instability, quantization of the signal, nonlinearity of the CCD device, nonlinearities in the phase shifter movements, calibration of the phase shifter, phase drifting during the measuring interval, mechanical vibration, and air turbulence. Errors may also be introduced during the phase unwrapping process by the noise (speckle and electronic noise) in the fringe pattern. However, through careful selection and calibration of the devices, and using appropriate phase calculation algorithms, the errors can be reduced to a negligible level if not removed completely.

Besides the above mentioned error sources, the most obvious and the most neglected source of errors in practice is inherent in the sensitivity vector of the ESPI optical setups. The concept of the sensitivity vector is well known [Vest 1979]. The sensitivity vector is a function of the relative positions of the test object, the illumination, and the observation. It is a parameter which dictates the measurement sensitivity to the quantity being measured. An ESPI system can be configured into either an out-of-plane displacement sensitive setup or an in-plane displacement sensitive setup. Note that the "out-of-plane sensitive" does not mean that the setup only measures the out-of-plane displacement, it means only that the setup is much more sensitive to the out-of-plane displacement component than it is to other displacement components. The same is true for the in-plane sensitive setups. Inappropriate assumptions and approximations about the sensitivity vector in the phase calculation can result in big errors in the final result, which is, normally, the displacement contour map. Therefore, to understand the characteristics and the magnitude of potential errors, a detailed investigation into the effect of the sensitivity vectors on the measurements is needed.

In using ESPI for engineering measurement, one has to understand what are the quantities really being measured and how big are the possible errors from the approximations of the sensitivity vectors. In the following discussion, a systematic and detailed treatment of the sensitivity vectors and their effect for various ESPI setups is presented. Methods for reducing or correcting the measurement errors are suggested.

A schematic diagram is shown in Figure 4.1 for the sensitivity analysis of the measurement. The origin of the right-hand coordinate system is located at the center of the entrance aperture of the imaging lens (the observation). The z-axis is chosen to be the optical axis. $P(x, y, z)$ is a point on the test object. $S(x_i, y_i, z_i)$ is the illumination

$\vec{R} =$

where

source. In ESPI, point P(x, y, z) may be considered to be the center of the resolution element on the object surface. If a CCD having 512 x 512 sensing cells is fully used, 262144 sample points each from a resolution element on the object are measured. The average size of a resolution element on the object is given by

$$s = \frac{1.22(1+M)\lambda F}{M} \tag{4.1}$$

where λ is the wavelength of the light, M is magnification of the imaging system, and F is the *f*-number of the imaging system. In the following discussion, "point" means the center point of a resolution element.

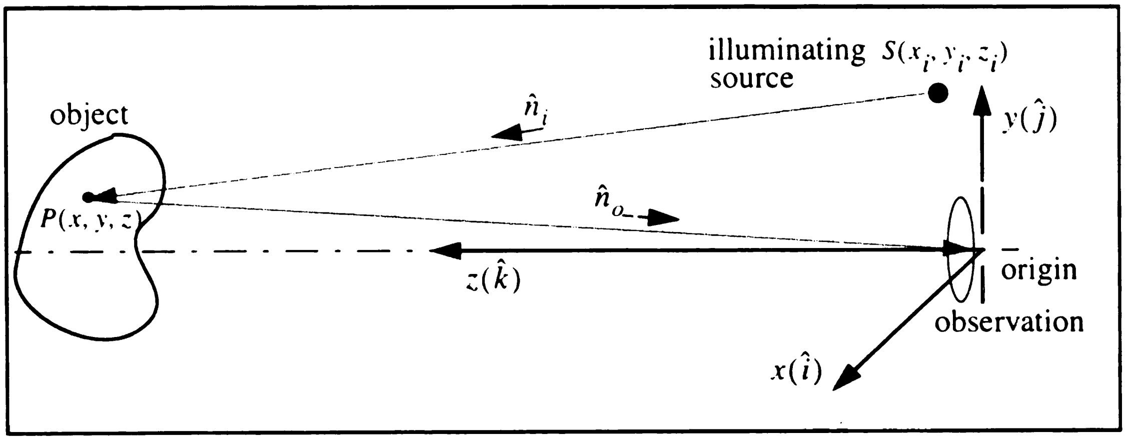

Fig. 4.1 Schematic diagram for sensitivity vector analysis.

For single-beam illumination, the sensitivity vector $\vec{K}$ is defined as [Vest 1979]

$$\vec{K} = \frac{2\pi}{\lambda}(\hat{n}_i - \hat{n}_o)\ , \tag{4.2}$$

where $\hat{n}_i$ is the illumination propagation unit vector and $\hat{n}_o$ is the observation propagation unit vector.

For double-beam illumination, $\vec{K}$ is given by

$$\vec{K} = \frac{2\pi}{\lambda}(\hat{n}_{i1} - \hat{n}_{i2}) \ . \tag{4.3}$$

where $\hat{n}_{i1}$ and $\hat{n}_{i2}$ are the two illumination propagation unit vectors for the two illuminating beams respectively.

The propagation unit vectors can be calculated for each point on the object from the coordinates of the illuminating source, the point on the object, and the center of the entrance aperture of the imaging lens. They are given by

$$\hat{n}_o = -\frac{x\hat{i} + y\hat{j} + z\hat{k}}{\sqrt{x^2 + y^2 + z^2}} = n_{ox}\hat{i} + n_{oy}\hat{j} + n_{oz}\hat{k} \tag{4.4}$$

$$\hat{n}_i = \frac{(x - x_i)\hat{i} + (y - y_i)\hat{j} + (z - z_i)\hat{k}}{\sqrt{(x - x_i)^2 + (y - y_i)^2 + (z - z_i)^2}} = n_{ix}\hat{i} + n_{iy}\hat{j} + n_{iz}\hat{k} \tag{4.5}$$

where n_{ix}, n_{iy} and n_{iz} are the x, y and z components of the $\hat{n}_i$ propagation unit vector respectively. n_{ox}, n_{oy} and n_{oz} are the x, y and z components of the $\hat{n}_o$ propagation unit vector respectively. Eq. (1) can be rewritten as

$$\vec{K} = \frac{2\pi}{\lambda}[(n_{ix} - n_{ox})\hat{i} + (n_{iy} - n_{oy})\hat{j} + (n_{iz} - n_{oz})\hat{k}] \ . \tag{4.6}$$

Let $\Delta\vec{d}$ be the displacement vector at point P. The phase change caused by this displacement is given by

$$
\begin{aligned}
\Delta\phi &= \vec{K} \bullet (\Delta\vec{d}) \\
&= \frac{2\pi}{\lambda}[(n_{ix} - n_{ox})\Delta d_x + (n_{iy} - n_{oy})\Delta d_y + (n_{iz} - n_{oz})\Delta d_z]
\end{aligned}
\tag{4.7}
$$

where Δd_x, Δd_y and Δd_z are the x, y and z components of the displacement vector respectively. The sensitivity vector remains constant for a certain point because the displacement is normally very small ($\sim 15\mu m$). The sense of the components is defined according to the following rules:

(1) If the head of the projection of the unit vector on an axis is directed towards the positive direction of the axis, the corresponding component of the unit vector is positive.

(2) If the projection of the unit vector on an axis is directed towards the negative direction of the axis, the corresponding component of the unit vector is negative.

For convenience of the discussion, the following variables are also defined:

θ_{ix} = the angle between the illuminating beam and the x-axis.

θ_{iy} = the angle between the illuminating beam and the y-axis.

θ_{iz} = the angle between the illuminating beam and the z-axis.

θ_{ox} = the angle between the observation and the x-axis.

θ_{oy} = the angle between the observation and the y-axis.

θ_{oz} = the angle between the observation and the z-axis.

Note that all the angles above are acute angles. Thus, the following relations exist:

$$
\begin{aligned}
|n_{ix}| &= \cos\theta_{ix} \\
|n_{iy}| &= \cos\theta_{iy}, \\
|n_{iz}| &= \cos\theta_{iz}
\end{aligned}
\qquad \text{and} \qquad
\begin{aligned}
|n_{ox}| &= \cos\theta_{ox} \\
|n_{oy}| &= \cos\theta_{oy}. \\
|n_{oz}| &= \cos\theta_{oz}
\end{aligned}
$$

Physically, at this point, we can see that if the sensitivity vector is constant, a rigid body translation of the object will produce a uniform phase shift across the object, and no fringe pattern will be formed. When the sensitivity vector is variable, the same rigid body translation produces a fringe pattern. In the following section, the effects on the measurement caused by the varying sensitivity vectors are investigated for a number of optical setups which may be employed in an ESPI system.

4.1.1 Single-Beam illumination

Single beam illumination is normally used to set up an out-of-plane displacement sensitive measurement. In this case, the interference is between the illumination beam and a reference beam. Two optical configurations are studied.

(1) Collimated illumination

The illumination beam is collimated and parallel with the y-z plane as shown in Figure 4.2. In this case, the illumination unit vector is constant across the test area. The observation unit vectors are symmetrical around the z-axis and variable across the test area.

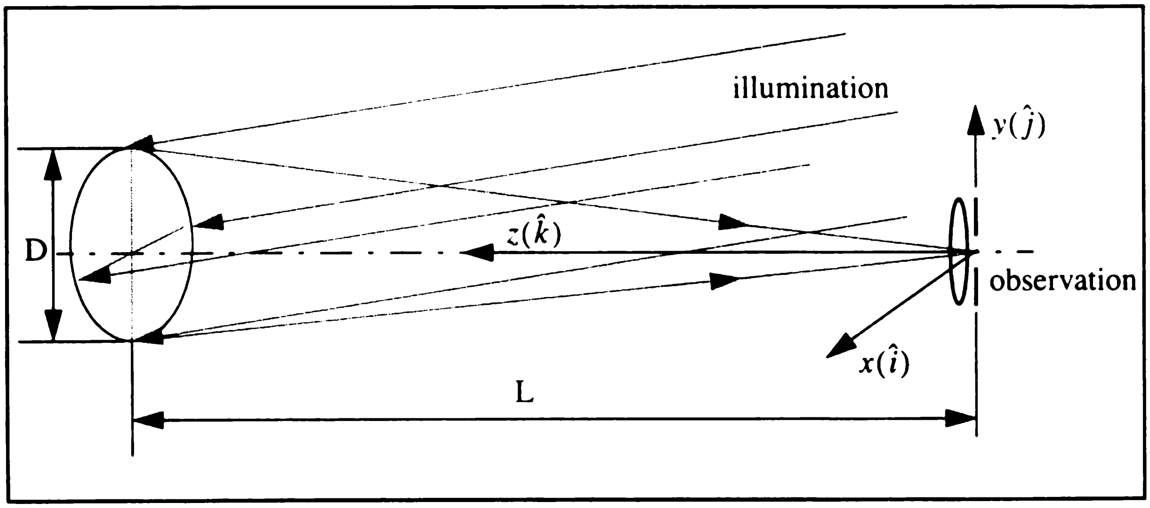

Fig. 4.2 Collimated single-beam illumination

In this setup, D is the size of the test area, and L is the distance between the object and the imaging lens. We have $n_{ix} = \cos\frac{\pi}{2} = 0$, $n_{iz} = \cos\theta_{iz}$ and $n_{iy} = -\cos\theta_{iy}$. Therefore, the sensitivity vector is given by

$$\vec{K} = \frac{2\pi}{\lambda}[(\pm\cos\theta_{ox})\hat{i} + (\cos\theta_{iy}\pm\cos\theta_{oy})\hat{j} + (\cos\theta_{iz} + \cos\theta_{oz})\hat{k}] \quad , \qquad (4.8)$$

and the phase change due to the displacement $\Delta\vec{d}$ is given by

$$\Delta\phi = \frac{2\pi}{\lambda}[(\pm\cos\theta_{ox})d_x + (\cos\theta_{iy}\pm\cos\theta_{oy})d_y + (\cos\theta_{iz} + \cos\theta_{oz})d_z] \quad . \qquad (4.9)$$

Note that there are " ± " signs before $\cos\theta_{ox}$ and $\cos\theta_{oy}$. This is because of the varying direction of the observation unit vector. n_{ox} is positive on the left hand side of the y-z plane (at x = 0) and negative on the right hand side of the plane. Similarly, n_{oy} is positive for the area below the x-z plane (at y = 0) and negative for the area above the plane. A sign map may be introduced here to illustrate the sign variations across the object plane (the x-y plane). Figure 4.3 shows the sign variations of the x and y components of the observation unit vector in each quadrant.

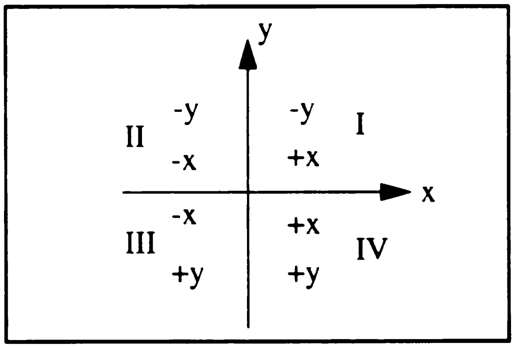

Fig. 4.3 The sign variations of the components of the observation unit vector.

The most out-of-plane displacement sensitive configuration practically achievable for a diffuse object is when θ_{iz} is zero across the viewing (test) area. Furthermore, only when θ_{oz} is also zero across the viewing area may a pure out-of-plane sensitive setup be obtained. But, this is impossible in practice. A good approximation may be obtained when: (1) the distance L between the object and the imaging lens is much greater than the size D of the test area and θ_{iz} is small. This means that $\cos\theta_{iy}$, $\cos\theta_{ox}$ and $\cos\theta_{oy}$ are approximately zero. Or, (2) the in-plane displacement components d_x and d_y are much smaller than the out-of-plane displacement component d_z. Under these approximations, Eq. (4.9) reduces to

$$\Delta\phi \approx \frac{2\pi}{\lambda}(\cos\theta_{oz} + \cos\theta_{iz})d_z \approx \frac{4\pi}{\lambda}d_z \, . \qquad (4.10)$$

where $|\vec{k}|$ is taken as constant $\frac{4\pi}{\lambda}$. This is the formula normally used in an out-of-plane displacement sensitive ESPI system.

(2) Diverging beam

In practice, it is not easy and economical to obtain a large collimated illumination beam to cover a large area. Typically, a diverging beam is used to illuminate the object. In this configuration, as shown in Figure 4.4, the sensitivity vector is given by

$$\vec{k} = \frac{2\pi}{\lambda}[(\pm\cos\theta_{ox} \pm \cos\theta_{ix})\hat{i} + (\pm\cos\theta_{oy} \pm \cos\theta_{iy})\hat{j} + (\cos\theta_{oz} + \cos\theta_{iz})\hat{k}] \qquad (4.11)$$

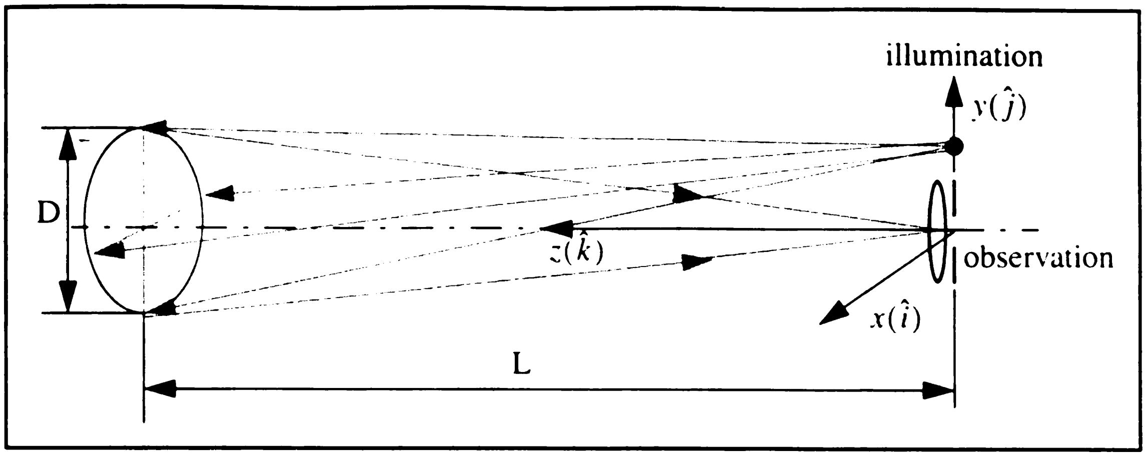

Fig. 4.4 Diverging single-beam illumination.

In this case, we not only have the sign variations in the observation beam, but also have sign variations in the illumination beam. The sign variation of the illumination is determined by the relative position of the point on the test object and the location of the illuminating source point. These result in the " ± " signs in the equation. Furthermore, the displacement components d_x and d_y can also have both positive and negative values. This results in addition or cancellation of the in-plane displacement-caused phase changes.

When the illuminating source coincides with the center of the aperture of the imaging lens, the sign variation of the illumination for each quadrant is just the opposite of the sign map of the observation. The maximum error due to the variable sensitivity vector is minimized.

A computer simulation for a typical out-of-plane displacement sensitive optical setup is shown in Figure 4.5 through 4.8 to illustrate the effect of the variable sensitivity vectors on the displacement measurement. In this example, a square 0.2 x 0.2 meter plate was used as the test object. The distance between the object and the imaging lens is one meter, and the illuminating point source is located at (0, 0.1, 0). A number of cases are examined to depict the effect of the variable sensitivity vectors on three displacement components individually, and on one case in which all three displacement components are not zero. Figure 4.5 shows the result of a displacement field of $dz = 10\mu m$, and $dx = dy = 0$. In this case, the measured result would display a non-uniform displacement from what is actually a uniform displacement. The "peak to valley" relative displacement is $0.2\mu m$, while the real relative displacement should be zero. In another word, the sensitivity factor is 100% only for the point of (0, 0, 0) on the object. On the edge of the object it falls down to 98%. The relative measurement error is, therefore, 2% on the edges and zero at the center. It also varies across the object. In Figure 4.6, the displacement of the object is $dx = 10\mu m$, and $dy = dz = 0$. The uniform in-plane displacement generated about $2\mu m$ "peak to valley" false out-of-plane displacement. The sensitivity factor varies linearly along the x-axis. At $x = \pm 0.1$, the edges of the plate, about 10% of the in-plane displacement is registered. The signature of the in-plane displacement on the out-of-plane displacement sensitive ESPI setup becomes zero only at the line of $x = 0$. The sign of the displacement changes at x = 0. On one hand, the in-plane displacement can give rise to a false out-of-plane displacement; on the other hand, the out-of-plane sensitive setup may be used to measure the in-plane displacement followed by some correction factors. Figure 4.7 is similar to Figure 4.6; in this case, the displacement is $dy = 10\mu m$, and $dx = dz = 0$. The zero sensitivity line now is shifted to y = 0.05 meter as the location of the illuminating point source is at (0, 0.1, 0). When all the displacement components are not zero, the result will include contributions from all the displacement components. An example is shown in Figure 4.8 where the displacement field is $dx = dy = dz = 10\mu m$. It results in a maximum out-of-plane displacement of $11.5\mu m$ and a minimum out-of-plane displacement $7.5\mu m$. If one wants to separate the three displacement components, at least three or more different illuminations are needed [Stetson 1990b].

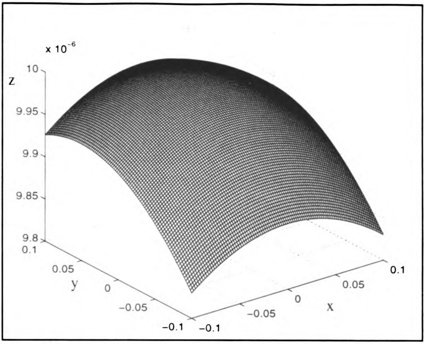

Fig. 4.5 Computer simulated measurement result for the out-of-plane ESPI setup with the displacement field $dz = 10\mu m$, and $dx = dy = 0$.

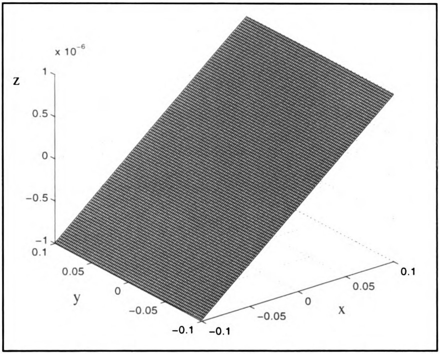

Fig. 4.6 Computer simulated measurement result for the out-of-plane ESPI setup with the displacement field $dx = 10\mu m$, and $dy = dz = 0$.

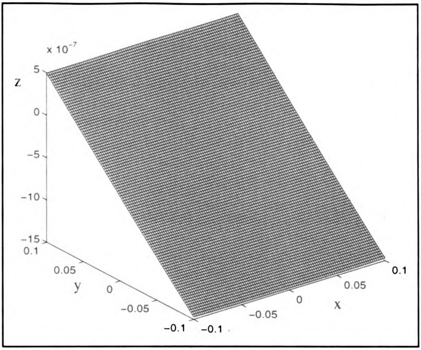

Fig. 4.7 Computer simulated measurement result for the out-of-plane ESPI setup with the displacement field $dy = 10\mu m$, and $dx = dz = 0$.

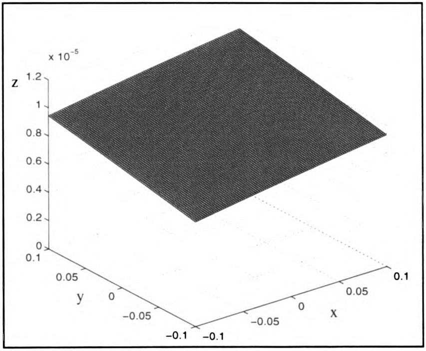

Fig. 4.8 Computer simulated measurement result for the out-of-plane ESPI setup with the displacement field $dz = dx = dy = 10\mu m$.

4.1.2 Double-Beam Illumination

Double-beam illumination is normally employed to construct an in-plane displacement sensitive setup. In this case the interference is between the two illumination beams. The sensitivity vector is given by

$$\begin{aligned}\vec{K} &= \frac{2\pi}{\lambda}(\hat{n}_{i1} - \hat{n}_{i2}) \\ &= \frac{2\pi}{\lambda}[(\pm\cos\theta_{ix1} \pm \cos\theta_{ix2})\hat{i} + (\pm\cos\theta_{iy1} \pm \cos\theta_{iy2})\hat{j} + (\cos\theta_{iz1} - \cos\theta_{iz2})\hat{k}]\end{aligned} \tag{4.12}$$

where n_{i1} is the propagation unit vector of the first illumination beam and n_{i2} is the propagation unit vector of the second illumination beam. They can be expressed as

$$\hat{n}_{i1} = \frac{(x - x_{i1})\hat{i} + (y - y_{i1})\hat{j} + (z - z_{i1})\hat{k}}{\sqrt{(x - x_{i1})^2 + (y - y_{i1})^2 + (z - z_{i1})^2}} = n_{ix1}\hat{i} + n_{iy1}\hat{j} + n_{iz1}\hat{k} \tag{4.13}$$

$$\hat{n}_{i2} = \frac{(x - x_{i2})\hat{i} + (y - y_{i2})\hat{j} + (z - z_{i2})\hat{k}}{\sqrt{(x - x_{i2})^2 + (y - y_{i2})^2 + (z - z_{i2})^2}} = n_{ix2}\hat{i} + n_{iy2}\hat{j} + n_{iz2}\hat{k} \tag{4.14}$$

Again, for convenience of discussion, the following expression will be used

$$\begin{aligned}|n_{ix1}| &= \cos\theta_{ix1} & \qquad & |n_{ix2}| = \cos\theta_{ix2} \\ |n_{iy1}| &= \cos\theta_{iy1} & \qquad \text{and} \qquad & |n_{iy2}| = \cos\theta_{iy2} \\ |n_{iz1}| &= \cos\theta_{iz1} & \qquad & |n_{iz2}| = \cos\theta_{iz2}\end{aligned}$$

where θ_{ix1}, θ_{iy1} and θ_{iz1} are the angles between the illuminating beam 1 and the x-axis, the y-axis and the z-axis respectively. θ_{ix2}, θ_{iy2} and θ_{iz2} are the angles between the illuminating beam 2 and the x-axis, the y-axis and the z-axis respectively. All the angles are acute angles. Three cases are investigated for the double-beam illumination type

ESPI.

(1) Collimated beams (symmetrical)

The configuration shown in Figure 4.9 is employed for the in-plane sensitive ESPI. The two illuminating beams are collimated and are arranged so that they are symmetrical about the x-z plane. This optical layout is used to measure the y-component of the in-plane displacement. The x-component of the in-plane displacement will not contribute to the phase changes because the illuminations are normal to the x-axis. The out-of-plane (the z-component) displacement-caused phase changes are cancelled out due to the symmetrical arrangement.

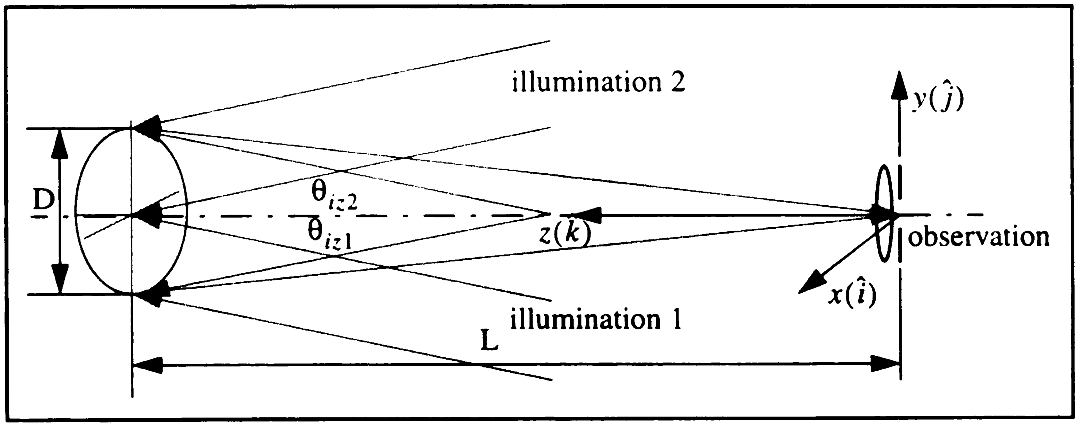

Fig. 4.9 Symmetrical collimated double-beam illumination.

In this case, the sensitivity vector is given by

$$\vec{K} = \frac{2\pi}{\lambda}(\cos\theta_{iy1} + \cos\theta_{iy2})\hat{j}, \tag{4.15}$$

thus, the phase change is

$$\begin{aligned}\Delta\phi &= \frac{2\pi}{\lambda}(\cos\theta_{iy1} + \cos\theta_{iy2})d_y \\ &= -\frac{2\pi}{\lambda}(\sin\theta_{iz1} + \sin\theta_{iz2})d_y \\ &= \frac{4\pi}{\lambda}d_y\sin\theta\end{aligned} \tag{4.16}$$

where $\theta_{iz1} = \theta_{iz2} = \theta$ and $\theta_{iy1} = \theta_{iy2}$. Clearly, the sensitivity increases with the increase in the incidence angle. Because the sensitivity vector has only non-zero $\hat{j}$ component, this setup is sensitive only to the y-component of the in-plane displacement. To obtain the actual value of the displacement, the illumination angle has to be entered into the calculation. Figure 4.10 shows the calculated uniform displacement field for dy = $10\mu m$.

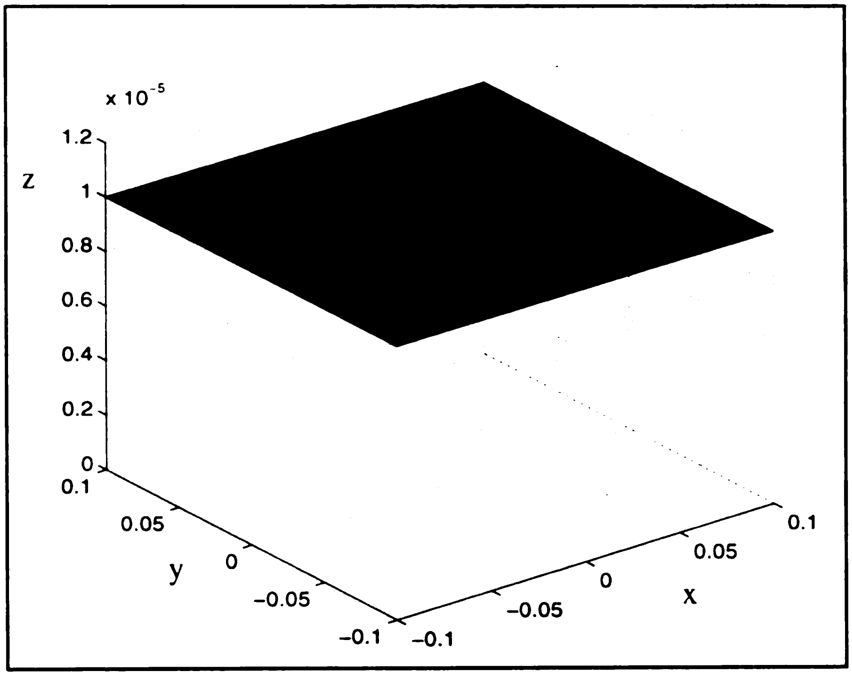

Fig. 4.10 Computer simulated measurement result for the in-plane ESPI setup using parallel beams with the displacement field $dy = 10\mu m$ and $dx = dz = 0$.

Similarly, the x-component of the in-plane displacement can be measured by rotating the two illuminating beams 90^o about the z-axis. If only one of the two beams is rotated 90^o about the z-axis, an orthogonal illumination setup is obtained. In this setup, one beam is parallel with the y-z plane and another beam is parallel with the x-z plane, both of the beams still have the same angle with the z-axis. In this case, the phase change is given by

$$\Delta\phi = \frac{2\pi}{\lambda}\sin\theta(d_y - d_x) \tag{4.17}$$

(2) Diverging beams (symmetrical)

Using two collimated beams for in-plane measurement is ideal due to the fact that the out-of-plane displacement is cancelled out. But, as mentioned before, a large collimated beam is difficult to obtain economically. When large objects need to be tested, a diverging beam is commonly used. In this case, the two beams are symmetrical about the z-axis as shown in Figure 4.11. Now, the two incident angles at a point are different except at points where y is zero. Therefore, the phase changes caused by out-of-plane displacement will not be cancelled out. Moreover, the x-component of the in-plane displacement also causes phase changes except at points with $x = 0$ or $y = 0$. In general, equation 4.12 has to be used in this case.

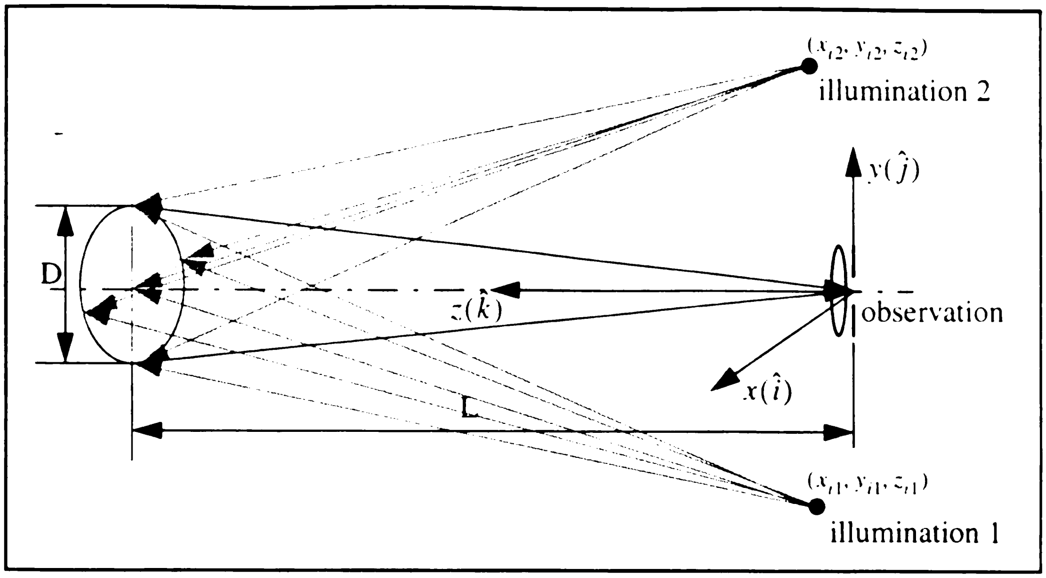

Fig. 4.11 Diverging double-beam illumination.

An example is studied below to analyze the effect of the variable sensitivity vectors. In this example, the two illuminating point sources are positioned at (0, 0.5, 0) and (0, -0.5, 0). D and L have the same values as before. The incident angles θ_{iz1} and θ_{iz2} are about 26.6 degree at the center of the object. If we use this "average" incident angle as the compensation factor for all the points on the object, the result for a displacement of $dy = 10\mu m$, $dx = dz = 0$ is shown in Figure 4.12. We can see, in Figure 4.12, the absolute displacement result for each point is very accurate with a maximum relative error of only 0.6%; the relative displacement has been distorted from an actual uniform displacement to a dome-shaped displacement. This setup has an average sensitivity factor of 99.7% to the y-component of in-plane displacement. Figure 4.13 shows the result of a displacement of $dx = 10\mu m$, $dy = dz = 0$. Although the displacement map is rather interesting, the maximum sensitivity to the x-component is only 0.5%. The maximum displacement shown is $0.05\mu m$ at the four corners of the object. This setup is very insensitive to the in-plane displacement in the x-direction. Of course, the same sensitivity factor can achieved for the x-component of the displacement by simply rotating the illuminating sources 90 degree around the z-axis. In Figure 4.14, the picture shows the result of a displacement of $dz = 10\mu m$, $dx = dy = 0$. The maximum displacement measured would be $0.5\mu m$. It is one order higher than the case in Figure 4.13. Figure 4.15 represents a combined case in which the displacement is $dx = dy = dz = 10\mu m$. Although the dy component contributes more than 99% to the total displacement, the relative displacement has been greatly altered.

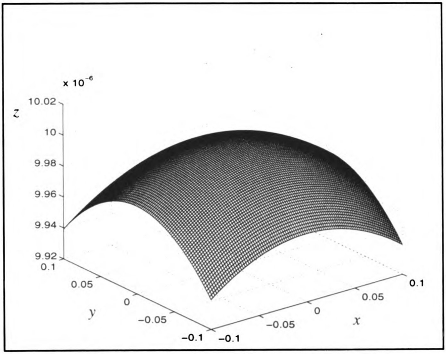

Fig. 4.12 Computer simulated measurement result for the in-plane ESPI setup using diverging double-beam illumination with the displacement field $dy = 10\mu m$, $dx = dz = 0$.

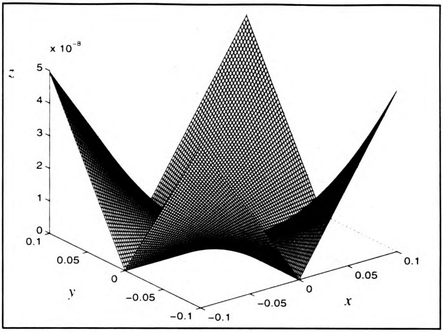

Fig. 4.13 Computer simulated measurement result for the in-plane ESPI setup using diverging double-beam illumination with the displacement field $dx = 10\mu m$ and $dx = dz = 0$.

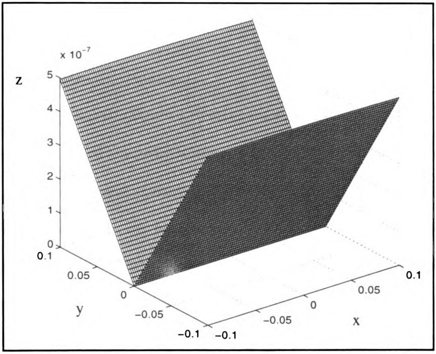

Fig. 4.14 Computer simulated measurement result for the in-plane ESPI setup using diverging double-beam illumination with the displacement field $dz = 10\mu m$ and $dy = dx = 0$.

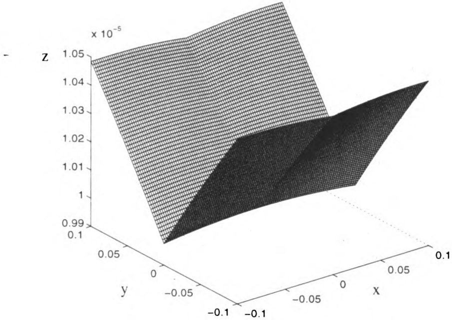

Fig. 4.15 Computer simulated measurement result for the in-plane ESPI setup using diverging double-beam illumination with the displacement field $dx = dy = dz = 10 \mu m$.

(3) Collimated beams (non-symmetrical)

The optical setup shown in Figure 4.16 may be used to measure the out-of-plane displacement with reduced sensitivity. Owing to the limited spatial resolution of the TV system, the displacement measurement range for a typical ESPI system is about 15 μm. In order to increase the range, two methods may be used. The first is the step-by-step reference method [Floureux 1993]. The potential of this technique is to study highly localized displacement fields as found in the field of fracture mechanics, and this method also offers better verification between finite element analysis and ESPI results [Flemming, Hertwig, and Usinger 1993; Hertwig, Flemming, and Usinger 1994]. The second technique is the optical desensitized method. Because θ_{iy1} and θ_{iy2} are not $\frac{\pi}{2}$, the in-plane displacement will also contribute to the phase changes. The reduction of the out-of-plane displacement sensitivity is related to the angle between the two illuminating beams. The smaller the angle, the less the sensitivity.

The sensitivity vector in this case is given by

$$\vec{K} = \frac{2\pi}{\lambda}[(\cos\theta_{iy1} - \cos\theta_{iy2})\hat{j} + (\cos\theta_{iz1} - \cos\theta_{iz2})\hat{k}] \tag{4.18}$$

Therefore, the phase change resulting from the displacement $\Delta\vec{d}$ is given by

$$\Delta\phi = \frac{2\pi}{\lambda}[(\cos\theta_{iy1} - \cos\theta_{iy2})d_y + (\cos\theta_{iz1} - \cos\theta_{iz2})d_z] \tag{4.19}$$

if d_y is small compared to d_z, we may write

$$\Delta\phi = \frac{2\pi}{\lambda}(\cos\theta_{iz1} - \cos\theta_{iz2})d_z \tag{4.20}$$

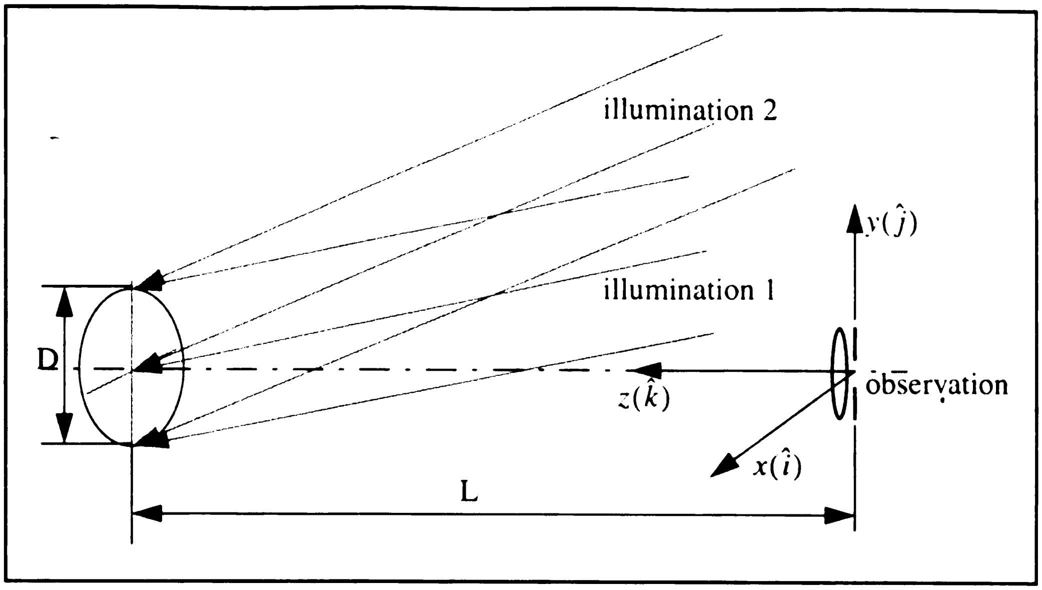

Fig. 4.16 Non-symmetrical collimated double-beam illumination.

4.1.3 Discussions

The displacement induced phase change is a function of the sensitivity vector and the displacement vector. An inappropriate approximation in the phase calculation can bring large errors to the measurement, especially for an unknown displacement field. To measure the deformation of an object, the out-of-plane deformation will cause in-plane deformation due to the Poisson's ratio of material, and vice versa. One should take these factors into account when making assumptions about the displacement field. The magnitude of the in-plane displacement may be checked by using a double-beam illumination arrangement. A sensitivity compensation table may be constructed for all the points on the object by keying several configuration parameters of the measurement setup into a computer program to offset the variable sensitivity vector introduced measurement errors.

4.2 Analysis for ES system

In ES, as illustrated in Figure 3.1, two separate neighboring points p_1 and p_2 are brought to a point and interfere with each other because of the shearing effect of the imaging system. Figure 4.17 shows a coordinate system which will be used in the sensitivity vector and measurement analysis for ES.

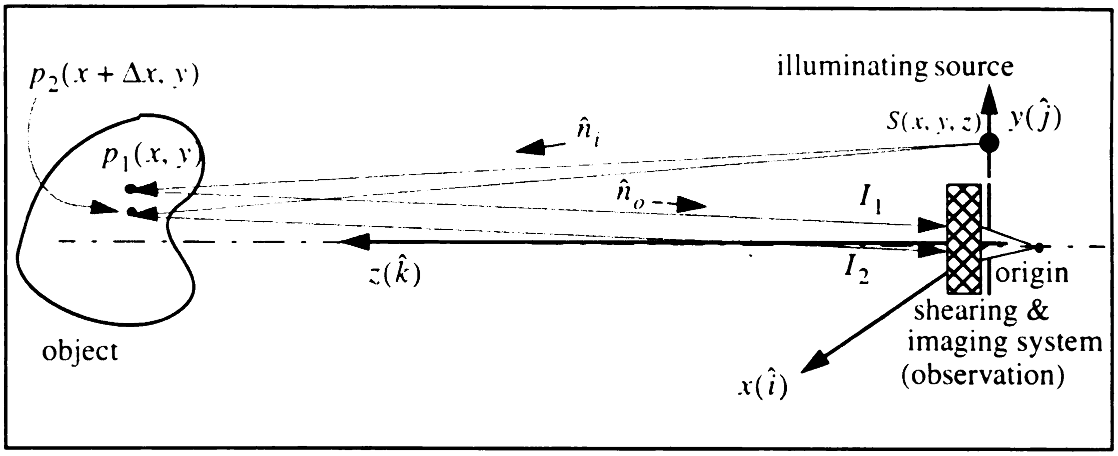

Fig. 4.17 Schematic for ES sensitivity vector analysis.

Similar to the one-beam ESPI case, the sensitivity vector $\vec{K}$ of a typical ES setup is given by

$$\vec{K} = \frac{2\pi}{\lambda}(\hat{n}_i - \hat{n}_o) \qquad (4.21)$$

where $\hat{n}_i$ is the illumination propagation unit vector, $\hat{n}_o$ is the observation propagation unit vector, and λ is the wavelength of the light.

Again, the propagation unit vectors can be calculated for each point on the object from the coordinates of the illuminating source, the point on the object, and the center of the entrance aperture of the imaging lens (the origin of the coordinate system in Figure 4.18). They are given by

$$\hat{n}_o = -\frac{x\hat{i} + y\hat{j} + z\hat{k}}{\sqrt{x^2 + y^2 + z^2}} = n_{ox}\hat{i} + n_{oy}\hat{j} + n_{oz}\hat{k} \tag{4.22}$$

$$\hat{n}_i = \frac{(x - x_i)\hat{i} + (y - y_i)\hat{j} + (z - z_i)\hat{k}}{\sqrt{(x - x_i)^2 + (y - y_i)^2 + (z - z_i)^2}} = n_{ix}\hat{i} + n_{iy}\hat{j} + n_{iz}\hat{k} \tag{4.23}$$

where n_{ix}, n_{iy} and n_{iz} are the x, y and z components (direction cosines) of the $\hat{n}_i$ propagation unit vector respectively. n_{ox}, n_{oy} and n_{oz} are the x, y and z components of the $\hat{n}_o$ propagation unit vector respectively. Equation 4.21 can be rewritten as

$$\vec{K} = \frac{2\pi}{\lambda}[(n_{ix} - n_{ox})\hat{i} + (n_{iy} - n_{oy})\hat{j} + (n_{iz} - n_{oz})\hat{k}] \quad . \tag{4.24}$$

When the object is deformed, the relative phase change between the two interfering points can be written as

$$\Delta\phi = \vec{K} \bullet (\Delta\vec{d}) \tag{4.25}$$

where $\Delta\vec{d}$ is the relative displacement between the two neighboring points. When the shearing is in the x-direction and the amount of shearing is Δx, using Taylor's expansion, $\Delta\vec{d}$ can expressed as

$$\Delta\vec{d} = \frac{\partial}{\partial x}(d_x\hat{i} + d_y\hat{j} + d_z\hat{k})(\Delta x) + \frac{1}{2}\frac{\partial^2}{\partial x^2}(d_x\hat{i} + d_y\hat{j} + d_z\hat{k})(\Delta x)^2 + \ldots + o(\Delta x)^n \tag{4.26}$$

where $o(\Delta x)^n$ represents the higher order small terms. For small shearing Δx, We have

$$\Delta\vec{d} \approx \frac{\partial}{\partial x}(d_x\hat{i} + d_y\hat{j} + d_z\hat{k})\Delta x \tag{4.27}$$

therefore, equation 4.24 becomes

$$\begin{aligned} \Delta\phi &= \vec{K} \bullet (\Delta\vec{d}) \\ &= \frac{2\pi}{\lambda}\left[(n_{ix} - n_{ox})\frac{\partial d_x}{\partial x} + (n_{iy} - n_{oy})\frac{\partial d_y}{\partial x} + (n_{iz} - n_{oz})\frac{\partial d_z}{\partial x}\right]\Delta x \end{aligned} \tag{4.28}$$

When the illumination and observation unit vectors are both parallel with the z-axis (the optical axis), equation 4.27 reduces to

$$\Delta\phi \approx \frac{4\pi}{\lambda}\left(\frac{\partial d_z}{\partial x}\right)\Delta x \tag{4.29}$$

or we can write

$$\frac{\partial d_z}{\partial x} \approx \frac{\Delta\phi\lambda}{4\pi(\Delta x)} \tag{4.30}$$

where $\frac{\partial d_z}{\partial x}$ is the derivative of the out-of-plane displacement with respect to x-direction, and this is normally the output from a direct ES measurement. For practical cases, strictly speaking, there are not any cases where the illumination and observation vectors are parallel with the optical axis for every point on the test object. Although this condition may be achieved approximately, sometimes it is wrongly assumed. A discussion will be given below to analyze the influence of the sensitivity vectors and the approximations.

If the shearing is very small (but it must be greater than the size of the speckle), we may have the following approximations:

$\hat{n}_{i1} \approx \hat{n}_{i2} = \hat{n}_i$

$\hat{n}_{o1} \approx \hat{n}_{o2} = \hat{n}_o$

where $\hat{n}_{i1}$ and $\hat{n}_{i2}$ are the illumination unit vectors of points p_1 and p_2, and $\hat{n}_{o1}$ and $\hat{n}_{o2}$ are the observation unit vectors for points p_1 and p_2 respectively. $\hat{n}_i$ and $\hat{n}_o$ act as the "weighted unit vectors" representing the two interfering points p_1 and p_2. When the distance between the test object and the imaging lens is much greater than the size of the area under test, the following approximation holds:

$n_{ox} \approx n_{oy} \approx 0$

$n_{oz} \approx -1$.

Further, if the source of the illumination is very close to the imaging lens in comparison with the distance between the test object and the illuminating source, the following approximations may be used

$n_{ix} \approx n_{iy} \approx 0$

$n_{iz} \approx 1$.

Under the above conditions, the final approximation, equation 4.29, may be reached. The fringes depict the derivative of the out-of-plane displacement with respect to the shearing direction.

Additional results can be obtained from ES by arranging the optical configuration in different ways. If the conditions for deriving equation 4.29 are satisfied except that the illuminating source is on the y-axis and is not close to the lens, with the shearing in the x-direction, we have

$n_{iy} \neq 0$, $n_{iz} \neq 0$, and $n_{ix} \approx 0$.

Equation 4.29, using the same definition for the signs of the vector components as described in Chapter Two, becomes

$$\begin{aligned}\Delta\phi &\approx \frac{2\pi}{\lambda}\left[(n_{iy})\frac{\partial d_y}{\partial x} + (1 + \cos\theta_{iz})\frac{\partial d_z}{\partial x}\right]\Delta x \\ &= \frac{2\pi}{\lambda}\left[(\sin\theta_{iz})\frac{\partial d_y}{\partial x} + (1 + \cos\theta_{iz})\frac{\partial d_z}{\partial x}\right]\Delta x\end{aligned} \tag{4.31}$$

if the shearing is changed to the y-direction, equation 4.31 changes to

$$\begin{aligned}\Delta\phi &\approx \frac{2\pi}{\lambda}\left[(n_{ix})\frac{\partial d_y}{\partial y} + (1 + \cos\theta_{iz})\frac{\partial d_z}{\partial y}\right]\Delta y \\ &= \frac{2\pi}{\lambda}\left[(\sin\theta_{iz})\frac{\partial d_y}{\partial y} + (1 + \cos\theta_{iz})\frac{\partial d_z}{\partial y}\right]\Delta y\end{aligned} \tag{4.32}$$

If the illuminating source is placed on the x-axis, with shearings in x-direction and y-direction respectively, we have

$$\begin{aligned}\Delta\phi &\approx \frac{2\pi}{\lambda}\left[(n_{ix})\frac{\partial d_x}{\partial x} + (1 + \cos\theta_{iz})\frac{\partial d_z}{\partial x}\right]\Delta x \\ &= \frac{2\pi}{\lambda}\left[(\sin\theta_{iz})\frac{\partial d_x}{\partial x} + (1 + \cos\theta_{iz})\frac{\partial d_z}{\partial x}\right]\Delta x\end{aligned} \tag{4.33}$$

and

$$\begin{aligned}\Delta\phi &\approx \frac{2\pi}{\lambda}\left[(n_{ix})\frac{\partial d_x}{\partial y} + (1 + \cos\theta_{iz})\frac{\partial d_z}{\partial y}\right]\Delta y \\ &= \frac{2\pi}{\lambda}\left[(\sin\theta_{iz})\frac{\partial d_x}{\partial y} + (1 + \cos\theta_{iz})\frac{\partial d_z}{\partial y}\right]\Delta y\end{aligned} \tag{4.34}$$

Note that the two in-plane derivatives of the displacements can be separated in equations 4.31 through 4.34 if we record two interferograms with different illumination angles.

Therefore, after solving equations 4.31 through 4.34, a complete 2D state of strain can be measured. We have

$$\varepsilon_x \approx \frac{\partial d_x}{\partial x} \tag{4.35}$$

$$\varepsilon_y \approx \frac{\partial d_y}{\partial y} \tag{4.36}$$

$$\gamma_{xy} \approx \frac{\partial d_x}{\partial y} + \frac{\partial d_y}{\partial x}. \tag{4.37}$$

Note if the out-of-plane displacement d_z is a constant, the derivative of it will be zero. Moreover, if d_z is a function of y only, using x-shearing will cause the derivative of d_z to be zero, and if d_z is a function of x only, using y shearing will cause the derivative of d_z to be zero. One may use these relations to simplify the interpretation of the measurements. Also note that when the illumination angle θ_{iz} increases, the light intensity scattered into the imaging lens will generally decrease.

At present, because of the limited resolution of CCD cameras and poor quality of the shearographic fringes, very accurate slope and strain measurements have not been achieved [Owner-Petersen 1991a].

CHAPTER V

APPLICATIONS OF ESPI AND ES TO NDE

Non-destructive evaluation is, to date and perhaps for the future, the most important area of the applications of ESPI and ES. Fast and highly sensitive testing can be achieved by using ESPI or ES systems.

5.1 NDE of fiber reinforced plastic composites

Because of their high strength-to-weight ratios and designable properties, fiber reinforced plastics (FRP) composite materials are becoming increasingly important for high volume industrial applications. Since a composite is a combination of two or more materials, the likelihood of defects in composite components is generally higher than in metals. Consequently, there is an urgent need for nondestructive inspection of composite structures during and after fabrication. Since defects and damage can develop during service, nondestructive inspections may be required during the lifetime of a critical product such as high pressure natural gas vessels for vehicles and aircraft. A universally practical method that can effectively and economically detect and characterize defects in composite materials in a production/field environment or a service/maintenance station has yet to be developed.

FRP composites are very different materials from metals when considering which

NDT methods are appropriate. In general, FRP materials have poor electrical and thermal conductivity, high acoustic attenuation and high anisotropy of mechanical and physical properties. Therefore, many traditional NDE tools can not be effectively utilized.

Some NDE methods for composite materials were discussed by Jones & Berger [1989], Summerscales [1990], and Chapman and Hagerman [1993] among others. At the present time, the NDE methods most widely used in industry for composite inspection are ultrasonics and x-radiography. Ultrasonic techniques detect the flaws by measuring the response of the ultrasonic signal traveling in the materials. Because of the point by point scanning procedure of the technique, the ultrasonic method is normally slow. Some type of media (water, gels...) is required to couple ultrasound energy from the transducer into the materials. X-radiography relies on the differential absorption or scattering of the x-ray photons as they pass through a material. Flaws that either allow more x-ray photons to pass or that absorb or scatter the photons can be imaged if the effect is significant. The molecules in FRP composites are usually of low atomic weight, and hence the absorption of x-rays is low, so contrast is usually poor, especially for thin plates. Neither of the methods relate the detection to the stress/strain states of the test object. Therefore, how the detected flaw affects the performance of the component can not be revealed by the experiment.

Unlike other NDE techniques, loading (stressing) is an essential part of NDE processes using interferometry, including ES and ESPI. The loading provides a very important connection between the detected flaws and the effect of the flaws on the integrity and strength of the structures. NDE techniques such as ultrasound, x-ray, magnetic particle, eddy current, etc., provide little or no information on whether or not these flaws will weaken the structures.

5.2 Loading (stressing) techniques

The key to successful NDE using HI, ESPI or ES is the selection of an effective stressing techniques that will cause flaws to effect a localized surface deformation. Loading techniques are as important as the ESPI and ES systems themselves when they are used for NDE applications. That is, we have

Stressing techniques + ESPI (or ES, HI) → NDE

The object under test can be mildly stressed in several ways, which include mechanical stressing, thermal excitation, pressurization/vacuum, and acoustic or mechanical vibration. The method employed would depend upon the object itself, the type of defect to be detected, and the accessibility of the object. For each loading method, there are a number of ways to carry it out.

Thermal loading -- A number of methods can be used. (1) refrigerator and oven, (2) heating elements (strip, foil, resistor...), (3) hair dryer, (4) steam jet, (5) electric bulb, (6) radiation from quartz heaters or infrared lamps, and (7) even the relative warm human hands. Thermal loading is especially suitable for materials with low heat conductivity. The repeatability of the thermal loading should be considered in some cases. Where the thermal loading technique can be used, it offers an advantage in minimal disturbance of the rig for mounting the test object. In real-time mode, thermal loading is usually most satisfactory, since the dynamically changing fringe patterns can normally be observed. Debondings in honeycomb or laminate structures result in large local deformation when bending stresses are induced by temperature gradients. Air spaces created by debonds conduct less heat than do regions where a good bond exists, as a consequence, the temperature field is distorted. Similarly, thermal distortions can be caused by crushed honeycomb cores, voids, delaminations, or other nonhomogeneities in composite materials. A small temperature gradient of a few degrees is often sufficient to produce surface displacements amounting to many fringes.

Mechanical loading -- refers to loading the test objects in tension, compression, bending, torsion, or point load. When mechanical loading is used, care must be taken to eliminate any rigid body motion. Tests involving high mechanical loads should be avoided if possible because of the complexity of the loading rig necessary to hold the test object stationary. Miniature hydraulic jacks seem suitable for producing some mechanical loadings. An unusual mechanical stressing using gravity-induced creep for fiber reinforced plastic composites has been demonstrated by Chen and Cloud [1994] and this technique will be discussed in detail in Chapter 5.

Pressure or vacuum -- Pressure or vacuum loading is often suitable for inspecting debonding and delaminations in composite materials and structures. For container-type components such as pressure vessel and pipes, this type of loading is easy to apply, otherwise, a vacuum chamber may be used. An additive-subtractive phase-modulation ESPI technique that is synchronized with pressure stressing is proposed as a way to minimize the susceptibility of ESPI NDE to environmental noise [Chatters, Pouet, and Krishnaswamy 1992, 1993]. Vacuum stressing and artificial delamination (airbag) was used to demonstrate the effectiveness of vacuum stressing to delaminations of composite material [Wang et al. 1993]. Pressurization has been used in our lab to detect impact damage in carbon/glass fiber wrapped composite vessels (cylindrical and spherical natural gas tanks) [e.g. Nokes et al 1995; Cloud et al. 1995].

Vibrational excitation -- This method is useful for detecting debondings in composite materials and for disclosing inhomogeneities in materials or structures. When a structure vibrates in its resonant mode, it creates bending stresses which may cause anomalous deformation near flaws such as voids. Debondings near the surface, for example, between the skin and the core of a honeycomb panel, may create a local resonance. Frequency of the excitation is varied to locate such local resonance. Normally, quite high frequencies are needed to excite the local resonance. In general, unbonded areas in structures respond to a wider bandwidth of frequencies than does the structure itself. A technique which uses white noise vibration excitation was reported, the dark areas in the time-average fringe pattern indicate the flaws [Claraday 1983].

Acoustic stressing -- Acoustic stressing may be achieved by the use of piezoelectric transducers bonded on the surface of the test object., or by the use of loudspeakers. Ultrasonic transducers can be used to produce surface waves for NDE application [Crostack, Meyer, and Pohl 1991].

Elastic waves -- Elastic waves may be produced by impact or by a pulsed laser-induced localized thermal expansion. A pendulum may be used to produce elastic wave propagation in the materials as a loading technique [Fällström 1991a]. In this case, pulsed lasers have to be used to capture the fringe patterns.

Microwave or moisture -- Microwave radiation and moisture may also be used for stressing objects. The idea is that microwaves can heat up the object from inside.

While all the loading methods described above may be used for NDE of FRP composites, thermal loading and pressurization/vacuum methods were found by experiment to be the most effective. Thermal methods normally work very well with fiber reinforced plastic materials due to their low heat conductivities. Table 5.1 is a list of

thermal properties of some materials.

Table 5.1 Thermal properties of some materials

Materials -	Thermal Conductivity W/m-^oK	Coeff. of Linear Expansion x 10^{-6} / ^oK
Plain Carbon Steel	100	3.72
Polyester Resins	0.17 - 0.22	17.22 - 30.56
Epoxy Resins	0.17 - 0.20	13.89 - 20.0
E and S Glass	1.05	1.56
Graphite / Carbon	$(80)_{L,}$ $(12.5)_T$	0.28

As we can see from Table 5.1, fibers have significantly smaller coefficients of thermal expansion (CTE), the CTE of glass fiber is 1.56 x 10^{-6} / ^oK, while a typical epoxy value is 17.22 x 10^{-6} / ^oK. Carbon and graphite fibers are anisotropic in thermal expansion. The CTE's are usually extremely small, either positive or negative, on the order of 0.28 x 10^{-6} / ^oK. It follows that a unidirectional fiber composite has very small CTE in the fiber direction because the fibers will restrain matrix expansion. On the other hand, the transverse CTE will be much larger because the fibers move with the expanding matrix and thus provide less restraint to matrix expansion.

These phenomena are of considerable practical importance, particularly for laminates made of unidirectionally reinforced layers. When such a laminate is heated, the expansion of any layer is prevented by the adjacent laminae because the fiber directions in all layers are different. This causes internal stresses that could be considerable, even when the laminate is allowed to expand freely.

All polymeric matrix viscoelastic properties, such as creep and relaxation, are significantly dependent on temperature. This dependence will also introduce deformations when there is a temperature change. No matter how complicated the stress field is, looking at the large scale, the stress-introduced displacement field should be uniform if the composite plate is without defects.

Thermal stressing has been used for various applications of holographic nondestructive testing. This technique is used to observe mechanical deformation which occurs in response to changes in temperature. The object can be heated by a heating device such as a hair drier, an electric bulb, a soldering iron, steamed air (vapor) or even an electric resistor. It also can be cooled by using a refrigerator or by evaporation after a volatile substance like alcohol has been sprayed on it. Air spaces created by debonds conduct less heat than do regions where a good bond exists, so the temperature field itself is distorted. Similar thermal distortion can be caused by crushed honeycomb cores, voids, delaminations, or by other nonhomogeneities in composite materials. Thermal loading has been used to identify defective solder joints on printed circuit boards [Lu et al. 1990] and to detect debonded areas of adhesive joints between FRP composite and steel frame [Cloud, Nokes, and Chen 1993].

In our experimental study, we found that using steamed air (vapor) to introduce a temperature difference into materials, especially a composite material, is very effective. The steamed air can be directed to a localized area, or spread to a large area to create a small temperature difference (ΔT about $10^{o}C$) between the specimen and the ambient. Then, allowing the specimen to expand under some constraint was found to be very effective and easy to do. Similarly, an electric lamp can also be used to apply thermal stressing. To create a localized heating spot, the lamp radiation may be transferred through a fiber optic bundle. This problem may be solved by coupling a fiber optic bundle to the light source.

For an undamaged composite plate, when the heat source is removed, the created fringe pattern will tend to trace back into the original (or primary) heat point or the area which generates those fringes (where the heat is applied), and the speed of the 'trace back' is very fast (several seconds). If there is damage, the damaged zone will block this 'trace back' and act as another heat source creating some 'secondary' fringes, and these 'secondary' fringes will rest there for quite some time, long enough for observation or recording. These phenomena were checked on different specimens using different heating locations. This happens because in the damaged zone the matrix is loosened, some fibers may be broken, and likely there will be some air trapped in the matrix and between laminates. Overall, these will decrease the thermal conductivity in the damaged zone area. When we monitor the live change of this phenomena it is quite obvious. To characterize the size of the damage and the depth of the damage more work must be done. The steamer we used is very simple. A more sophisticated device can be built to have adjustable heat flow and temperature.

5.3 Complementary use of ESPI/ES with ultrasonic c-scan

A method utilizing the advantages of ESPI/ES and ultrasonic C-scan for nondestructive evaluation of materials is described. Some experimental results using this method on fiber reinforced plastics are presented. This approach seems to be very effective and efficient, and it should be equally applicable to other materials.

Flaws and damage in the material can affect the displacement/strain field when the material is under stress. The existence of flaws and damage are indicated in the interferometric fringe pattern as fringe anomalies through the use of a proper loading technique. The flaws and damage which affect the structure the most may be detected by employing the loading type which simulates the working condition of the product. Unfortunately, the depth and the size of the defect are difficult to determined accurately by the interferometric techniques, while the ultrasonic technique can measure the depth and size of the flaw.

From the above analysis, the complementary use of ESPI/ES and ultrasonic techniques seems to be able to offer a better approach for effective and quantitative NDE of composite materials because their results are complementary to each other. Figure 5.1 is an illustration of this approach. To carry it out, a two-step process could be used. Step one, use ESPI/ES with appropriate loading techniques to find areas with defects. Step two, ultrasonic techniques or other NDE techniques can then be used to zoom into the localized areas to establish the depth, the size, and other characteristics of the flaws. This procedure would be more efficient and effective than using only one of these techniques.

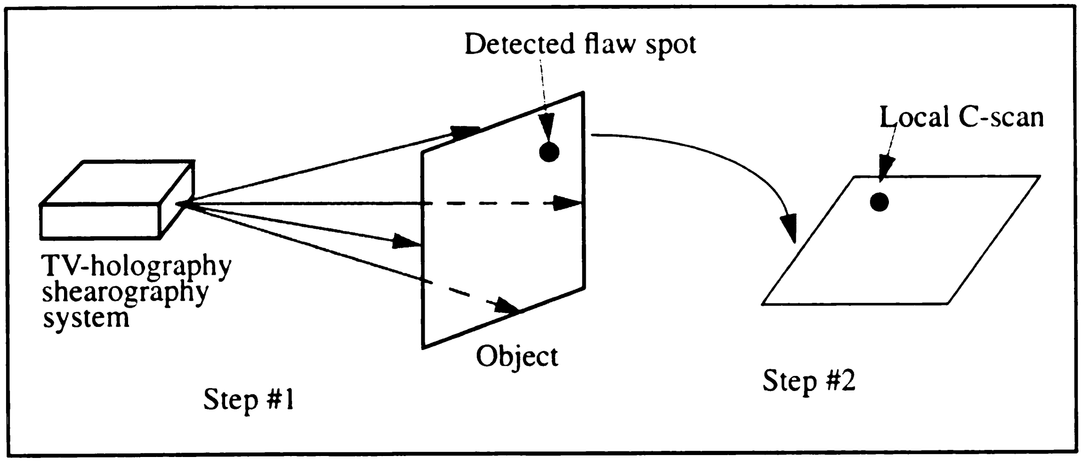

Fig. 5.1 Illustration of the complementary NDE approach.

As mentioned previously, loading techniques play a key role in NDE applications.

Flaw and damage detection by ESPI/ES is based on the comparison of the two states of deformation in the object. Development of NDE procedures employing ESPI/ES essentially becomes the development of a practical means of stressing the object so that flaws and damage are revealed. Thermal, pressure, vacuum, vibrational excitation, and mechanical loading are commonly used for stressing the object. Some unusual loading techniques can also be used [Chen and Cloud, 1994]. Note that each loading type, such as thermal, can be carried out by different procedures. Different loading methods can result in different effects. The effectiveness of the loading methods depends on the nature of the damage or flaw, and it also depends on the types of materials. Once the equipment is in place, the effective detection of the damage and flaws is largely dependent on the loading methods.

The flaws and damage are normally shown in the fringe pattern as anomalies such as "bulls-eye", "butterfly", fringe discontinuities, abrupt fringe curvature or density changes depending on the types of the flaws. The loading techniques should be designed to reveal flaws and damage as distinctly as possible; and the ideal loading normally will be the one which simulates the actual working condition of the component.

5.3.1 Ultrasonic techniques

The basic ultrasonic testing technique is to transmit a pulse of high-frequency (typically 500KHz to 10MHz) energy through the specimen and to measure the transit time or attenuation of the signal [Krautkrämer 1977; Bar-Cohen 1987]. The attenuation is a function of the state-of-cure of the matrix resin, and the condition of the fiber-resin interface, delaminations, porosity, inclusions, and cuts. The measurement may be either through-transmission or pulse-echo. Ultrasonic through-transmission test systems measure the signal strength of a pulse of ultrasonic energy transmitted through the material under test. This approach is probably the most commonly used production inspection method for composite materials. The method is sensitive to most flaws that are planar in nature and lie roughly parallel to the surface. The method generally requires access to both sides of the part and alignment of transducers on opposite sides of the part. These factors restrict the usefulness of this approach for in-service inspection because, in many cases, access to both sides of the structure is not available or not practical. For the pulse-echo method, the inspection requires access to only one side of a composite structure. Flaws are detected by monitoring the time of arrival and/or the signal strength of returning echoes. Flaws cause the returning echo to arrive before its expected travel time from the back surface. This method is commonly used for in-situ inspection because the single-transducer approach usually makes it simpler to apply in a manual test. On the other hand, the more complex signal patterns and more critical incidence angle make this test more difficult to automate than the through-transmission test. An advantage of the pulse-echo technique is that flaws at multiple depths can be distinguished from one another. In this study, a computer controlled pulse-echo C-scan ultrasonic system was used. A schematic of the system is shown in Figure 5.2. Ultrasonic techniques can not show the effect of the flaws on the stress state of the object.

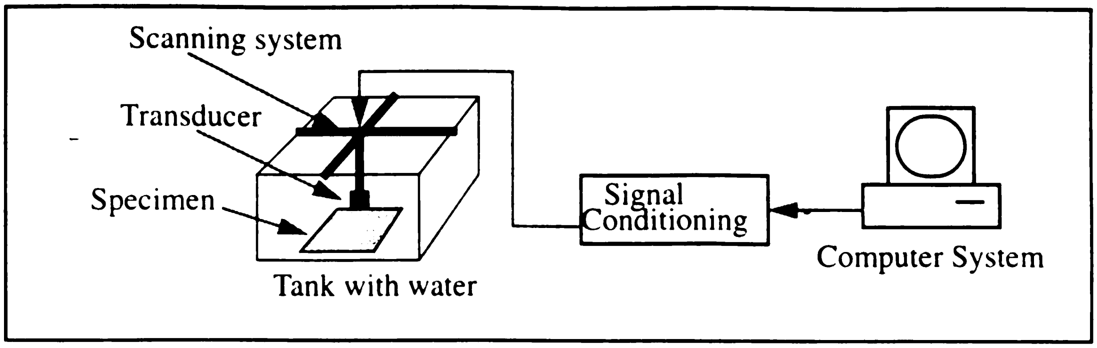

Fig. 5.2 Schematic of ultrasonic C-scan system.

5.3.2 Experiments combining interferometry and ultrasound

The purpose of this program is to demonstrate the idea of the complementary use of ESPI/ES and ultrasonic techniques. The flaws are detected by ESPI/ES technique through thermal-loading-induced deformation, and by ultrasonic c-scan method.

The specimen used in this study was a glass fiber reinforced plastic plate (random chopped glass strands/polyester). The area of the specimen is 150 *mm* x 150*mm* and the thickness is 3*mm*. Two voids having different shapes and sizes were made in the specimen to simulate flaws. The detailed configurations of the flaws are shown in Figure 5.3. The specimen was clamped around the edges which results in a circular examination area of about 120 *mm* in diameter. The experiment setup is shown in Figure 5.4.

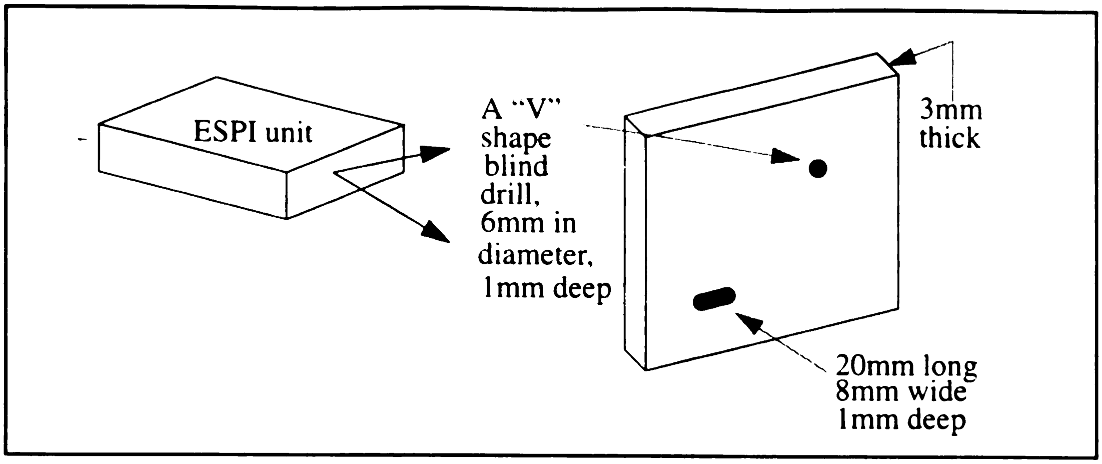

Fig. 5.3 Configuration of the specimen.

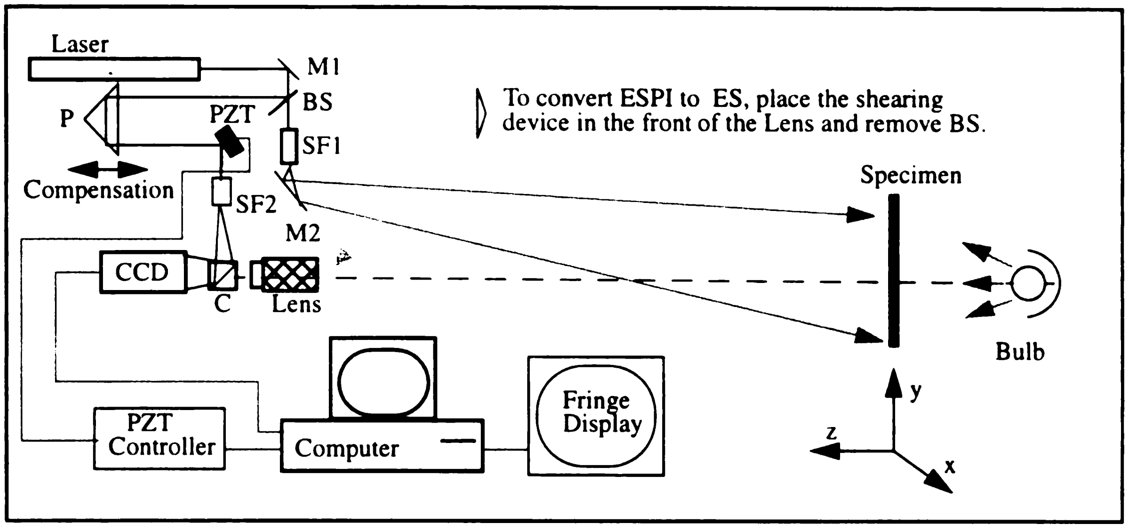

To convert ESPI to ES, place the shearing device in the front of the Lens and remove BS.

Fig. 5.4 Schematic of ESPI/ES systems and the experimental setup.

In this experiment, thermal loading was used to stress the specimen. Thermal stressing has been used for various applications of holographic nondestructive testing. This technique is used to observe the deformation which occurs in response to changes in temperature. As mentioned, the object can be heated by a heating device such as a hair drier, an electric bulb, a soldering iron, or even an electric resistor. Air spaces created by delaminations, voids or cuts conduct less heat than do regions where a good bond exists, so the temperature field itself is distorted causing anomalies in the fringe pattern with anomalies. Thermal distortion also can be caused by other nonhomogeneities in composite materials. Thermal loading techniques have been found very effective in working with FRP composite materials because of the low heat conductivity and the mismatch of the conductivities between fiber and matrix.

A regular 40W bulb was used to apply the thermal loading for simplicity. The temperature field of the specimen is a function of the time length of heating, the power of the bulb, the distance between the bulb and the specimen, and the boundary conditions of the specimen. Since the specimen was heated from one side, there is a temperature gradient between the front and the rear surfaces. This temperature difference may create a bending effect in addition to thermal expansion. Care should be taken in using such thermal loading techniques. A small permanent deformation (a couple of microns) was observed after a specimen was heated for about 20 seconds when the bulb was placed two inches away from the specimen surface. A distance of 8 inches between the specimen and the bulb, therefore, was used in this test to avoid the possible permanent deformation.

The flaw detection procedure by ESPI and ES is the following; (1) the bulb is first turned on for about 10 seconds, then switched off. A reference picture of the specimen speckle pattern was taken after the lamp has been turned off; (2) development of the fringe pattern is watched closely (the real-time subtraction speckle pattern); (3) the fringe pattern which clearly indicates the flaws is captured. This heat-up and then turn-off of the heat before acquiring the pictures is best suited for this type of loading method in that it does not introduce any loading-related disturbance to the image acquisition process. Figure 5.5 shows three digitally filtered ESPI interferograms that reveal the two flaws as anomalies in the fringe patterns. Picture 5.5a is the fringe pattern taken immediately after the bulb was switched off. Figure 5.5b indicates the flaws at about 3 seconds after the bulb was switched off. Figure 5.5c displays the flaws at about 5 seconds after the bulb was turned off. The two flaws are indicated clearly as local bull-eye fringe anomalies in the fringe patterns in pictures 5.5a and 5.5b. In picture 5.5b the fringes in the area where there are no flaws disappeared, only a few fringes surrounding the two flaws were left. In picture 5.5c the indication of the small flaw disappeared and some fringes surrounding the big flaw shrank into the center of the flaw. The fringes in this case are the contours of the out-of-plane displacement. These ESPI fringe patterns were digitally filtered phase fringe patterns.

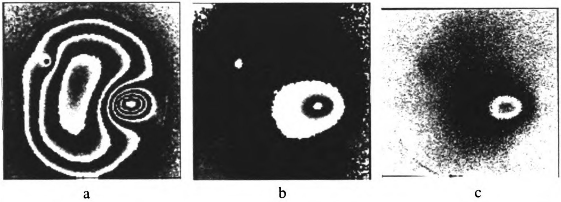

Fig. 5.5 ESPI fringe patterns (digitally filtered) showing the flaws at different time points

Figure 5.6 shows three fringe patterns obtained using ES in a time sequence. Again the same thermal loading technique was used. Figure 5.6a is the fringe pattern taken immediately after the bulb was switched off. In Figure 5.6a, the big flaw is clearly revealed as a butterfly pattern. The center of the flaw is the center of butterfly pattern. The small flaw is hardly seen. Figure 5.6b is the fringe pattern taken at about 3 seconds after the bulb was switched off. Picture 5.6c is the fringe pattern taken at approximately 5 seconds after the bulb was turned off. We can see that the recovery in areas where a flaw exists is slower than in the area without flaws. The fringe patterns in this case were not digitally filtered, and the fringes are the derivatives of the out-of-plane displacement with respect to the vertical direction.

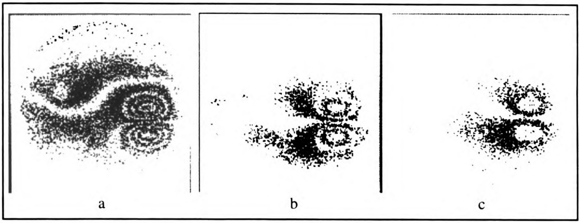

Fig. 5.6 ES fringe patterns (not digitally filtered) revealing the flaws at different time points.

In comparison with the ES results, we see that ESPI provides clearer flaw indication than does ES. After the bulb was turned off, the fringe pattern changes with the heat dissipation of the specimen. For our ES setup, the lateral shearing is rather large. If smaller shearing were used, the flaw indication would be more localized but sensitivity is then smaller.

The results from ultrasonic C-scan are shown in Figure 5.7. A 2.25 MHz transducer was used. A wave form correlation algorithm was implemented for the flaw detection. From the results obtained in ESPI and ES inspections, only the small areas centered in the flaw spots were scanned. Figure 5.7a is the C-scan picture of the plan view of the bottom of the big flaw, and Figure 5.7b is the plan view of the small flaw on the back surface of the plate (the reference signal was taken from the surrounding back surface). The shapes of the flaws were clearly displayed for both of the voids. A number of C-scans are needed if one wants to obtain the 3-D profile of the flaws. Knowing the thickness of the plate or the material properties, the depth of the flaw can easily be measured.

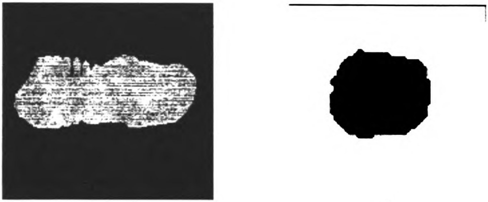

a b

Fig. 5.7 A plan view of the flaws detected using c-scan.

5.3.3 Conclusions on the complementary NDE method

Clearly, the complementary approach of using optical interferometric techniques, TV-holography/shearography, with ultrasonic C-scan offers an effective and efficient way to detect flaws and damage in fiber reinforced plastics. The method brings the advantages of TV-holography/shearography and ultrasonic C-scan together. It should be equally applicable to other materials, and equally workable with other NDE methods such as x-radiography. Various loading techniques can be selected depending on the specific problems. Thermal loading for FRP materials seems to be very simple and effective. A very small amount of thermal energy is normally sufficient to reveal flaws. In general, ESPI provides better indication of the flaws than does ES. But, ES may be more practical to use in an industrial environment because it is a common-path optical configuration.

5.4 NDE of FRP composites by gravity loading ("the loadingless method")

Gravity-induced creep under room temperature was studied and used as a loading technique with Electronic Speckle Pattern Interferometry (ESPI) for nondestructive screening of polymer composites. Some experimental results from use of this method on low-velocity impact damaged and undamaged glass/epoxy composite laminate plates showed that this method could be valuable as a first screening procedure in NDE of composites due to its simplicity and effectiveness. Positioning of the composite plate and the delay time before taking the first reference pattern seems to play an important role in the detection of the damage zone.

Nondestructive Evaluation (NDE) is very important for quality assurance and safety of products. There exists an urgent need for NDE of composite materials, as their usage continuous to increase dramatically [Chapman and Hagerman 1993]. A simple NDE screening procedure that could facilitate inspections at production line speeds would be especially valuable.

Several loading techniques such as mechanical loading, thermal stressing, pressure or vacuum, and vibration excitation can be used with ESPI. For each of the above techniques, some kind of loading device is involved. Sometimes, appropriate stressing of the test object is not very convenient or easy to do. Certainly, one can use the many loading techniques developed for traditional holographic interferometry over the years. However, in order to fully exploit the capabilities of ESPI and to incorporate the unique characteristics of new materials such as composites, efforts should be made to search for new effective stressing (loading) techniques.

The motivation of this study came from experience in using ESPI for NDE of composite materials. It was necessary to wait for a while to let the specimen settle down before taking the first reference pattern. Otherwise, the fringes resulting from gravity induced creep deformation would contaminate the results. At first, these fringes were considered to be a nuisance. Soon, we realized that this phenomenon may be utilized as useful information. This finding triggered a feasibility study on using gravity-induced creep for NDE of fiber reinforced polymer composites. Because of its simplicity, no loading devices would be required, ESPI with gravity loading could be used as a first step in NDE of composite materials. If more detailed inspection is required, ESPI or other NDE tools can then be used with various loading techniques to zoom into the areas which have been found by the gravity method to contain damaged spots or imperfections. This approach might save time and effort even if not all types of defects can be screened out by the gravity loading technique.

Most fiber reinforced composite materials use a polymer as the matrix material. All polymers exhibit time-dependent mechanical response, especially at higher temperature. However, the significance of the unique creep behavior of fiber reinforced composite at room temperature under only gravity has not been noticed. This study aims to use this characteristic to develop a good technique for NDE screening of composite materials using ESPI. Study of some glass/epoxy composite plates shows that at room temperature, impact-damaged and undamaged specimens will give significant difference in terms of the number of fringes and the shape of the fringes accumulated in a short time period under gravity alone. This time period is typically less than 30 minutes. The experiments described below showed that gravity force can be utilized at least to identify some damaged spots in composite materials with a polymer matrix.

5.4.1 Experiments with NDI using creep loading

In this study, a commercial ESPI system manufactured by Ealing Electro-Optics Inc. was used. To increase the laser power, a 25 mW external He-Ne laser was coupled into the system. A schematic of this system is shown in Figure 4.18a.

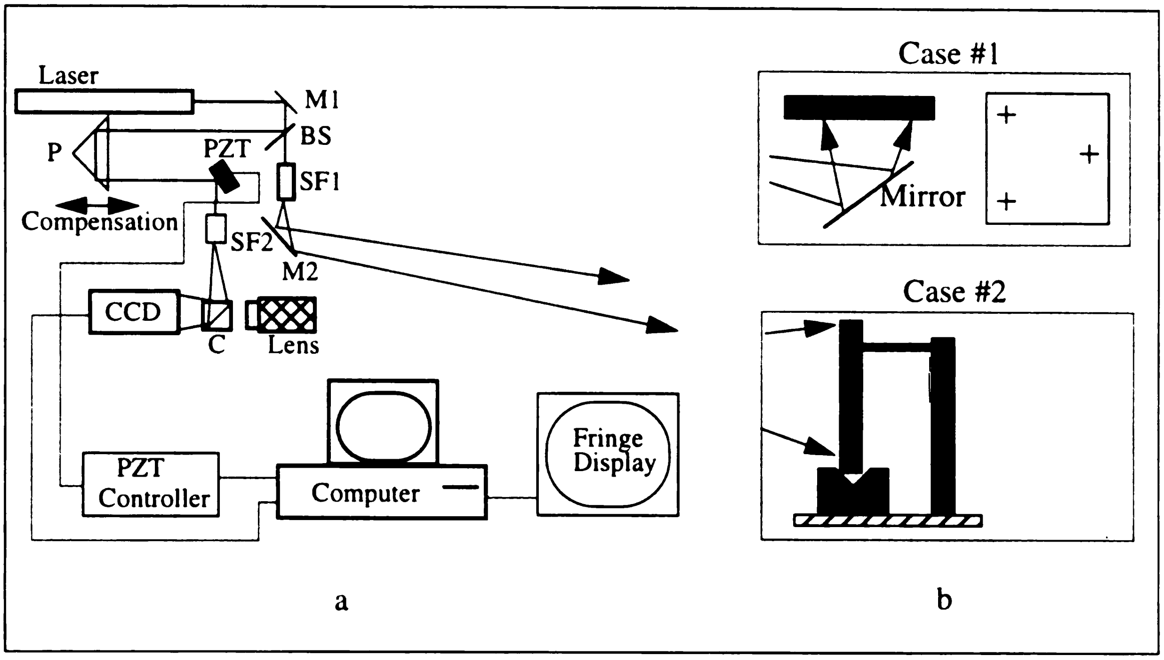

Fig. 5.8 The experimental setup, 5.8a the schematic diagram of the ESPI system; 5.8b the specimen setups.

Since a spherical illuminating beam is normally used, the angle of illumination varies across the entire object surface. This arrangement affects the accuracy of the quantitative displacement information calculated using phase stepping techniques. However, the problem should not be a concern for NDE applications due to the fact that one is mainly interested in finding fringe anomalies and not in determining precise displacement values.

The study was carried out on150 mm x150 mm continuous fiber glass/epoxy composite plates with various stacking sequences. Four plate specimens were studied. The configurations of the specimens are shown in Fig. 5.9. Among them, only specimen P1 was not damaged. The damage in the plates was caused by low-velocity (non-penetrating) impact. The point of impact is located in the central area of the plates. The size of the damage spot is about 10 mm x 10 mm. In general, the damage zone consists of delamination, fiber-matrix debonding, fiber breakage, and matrix cracking. The lay-ups of the composite plates strongly affect the shape and characteristics of the damage.

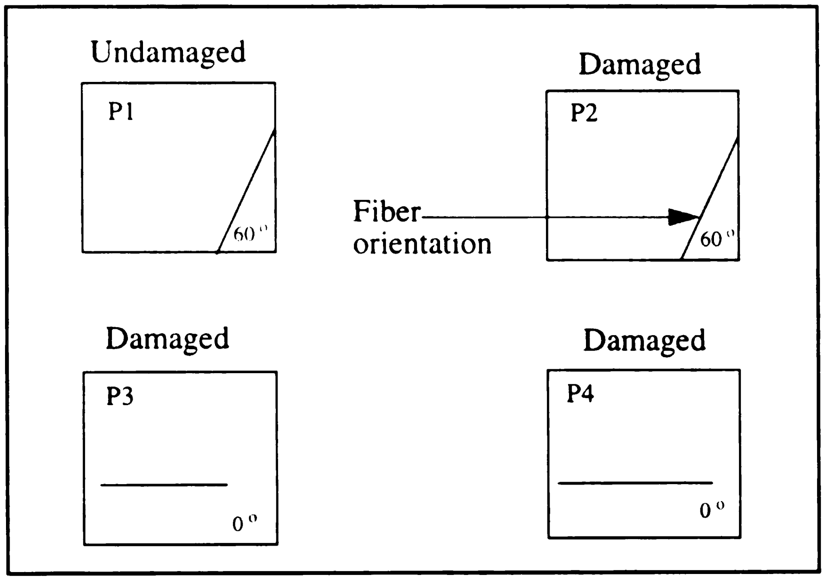

Fig. 5.9 The configuration of specimen plates (the line shows the orientation of fibers)

To assist in the planning of the setups for the specimens, an understanding of some fundamental properties of composite materials is necessary. The elastic properties of a unidirectional fiber composite (UDC) are functions of the elastic properties of fibers and matrix, of their relative volumes in the composite material, and of fiber directions.

Clearly, the stiffness in the fiber direction is much higher than the stiffness transverse to the fibers. If a load is applied in the fiber direction, it is carried primarily by the fibers, which deform very little and constrain the matrix to small deformation. On the other hand, in the direction normal to the fibers, the matrix is a continuous load carrying media and the fibers move with the deforming matrix, not significantly impeding deformation.

The viscoelastic effect in a UDC is more significant for axial shear, transverse shear, and transverse uniaxial stress. Creep compliance and relaxation moduli are a function of stress level and temperature. In this study, the load, which is merely gravity force, is distributed in the composite plate proportionally to mass. In practice, composite materials are laminated using many layers of UDC in multi-directions. This complicates the stress and strain analysis.

A variety of setups can be arranged to achieve specific stress situations in the object, including tension, compression, bending, torsion, and more complex stress conditions. In this feasibility study, only two positioning configurations of the sample plates were studied. One was horizontal positioning and another was vertical positioning. A schematic showing these setups is illustrated in Figure 5.8b as mentioned above.

Experiments showed that the primary creep during the first couple of seconds is the overall creep of the composite plate. The speed of this overall creep and the form of the creep are closely related to the stacking sequence and the number of plies of the plate. The overall creep was found to be faster and larger than the subsequent localized creep. The strong overall creep takes place immediately after the plate is placed into position. To avoid the domination of the overall body creep, a delay time (a couple of seconds) was used after the specimen was placed and before taking the first reference speckle pattern. Various creep times were used for different specimens, the creep time is the time elapsed between the first reference pattern and the second pattern.

In case #1, horizontal positioning, specimen plates P1, P2, P3 and P4 were tested. In this position, the plates were supported at three points around the edges to achieve stability and consistency. At the horizontal position, the direction of gravity is normal to the plane of the plate, and the major component of the displacement of the plate is out-of-plane displacement. The delay time and the creep time used for each specimen tested in this case are listed in Table 5.2 below.

Table 5.2 Delay and Creep Time in Case #1

Specimen #	P1	P2	P3	P4
Delay time in (sec)	5 ~ 10	5 ~ 10	~ 60	~ 60
Creep time in (min)	~ 10	~ 10	~ 30	~ 30

In case #2, vertical positioning, specimen plates P1 and P2 were inspected. A steel base with a V-groove was used as the support of the plate. The plate was placed on the groove in a free standing fashion with only a slight inclination against a pointer which was used to prevent falling of the specimen. By using the "V" type support, two edges of the plate were supported, which brings more stability to the specimen. Some shear stresses may also be introduced near the supported end of the plate. At the vertical position, the direction of gravity is in the plane of the plate. The major component of the displacement of the plates is expected to be in-plane displacement. Only about 10% of the in-plane displacement can be registered on the out-of-plane sensitive ESPI. The delay time and the creep time for each specimen are listed in Table 5.3 below.

Table 5.3 Delay and Creep Time in Case #2

Specimens	P1 (90^o)	P2 (90^o)
Delay time in (sec)	~8	~8
Creep time in (min)	~2	~2

5.4.2 Experimental Results

The experimental results are shown in Figures 5.10 through 5.14. In Fig. 5.10, the fringe patterns from plates P1 and P2 are compared. Horizontal positioning was used in this case. These two specimens are identical except P2 was damaged. 5.10a is the fringe pattern of the undamaged specimen P1, and 5.10b is the fringe pattern of the damaged specimen P2. In general, the area in a fringe pattern where a sharp or abrupt change of fringe curvature occurs indicate the location of flaws or damage. Obviously, there is an abrupt curvature change around the central region in the fringe pattern of the damaged specimen P2.

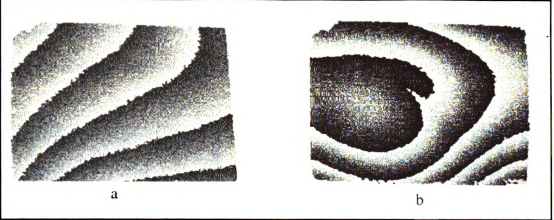

Fig. 5.10 Fringe patterns of P1 and P2 in horizontal positioning test respectively.

In Fig. 5.11, plates P3 and P4 are compared. Again, horizontal positioning was utilized. Both plates were damaged, and the only difference between the two specimens is the thickness. P4 is thicker than P3. There are sharp curvature changes in the fringe patterns of both specimens at the location of the damage zone.

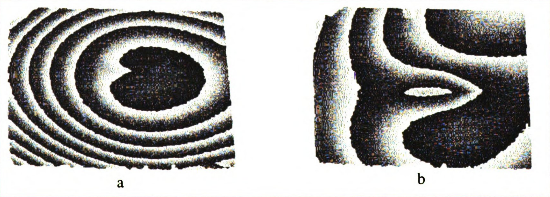

Fig. 5.11 Fringe patterns of P3 and P4 in horizontal positioning test respectively.

Figure 5.12 shows the fringe patterns of plate P1 and P2 from the vertical positioning test. The fringe pattern analysis seems not very straight forward. Even so, any abrupt changes in the fringe pattern would give indications of possible damage or flaws.

Comparing the fringe patterns of undamaged plate P1 with that of damaged plate P2, one finds that there is no clear indication of the damage zone, however, the fringe pattern of the damaged plate is more complex.

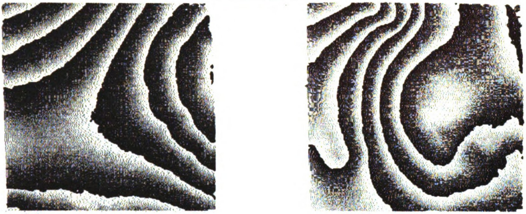
a
b

Fig. 5.12 Fringe patterns of P1 and P2 in vertical positioning test respectively.

The test shown in Figure 5.13 is designed to illustrate the importance of the delay time. Figure 5.13a shows a fringe pattern for undamaged specimen P1 when placed in the horizontal position. Figure 5.13b is for horizontal positioning of damaged specimen P2. Comparing Figures. 5.13a and 5.13b with 5.10a and 5.10b, we see very different fringe patterns. The only difference between the experiment in Figure 5.13 and that in Figure 5.10 is the delay time used after placing the specimens. In the case of Figure 5.13, the delay time was about 3 seconds, which was several seconds shorter than that used in the case of Figure 5.10. Careful comparison of Figure 5.10 and Figure 5.13 shows two things. First, for the same plate P2, the damage indication in Figure 5.10b is much clear than that in Figure 5.13b. In Figure 5.13b, only a slight fringe perturbation in the central area can be seen. This is likely due to the fast overall matrix creep of the entire plate in the first a couple of seconds. When overall creep dominates, it could dominate further localized creep in the damaged region and make the indication of the damage unclear. Second, when undamaged plate P1 and damaged plate P2 are compared in Fig. 5.13, one can see more fringes in the damaged plate P2. This seems to be an indication of the fiber matrix debonding and matrix cracking in P2. It seems that delay time plays an important role in finding the damaged spot.

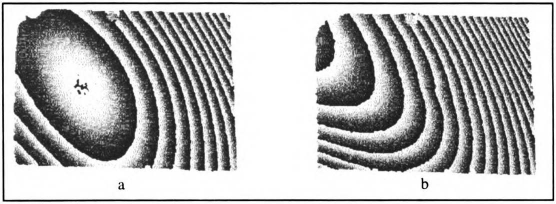
a
b

Fig. 5.13 The effect of the delay time.

3D isometric plots of the out-of-plane displacements as determined with ESPI for the above testing cases are shown in Figure 5.14a-h. This type of plot presents directly the quantitative displacement information. They may provide better visualization of abrupt curvature changes in some cases.

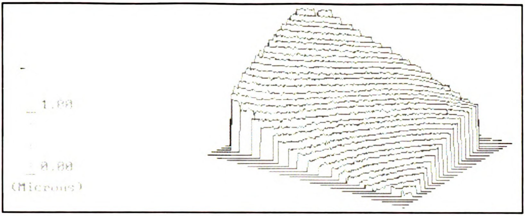

5.14a 3D isometric plot of the deformation of P1 for horizontal positioning test.

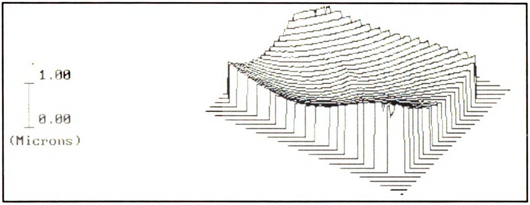

5.14b 3D isometric plot of the deformation of P2 for horizontal positioning test.

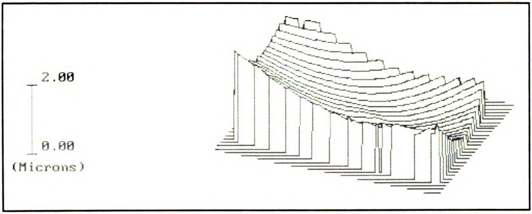

5.14c 3D isometric plot of the deformation of P3 for horizontal positioning test.

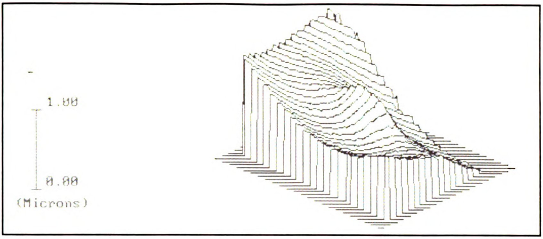

5.14d 3D isometric plot of the deformation of P4 for horizontal positioning test.

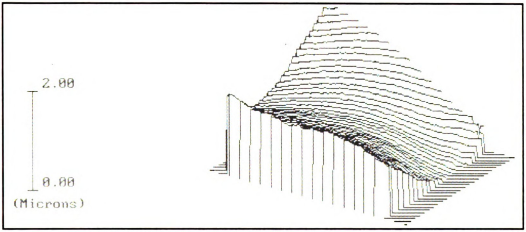

5.14e 3D isometric plot of the deformation of P1 for vertical positioning test.

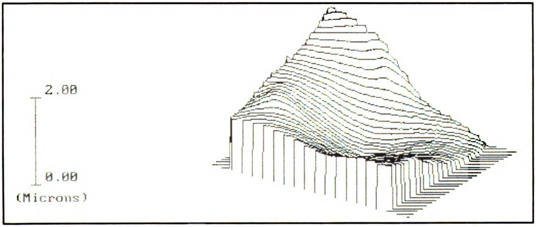

5.14f 3D isometric plot of the deformation of P2 for vertical positioning test.

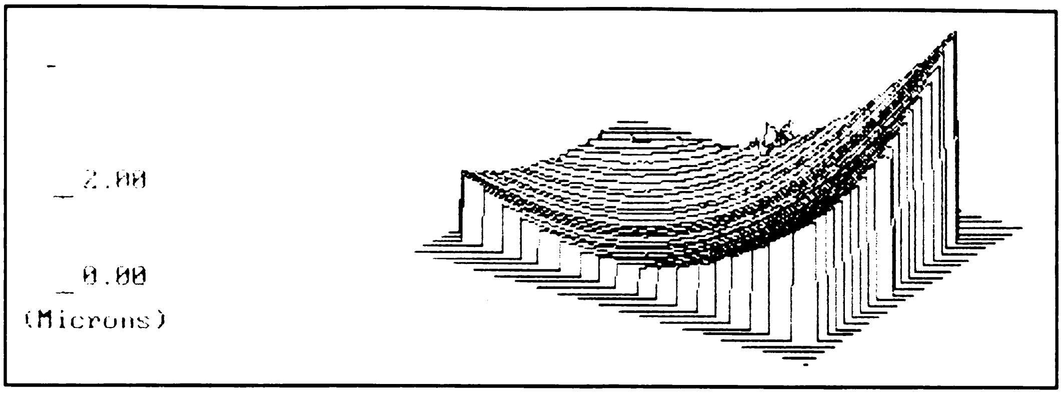

5.14g 3D isometric plot of the deformation of P1 for horizontal positioning test with delay time about 3 seconds.

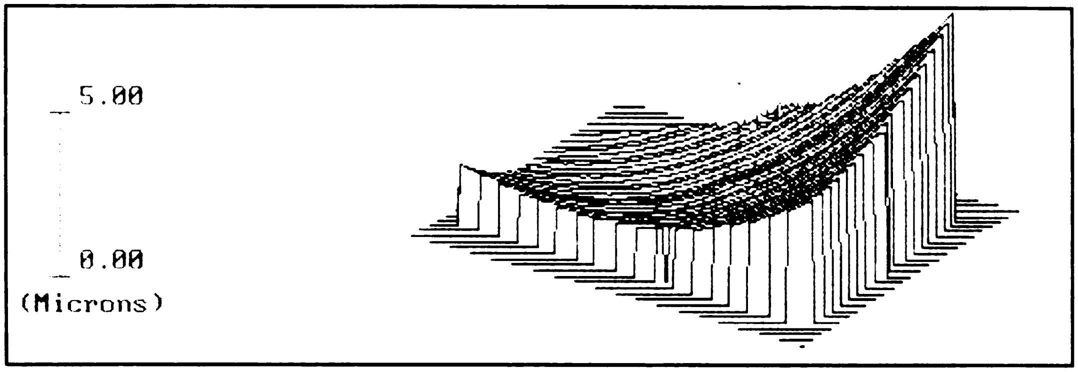

5.14h 3D isometric plot of the deformation of P2 for horizontal positioning test with delay time equal to about 3 seconds.

Fig. 5.14 3D isometric plots of the deformations for various cases studied.

5.4.3 Discussion

In a general case, the total strain is made up of elastic, plastic, creep, and thermal components. In our experiment, the temperature was kept at room temperature, so the thermal component of the strain is zero. The total strain can be written as follows:

$$\varepsilon_{total} = \varepsilon_{el} + \varepsilon_{pl} + \varepsilon_{cr} \tag{5.1}$$

where the subscripts el, pl, and cr refer to the elastic strain, plastic strain, and creep strain, respectively. Elastic strain and plastic strain are instantaneous strains. The plastic strain is zero for gravity loading. The elastic strain will not be recorded because of the delay time. The creep strain can be further broken down into three components given by

$$\varepsilon_{cr} = \varepsilon_p + \varepsilon_s + \varepsilon_t \tag{5.2}$$

where ε_p, ε_s and ε_t refer to primary creep, secondary creep, and tertiary creep respectively. Out of the three creep components, only primary creep is recoverable deformation for polymeric materials.

In this study, the stress introduced by gravity is rather weak. Tertiary creep and rupture do not exist. The secondary stage is basically constant with time. After a short time, typically less than 30 minutes for the glass/epoxy composite plates tested, the creep practically stops and the creep curve reaches its horizontal asymptote. The explanation is that at the beginning of a new position, the resin tends to gradually settle down in a relatively stable distribution or position on the fibers.

The damaged mode in low-velocity impact-damaged fiber-reinforced composite plate is complicated, as stated before. If a fiber breaks into very short pieces, they will likely take a ride along with creeping matrix. At the area where there is matrix-fiber debonding, fiber-matrix interface slip will occur, which can have some effect on the creep strength of fiber composites. Matrix cracking can weaken the ability to transfer load to the fibers, and, therefore, increase the creep. Creep compliance of the composite is inversely proportional to the fiber volume fraction. So, a matrix-rich region may have larger creep.

5.4.4 Conclusion of NDI with gravity loading

- Gravity can be used as a loading technique with an ESPI system to do a certain amount of NDE of composite materials having polymer matrix.
- Composite materials with polymer matrix show significant creep even at room temperature, and this creep is detectable by using the ESPI system. The creep rate goes to zero practically after a short time (about 30 min) under only gravity.
- The position of the specimen as well as boundary conditions affect the detection of a damage spot or flaw. Experiments showed that, in general, horizontal positioning of plates offers better indications of damage than does vertical positioning.
- The delay time plays an important role in finding damage.
- Since no loading device or other peripheral equipment are needed, this method is economical and easy to do. It may be used as the first screening procedure in some NDE applications of composite materials. It can save time and effort.

5.5 Miscellaneous Experimental Results

Some miscellaneous experimental results are presented in this section to illustrate additional applications and some issues related to the use of ESPI/ES.

5.5.1 NDE of adhesive bonding of FRP composite to steel frame

There are three general phases in the repair of structures which incorporate composites: (1) Identifying, locating and assessing damage; (2) performance of repair procedure; and (3) verification of repair. While all the three aspects are very important, the first and the last tend to be given insufficient attention. Yet, they are of crucial importance, especially in complex structures which involve composite panels bonded to frameworks, and which must demonstrate a certain energy management capability for safety reasons.

An experiment was carried out to demonstrate the detection of the debonding areas using ESPI [Cloud, Nokes, and Chen 1993]. In this experiment, a few tests of adhesive joinings have been conducted. A piece of composite (SMC glass/polyester) was glued to a steel frame as shown in Figure 5.15. Adhesive was left out of a small area at one end of the panel, as shown. This is a severe test of the technique since the adhesive is missing in an area of low stress and low stess gradient. The test setup is illustrated in Figure 5.16. Thermal loading was used to stress the structure. This loading device is a hot steam jet. The unbonded area is quite clearly visible as indicated in Figure 5.17.

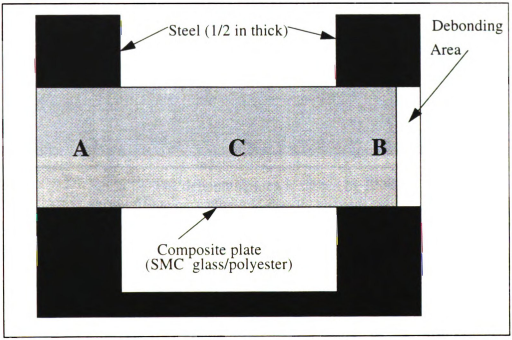

Fig. 5.15 Configuration of the test specimen used for adhesive bonding inspection.

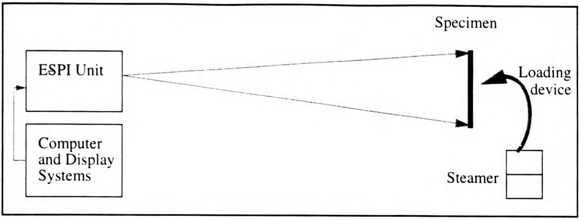

Fig. 5.16 Schematic of experimental setup for NDE applications using ESPI or ES systems.

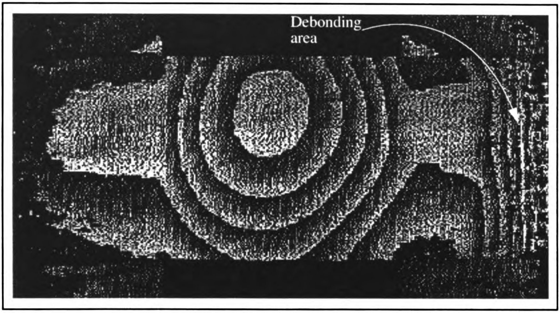

Fig. 5.17 The debonding area is shown by ESPI as abrupt fringe curvature and density changes, as indicated in the picture.

5.5.2 Influence of boundary conditions on the detection of flaws

In NDE using ESPI and ES, boundary conditions can play an important role in the detection of flaws. Some experiments have been carried out to investigate the influence of the boundary conditions on the detection of flaws.

Two different specimens were used for this study. The results are presented as two examples.

(1) Example 1: A 40 W electric bulb was used to apply thermal loading to the specimen. The specimen is a 130 mm x 130 mm 32-ply unidirectional carbon/epoxy plate. The thickness of the plate is about 6.6 mm. Two cuts were made in the specimen, one parallel with the fiber, and the other one perpendicular to the fiber. The size of the cuts is about 25 mm x 3 mm, with a depth of about 1.5 mm. The specimen was placed in a clamping fixture leaving a test area about 120 mm in diameter as shown in Figure 5.18. The experiment setup is the same as show in Figure 5.16 except that the loading device is a 40 W lamp.

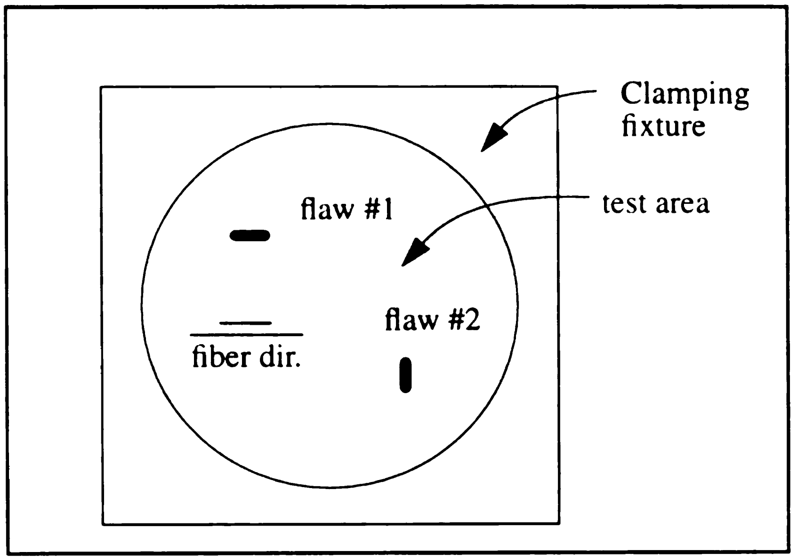

Fig. 5.18 A unidirectional carbon/epoxy composite plate.

In the experiment, several clamping boundary conditions were evaluated. Figure 5.19 shows the result for the case where all the edge is clamped. In this case, only flaw #1 was revealed. Flaw #2 does not introduce detectable disturbance in the fringe pattern under this condition. This is probably because that the deformation in the fiber direction is much less than that of the direction normal to the fiber. Along the direction perpendicular to the fiber the size of flaw #1 is much wider (about 8 times wider) than that of flaw #2. Thus, the disturbance on the heat conduction introduced by flaw #1 is more severe that of flaw #2.

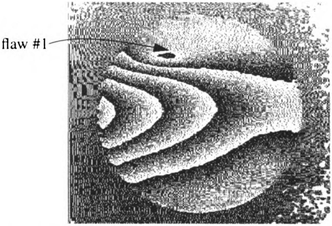

Fig.5.19 Flaw detection using ESPI with all edges clamped. Flaw #1 was revealed, flaw #2 was not revealed.

Figure 5.20 shows the case in which the clamping force on the top and bottom edges of the specimen were somewhat reduced, and the left and right edges were clamped. In this case, only some curvature change caused by flaw #1 can be seen.

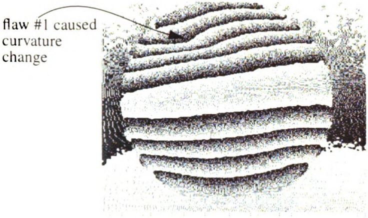

Fig. 5.20 Top and bottom of the plate was partially clamped. Flaw #1 caused some curvature change in the fringes.

Figure 5.21 is the case in which the top and bottom edges of the specimen were not clamped, but the right and left edges remained clamped. In this case, neither of the flaws can be detected. Rigid body motion perpendicular to the fiber dominates.

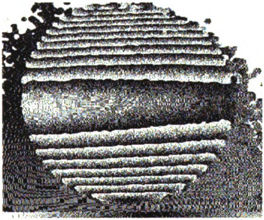

Fig. 5.21 Top and bottom edge of the plate were not clamped. Right and left edge were clamped. No flaw can be observed.

With all edges free, Figure 5.22 shows the result in which no flaw can be revealed. Some "matrix sagging" and "fiber bending" effect were shown in this case owing to the thermal energy applied and the gravity force.

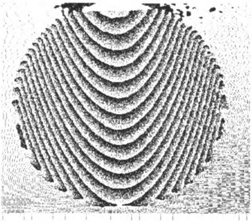

Fig.5.22 All edge are free. No flaws can be revealed.

Example (2): In this example, the same experiment setup was used as in example one. Again, the loading device was a 40 W electric bulb placed at a distance of 6" away from the specimen place. However, the specimen was made from a SMC (sheet molding compound) panel. The fiber is chopped glass strands about 1" long. The matrix material is polyester. Fiber volume fraction is 50%. The specimen is $3mm$ thick and $130mm \times 130mm$ in area. A cut of $20mm \times 3mm$ with depth of $1mm$ was made in the specimen. The same clamping fixture was used as shown in Figure 5.23.

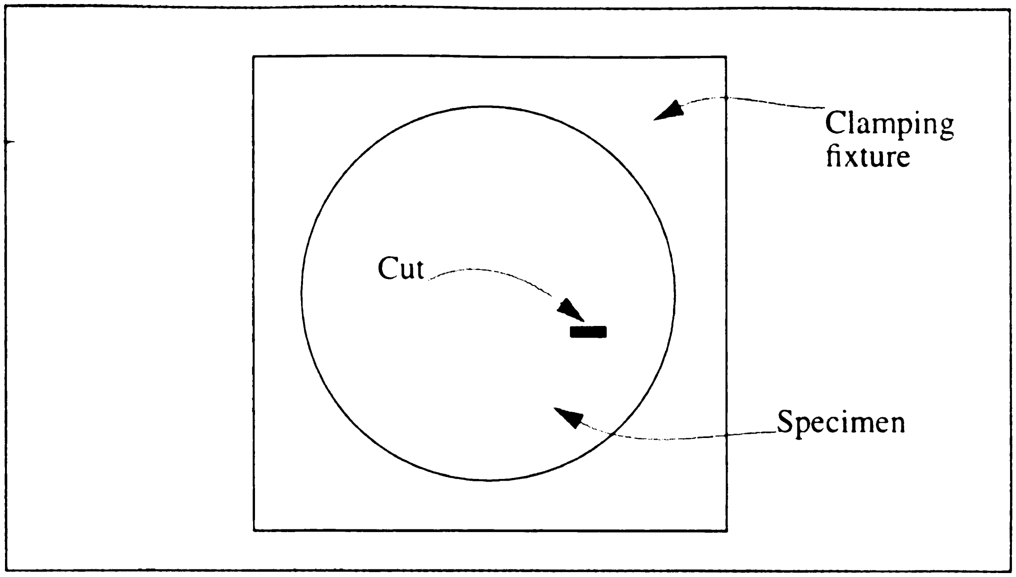

Fig. 5.23 The experimental specimen and fixture used for example 1.

Two boundary conditions were studied. In the first case, the specimen was placed in the fixture without applying any clamping force. Then, the bulb was switched on for a couple of seconds. A dense fringe pattern was developed as shown in Figure 5.24. The major deformation is whole-body expansion/bending caused by the temperature difference between the two sides of the specimen. However, some fringe curvature disruption can be observed around the vicinity of the flaw. The shape of the flaw is not well defined.

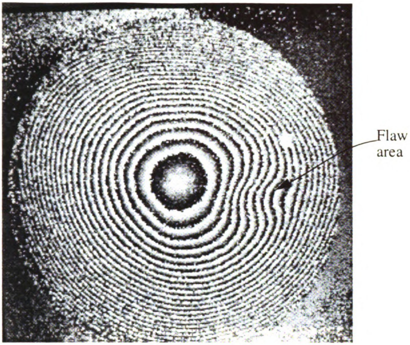

Fig. 5.24 The displacement contour map of example 2 with zero clamping force.

In the second case, the specimen was clamped around all edges in the fixture. Then, the bulb was switched on for several seconds. Because of the constraint applied by the boundary, only a few fringes can be observed. However, the localized deformation at the flaw spot was magnified. The shape of the flaw is now well defined as shown in Figure 5.25. A few seconds later, another speckle pattern was recorded. Due to heat dissipation, much of the area had recovered from the deformation, leaving only a strong indication at the flaw spot as shown in Figure 5.26.

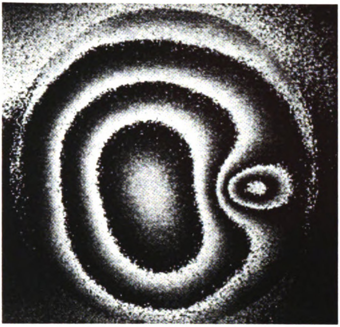

Fig. 5.25 The displacement contour map of example 1 with all edges clamped, showing clearly the area with flaw.

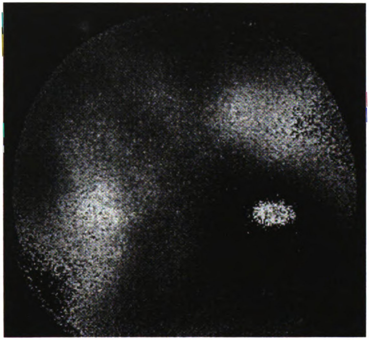

Fig. 5.26 The displacement contour map of Fig. 5.25 taken a few seconds later, most of the specimen had recovered from the stressing, leaving only a flaw indication.

5.5.3 Detection of impact damage in fiber reinforced composite vessels

Because their high strength to weight ratio, Composite Overwrapped Pressure Vessels (COPVs), which have long been used in aerospace applications, are receiving much attention for their potential uses in durable goods industries, particularly as fuel tanks for natural gas vehicles. Product liability and safety are very important issues for a wide applications of these high pressure gas containers. These structures have potentially low tolerance to impacts, and, in vehicles, they must operate through many pressurization cycles. An important element for addressing the impact damage tolerance of COPVs is the development of appropriate NDE methods for detecting impact events.

Interferometric techniques such as ESPI and ES have the potential to meet a number of the NDE requirements for inspection of these COPVs. They are non-contacting, highly sensitive, and allow for fast inspections. Moreover, the measured results can be utilized for integrating with numerically calculated results such as the results obtained from finite element analysis (FEA) to verify and improve designs.

In this experimental program, two types of COPVs are tested. One is a carbon/glass fiber reinforced cylindrical tank with thermoplastic liner, and another one is a graphite fiber reinforced spherical tank with aluminum liner. These tanks were subjected to a range of impact energies using different impactor shapes. Internal pressure was used to stress the tanks. The operation pressure for both types of tanks is 3600 PSI. Only some sample results are presented here. Detailed discussions have been published by our research group [Nokes, Cloud, Chen, and Wede 1995; Cloud, Nokes, Chen, and Wede 1995].

Case 1 -- The cylindrical tank: The structure of the cylindrical tank is shown in Figure

5.27a. The total wall thickness of the tank is about 1/2 inch. The tank is 32 inches long and 13 inches in diameter. One tank was impacted in the cylinder area by a pyramid impactor with 50 FT-LBF. The experimental setup is shown in Figure 5.27b. The results were compared with a identical tank with no damage. Both ESPI and ES were used to detect the damage. The results are shown in Figures 5.28 through 5.31. Figure 5.28 shows the fringe pattern measured from the undamaged tank. The fringes are parallel and uniform owing to the uniform expansion caused by the internal pressure. Figure 5.29 is the digitally filtered ESPI fringe pattern observed from the damaged tank. A "bull-eye" fringe anomaly caused by the impact damage is obvious. An internal pressure of 30 psi was applied to both the damaged and undamaged tanks. The fringe patterns presented by ESPI are out-of-plane displacement contour maps

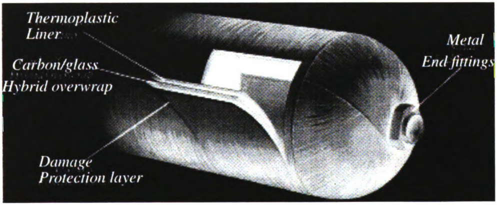

Fig. 5.27a The structure of the cylindrical tank.

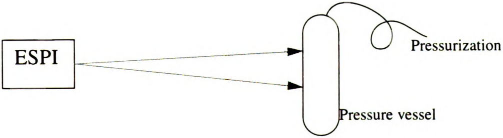

Fig. 5.27b Top-view of the experimental setup for pressure vessel NDI.

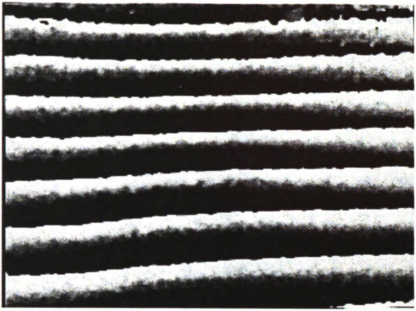

Fig. 5.28 The ESPI fringe pattern from the undamaged tank.

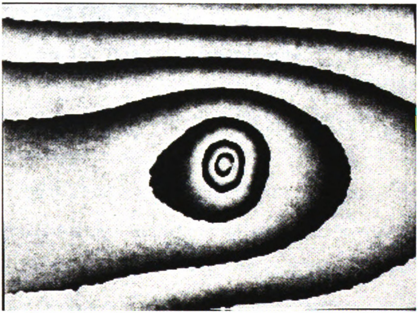

Fig. 5.29 The ESPI fringe pattern from the damaged tank.

Figure 5.30 is a picture of the unfiltered fringe pattern from the undamaged tank measured by ES. No clear fringe can be observed. A "butterfly" fringe anomaly was observed from the damaged tank as shown in Figure 5.31. An internal pressure of 40psi was used to load the tanks. The fringes measured by ES show the in-plane derivative of the out-of-plane displacement contour maps.

Fig. 5.30 The ES fringe pattern from the undamaged tank.

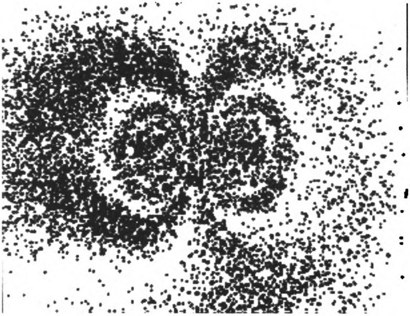

Fig. 5.31 The ES fringe pattern from the damaged tank.

Case 2 -- The spherical tank: The diameter of the tank is 10 inches. The liner material is 5083 aluminum with a nominal thickness of $1.3mm$. The overwrap thickness is $4.6mm$. The impact damage was caused by dropping the spherical tank from the top of a desk. The damage cannot be seen by inspection of the surface. ESPI with internal pressure loading was used to detect the damage. In this case, the comparison was made on the same tank between the damaged area and the undamaged area. The comparison was made at two different pressure levels, 5 psi and 28 psi. Figure 5.32 shows the fringe pattern around the damaged area at an internal pressure of 5 psi. The damage can be seen clearly owing to the reduced strength at the damaged area. Figure 5.33 is the fringe pattern produced by an undamaged area. No fringe was observed.

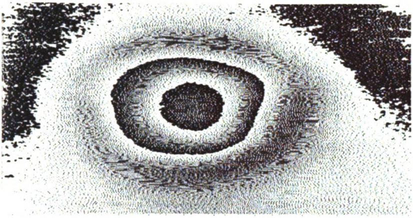

Fig. 5.32 The ESPI fringe pattern of the damaged area at a internal pressure of 5 psi.

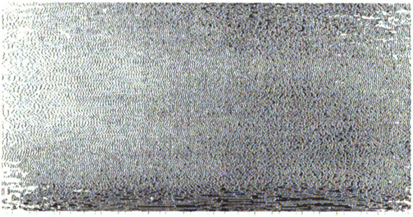

Fig. 5.33 The ESPI fringe pattern of a undamaged area at a internal pressure of 5 psi.

Figure 5.34 shows the fringe pattern produced by the same damaged area at an internal pressure of 28 psi. More fringes were generated because of the higher pressure. A few fringes now can be observed from the undamaged area as shown in Figure 5.35. In comparison with Figure 5.34, the total deformation caused by the pressure is much less than that of the damaged area. Figure 5.36 and 5.37 are the 3D isometric plots of the deformation of the corresponding pictures in Figure 5.34 and 5.35.

Fig. 5.34 The ESPI fringe pattern from the damaged area at 28 psi.

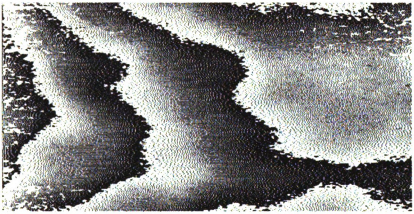

Fig. 5.35 The ESPI fringe pattern observed from an undamaged area at 28 psi.

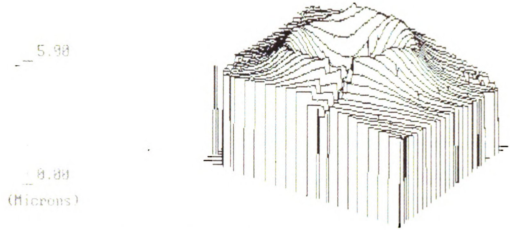

Fig. 5.36 The 3D plot of the surface deformation around the damaged area at 28 psi.

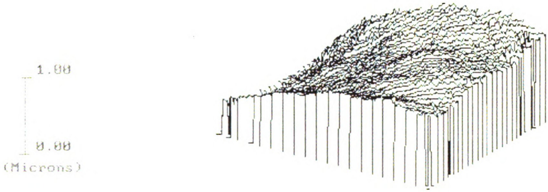

Fig. 5.37 The 3D plot of the surface deformation around the undamaged area at 28 psi.

5.5.4 Creep observation of FRP composites

As discussed in Section 5.4, the creep of some FRP composites at room temperature can be detected using ESPI. The viscous property can be observed by applying a small temperature increase. This section is meant to demonstrate the detection of viscous behavior of a specimen made from a SMC (sheet molding compound) panel. The fiber is chopped glass strands and about 1" long. The matrix material is polyester. Fiber volume fraction is 50%. The specimen is $3mm$ thick and $130mm \times 130mm$ in area. The specimen was clamped around the edges in a fixture. A 40 W electric bulb placed at a distance of 6" from the specimen was used to apply thermal radiation to the specimen. Figure 5.38 shows the fringe pattern taken at about 5 seconds after the bulb was switched on. The fringe pattern is a group of concentric round circles. Figure 5.39 shows the fringe pattern taken at about 10 seconds after the bulb was switched on. Now the fringe pattern is not a group of concentric circles; they are not even round. Because of the viscous property, the center of the group of fringes "flowed" downward owing to the gravity.

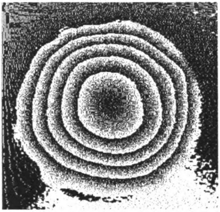

Fig. 5.38 The fringe pattern at about 5 seconds after the bulb was switched on.

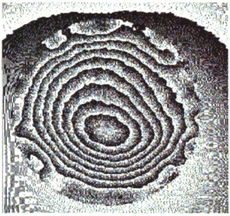

Fig. 5.39 The fringe pattern at about 10 seconds after the bulb was switched on.

5.5.5 Using ESPI for structure analysis and design

ESPI can measure the displacement (deformation) of a structure under load. So, it can be used directly for mechanics analysis of structures. Furthermore, the experimental results from ESPI may be used for verifying finite element analysis results. Three examples are presented in this section to illustrate these applications.

(1) ESPI for FEA verification

A unidirectional carbon/epoxy composite plate was the test specimen. The edges of the specimen were clamped, giving a circular test area. A 'point' temperature source was applied at the center of the circular area. Figure 5.40 is the experimental result from ESPI measurement, and Figure 5.41 shows the result from finite element analysis. In this case, the results are compatible with each other.

(2) Di

Fig

areas o

fact, thi

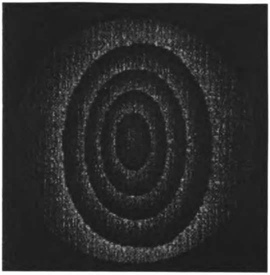

Fig. 5.40 ESPI result of the deformation contour caused by a 'point' thermal load at the center.

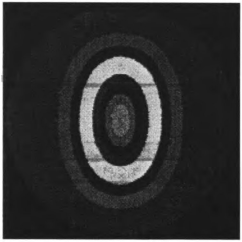

Fig. 5.41 The FEA result of the deformation contour caused by a 'point' thermal load at the center.

(2) Displacement contour maps of a fiber over-wrapped composite vessel

Figure 5.42 shows three out-of-plane displacement contour maps of three different areas on the vessel under internal pressure. Related FEA results are not yet available; in fact, this is a difficult problem to solve.

(3) D

T

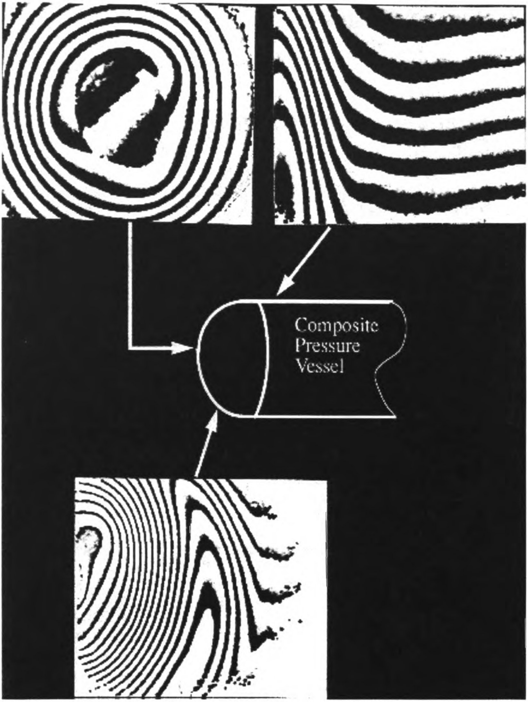

Fig. 5.42 Out-of-plane displacement contour maps around a fiber over-wrapped composite vessel.

(3) Displacement field created by fastening a screw into a honeycomb table

The out-of-plane displacement contour caused by fastening a screw into a honeycomb table was easily observed using ESPI. Figure 5.43 shows the displacement field created by fastening one screw to the table and Figure 5.44 is the displacement contour map caused by fastening two screws to the table.

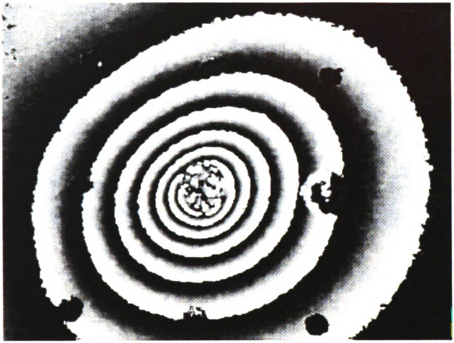

Fig. 5.43 Out-of-plane displacement contour created by fastening a screw into a honeycomb table.

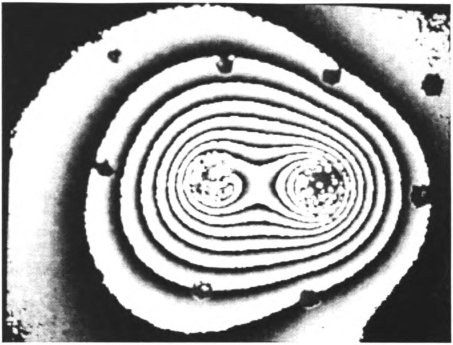

Fig. 5.44 Out-of-plane displacement contour created by fastening two screws into a honeycomb table.

I
r
T
te
co
is p
dar

outl
ESP
syste
algor
static
mathe
deriva
presen

Summary and Conclusions

This work is composed of two parts: (1) a systematic and comprehensive development of theory and practical techniques of ESPI and ES systems, and (2) NDE of FRP composite materials and other applications using ESPI and ES systems. In the study of ESPI and ES theory, detailed analyses and discussions are presented. Practical problems in using the systems are also discussed. A numerical model of an ESPI system has been programed to analyze the influence of the sensitivity vectors on the accuracy of the measurements. A novel NDE method for FRP composites is proposed and presented. This technique takes advantage of the creep characteristics of FRP materials under room temperature and gravity, and it may offer a "loadingless" method for the NDE of FRP composites. A new approach which exploits the advantages of ESPI, ES, and ultrasound is proposed for effective nondestructive inspection. Some experiments on NDE of impact damage of composite vessels will be shown along with other applications.

Chapter One is an introduction which describes briefly the historical background, the outline of the systems, and the applications. Chapter Two and Chapter Three deal with ESPI and ES systems respectively. The systems are analyzed and discussed systematically; these include the optics designs, phase measurement techniques and algorithms, computer hardware requirements etc. The principles of operations of ESPI for static measurement, vibration analysis, and general dynamic events are described mathematically. Strain field analysis through the ES technique which measures only the derivative of the out-of-plane displacement with respect to an in-plane direction is presented. General applications are also presented. Chapter Four focuses on the sensitivity analysis of ESPI (out-of-plane and in-plane) and ES systems. To obtain accurate measurement, the effect of the sensitivity vectors of the system should be taken into account. Chapter Five presents some experimental techniques, results, and more discussion of applications of ESPI and ES systems, especially in the area of nondestructive inspection (NDI). A novel 'loadingless' method is proposed for NDI of polymer composite materials. Experiment shows that the creep at room temperature of these materials is significant enough to be utilized for NDI application. A complementary NDI approach which uses the advantages of the ultrasound technique and the ESPI/ES techniques is discussed and demonstrated experimentally.

Over the past twenty-some years, ESPI and ES techniques have been continuously developed, modified and improved. On one hand, with fast advances in computer science and electronics, ESPI and ES will be further developed. On the other hand, more work is needed to explore and widen the area of applications of these techniques.

The current situation is that: (1) ESPI and ES have been developed into very powerful and promising engineering techniques. (2) ESPI and ES systems will be further improved along with the fast and continuous advances in electronics, computer technologies, and optical components. (3) There is a shortage of effective testing tools for new materials, new manufacturing processes, and new construction techniques. (4) Although there have been many reports on the application of ESPI and ES techniques, their potentials are still far from fully exploited. (5) Industries in general are still slow in realizing the capabilities of ESPI and ES, thus they have not really enjoyed the benefit of the new technologies. On one hand there are the researchers who understand what powerful tools ESPI and ES are, but they don't know where or what the real problems are. On the other hand, we have the manufacturers, people who make things and have problems with the things they make.

They are not aware that ESPI or ES is a possible solution, and this is the main reason why ESPI and ES have not been very popular in industrial applications.

At present, we need to develop industrial user-friendly ESPI and ES systems with more data reduction capability. The use of laser diodes and optical fibers is a key to make the systems more compact and stable. To reduce the influence caused by noise, vibration, air turbulence etc, feedback control and faster CCD frame grabbing electronics may be incorporated in the design of ESPI and ES. To increase the spatial resolution, a higher resolution (2K by 2K) CCD camera may be used. However, the improvement of the hardware performance largely depends on advances of electronics and their prices.

The key for reliable and fast fringe pattern analysis is to have good data. More work needs to be done in developing better fringe data pre-processing algorithms. Technologies developed for finger printing analysis may be utilized in the fringe pattern analysis. Besides the widely used phase-shifting techniques, other techniques such as the Fourier transform method may be used to analyze fringe patterns using fewer frames of data.

So far, the most important area of applications of ESPI and ES is nondestructive inspection of materials and structures. Future effort in this area should be to quantitatively relate ESPI and ES measurements to the flaw and damage detected, and to better predict the behavior of the defects under operating conditions of the materials and structures. Integration of ESPI and ES techniques with numerical methods such as finite element analysis (FEA) may offer some answers to the problem of quantification and identification.

Much effort is needed to explore potential application areas. Many applications are possible in medical science, engineering mechanics, materials science, and environmental study, etc.

The ultimate goal for a wider use of ESPI and ES is to bridge the gap between system development and practical applications. Education of potential users in the operation of these 'high tech' measurement tools is also very important.

LIST OF REFERENCES

REFERENCES

Albertazzi, A. Jr. (1993). Holographic station: a practical system for applying TV holography. SPIE Vol. 2004 Interferometry VI: Applications.

Aleksoff, C. C. (1974). Temporal modulation techniques. in Holographic Nondestructive Testing, edited by R. K. Erf, Academic Press, New York and London 1974, ISBN 0-12-241350-4.

Anastasi, R. F., Serabian, S. M., Shuford, R. J. and Das-Gupta, D. K. (1987). Nondestructive detection of simulated delaminations in composite laminates by laser-speckle shearography. Experimental Techniques, pp 28-31.

Anderson, D.J., Valera, J.D. and Jones, J.D. (1993). Electronic speckle pattern interferometry using diode laser stroboscopic illumination. Meas. Sci. Technol. 4, (1993) 982-987, Engineering Optics, pp475-480.

Andonovic, I. and Uttamchandani, D. (1989). Principles of Modern Optical Systems. ISBN 0-89006-351-6, Artech House, Inc.

Andrä, P., Mieth, U. and Osten, W. (1991). Strategies for unwrapping noisy interferograms in phase-sampling interferometry. SPIE Vol. 1508 Industrial Applications of Holographic and Speckle Measuring Techniques. pp 50-60.

Bao, N.K., Jin, G.C. and Chung, P.S. (1993). A New Electronic Shearing Speckle Pattern Interferometer with Continuously Variable Sensitivity. SPIE Vol. 2066 Industrial Optical Sensing and Metrology, pp63-66.

Bar-Cohen, Y. (1987). Ultrasonic NDE of composites - a review. In Solid Mechanics for Quantitative Non-Destructive Evaluation. J. D. Achenbach and Y. Rajapakse (editors).

Beranek, W. J. (1986). Potential of holographic interferometry for non- destructive testing of polymer composites. Polymer NDE. Proceedings of European Workshop on Nondestructive Evaluation of Polymers and Polymer Matrix Composites. Edited by K. H. G. Ashbee, pp 222-237.

Bischof, Th. and Juptner, W. (1991). Determination of the adhesive load by holographic interferometry using the results of FEM- calculations. SPIE Vol. 1508, Industrial Applications of Holographic and Speckle measuring Techniques, pp 90-95.

Bøving, K. G. (Editor). (1989). NDE Handbook. Butterworths, London. ISBN 0-408-04392-X.

Briers, J. D. (1991). Laser speckle and its temporal variability: the implications for biomedical holography. SPIE Vol. 1429, Holography, Interferometry, and Optical Pattern Recognition in Biomedicine, pp48-54.

Brown, G. C. and Pryputniewicz, R. J. (1992). Investigation of a submillimeter cantilever beam of variable cross section by computational and hologram interferometry methods. SPIE Vol. 1821, pp 72-81.

Brown, G. C. and Pryputniewicz, R. J. (1993). Measurement of young's modulus on thin films under static and dynamic loading conditions. SPIE Vol. 2004 Interferometry VI: Applications.

Brown, G. M. (1993). From tire testing to holometry and beyond. SPIE Vol. 2004 Interferometry VI: Applications. pp2-15.

Brown, G. M., Forbes, J. W., Marchi, M. M. and Wales. (1993). Comparison of holographic interferometry to other test methods in automotive testing. 2004 Interferometry VI: Applications. pp108-117.

Bruning, J. H. (1987). Fringe scanning interferometers. in Optical Shop Testing, D. Malacara edited, Wiley, New York.

Bruning, J. H., Herriott, D.R., Gallagher, J.E., Rosenfeld, D.P., White, A.D. and Brangaccio, D.J. (1974). Digital wavefront measuring interferometer for testing optical surfaces and lenses. Applied Optics, Vol. 13, No.11, pp 2693-2703.

Bryanston-Cross, P. J. and Towers, D. P. (1992). Quantitative holographic interferometry applied to combustion and compressible flow research. SPIE Vol. 1732, Holographics International'92, pp533-546.

Buckberry, C. and Davies, J. (1990). The application of TV- Holography to engineering problems in the automotive industry. SEM Proceedings, Conference on Hologram Interferometry and Speckle Metrology, pp 268-278.

Bushman, T. (1989). Development of a holographic computing system. in Laser Interferometry: Quantitative Analysis of Interferomgrams: Third in a Series, R. J. Pryputniewicz, ed., Proc. Soc. Photo-Opt. Instrum. Eng. 1162, pp 66-77.

Bhushan, B., Wyant, J.C. and Koliopoulos, C.L. (1985). Measuerment of surface topography of magnetic tapes by Mirau interferometry. Applied Optics, Vol. 24, No. 10, pp1489-1497.

Butters, J. N. and Leendertz, J. A. (1971). Speckle pattern and holographic techniques in engineering metrology. Optics and Laser Technology, pp 26-30, Feb. 1971
? 2

Carré, P. (1966), (in French). Installation et utilisation du comparateur photoelectrique et interferentiel du Bureau International des Poids et Mesures. Metrologia 2(1), pp13-23.

Claudine, G. and Xavier, B. (1990). Nondestructive testing by electronic speckle interferometry. SEM Proceedings, Hologram Interferometry and Speckle Metrology, pp 367-373.

Caponero, M. A. and Angelis, A. D. (1992). Vibrational analysis of an aircraft winglet by using of pulsed laser holographic interferometry. SPIE Vol. 1732, Holographics International'92, pp 565-576.

Castro-Montero, Shah, A. S. and Bjelkhagen, H. (1990). A study of the fracture process using laser holographic interferometry and image analysis. SPIE Vol. 1396, Applications of Optical Engineering: Proceedings of OE/Midwest'90, pp 122-130.

Chai, G.B., Chin, S.S., Lim, T.M. and Hoon, K. H. (1993). Vibration analysis of laminated composite plates: TV-holography and finite element method. Composite Structures 23, pp273-283.

Chang, M., Hu, C-P., Lam, P. and Wyant, J. C. (1985). High precision deformation measurement by digital phase shifting holographic interferometry, Applied Optics, Vol. 24, No. 22, pp 3780-3783.

Chapman, G. B. II and Hagerman, E. M. (1993). Nondestructive inspection technology for quality assurance of automotive composites components. ASM and ESD Conference proceedings, Advanced Composites Technologies. pp 621-646.

Chatters, T., Pouet, B. and Krishnaswamy, S. (1992). ESPI with synchronized pressure stressing. SPIE Vol. 1821, pp 38-45.

Chatters, T., Pouet, B. and Krishnaswamy, S. (1993). Nondestructive testing of adhesively bonded structures using synchronized pressure stressing. SPIE Vol. 2001 Nondestructive Inspection of Aging Aircraft. pp 236-247.

Chau, F. S., Toh, S. L., Tay, C. J. and Shang, H. M. (1989). Some examples of nondestructive flaw detection by shearography. Journal of Nondestructive Evaluation, Vol. 8, No. 4, pp 225-234.

Chen, X. L. (1992). Electronic Speckle Pattern Interferometry and Applications in Engineering Mechanics. Master Thesis, Department of Materials Science and Mechanics, Michigan State University, February, 1992.

Chen, X. L. and Cloud, G. L. (1994). Nondestructive evaluation of composites using ESPI and gravity loading. Proc. 1994 SEM Spring Conference and Exhibits, Baltimore, Maryland. June, 1994.

Chen Y., He, X., Chang, B., Zhu, X. and Chen, J. (1990). The application of ESPI technique for analysis of the typical damage models of craniofacial regions. SEM Proceedings, Conference on Hologram Interferometry and Speckle Metrology, pp279-283.

C
c
A
D

Co
pr
Ol

Co
rep
Inc

Cre
pp

Cre
XX

Crea
spec

Cros

Cheng, Y.Y. and Wyant, J. C. (1985). Phase shifter calibration in phase-shifting interferometry. Applied Optics, vol. 24, No.18, pp 3049-3052.

Chiang, F. P. (1993). Some recent advances in speckle methods of strain analysis. ATEM'93 Conference on Advanced Technology in Experimental Mechanics'93, JSME, pp 185-194.

Chiang, F. P., Adachi, J., Anastasi, R. and Baatty, J. (1982). Subjective laser speckle method and its application to solid mechanics problems. Optical Engineering, Vol. 21, No. 3, pp 379-390.

Cloud, G. L. (1995). Optical Methods of Engineering Analysis. Cambridge University Press, 1995.

Cloud, G. L. and Chen, X. L. (1994). Combined interferometric techniques for assessment of damage in composite structures. International Symposium on Advanced Transportation Applications, AACHEN, Germany, November.

Cloud, G, Nokes, J. and Chen, X. (1993). Combined Interferometric Techniques of Assessment of Damage and Verification of Repair in Composite Structure. Proc. Advanced Technologies Conference, ASM & ESD, Dearborn, Michigan, November.

Cloud, G. L., Nokes, J. P., Chen, X. L. and Wede, H. (1995). Nondestructive inspection of composite overwrapped pressurized tanks using two interferometric methods. The 11th Annual Advanced Composites Conference and Exposition, 6-9 November 1995, Dearborn, Michigan.

Cohn, G. E. and Domanik, R. A. (1990). Interferometric analysis for non-destructive product monitoring. SPIE Vol. 1396 Applications of Optical Engineering: Proceedings of OE/Midwest '90, pp 131-142.

Conley, E. and Genin, J. (1990). Application of speckle metrology at a nuclear waste repository. SPIE Vol. 1332, Optical Testing and Metrology III: Recent Advances in Industrial Optical Inspection, pp 798-801.

Creath, K. (1985). Phase-shifting speckle interferometry. Applied Optics, Vol. 24, No. 18, pp 3053-3058.

Creath, K. (1988). Phase-measurement interferometry techniques. Progress in Optics, Vol XXVI, edited by E. Wolf, Elsevier Science Publishers, Amsterdam, pp 349-393.

Creath, K. and Slettemoen, G. Å. (1985). Vibration-observation techniques for digital speckle-pattern interferometry. J. Opt. Soc. Am. A Vol. 2, No. 10, pp1629-1636.

Crostack, H. -A., Meyer, E. H. and Pohl, K. -J. (1991). Holographic soundfield visualization for nondestructive testing of hot surfaces. SPIE Vol. 1508, Industrial Applications of Holographic and Speckle measuring Techniques, pp 101-109.

Cyr, G. J., Hinrichsen, R. L. and Walley, R. A. (1988). Effects of cutouts on the dynamic response of curved rectangular composite panels. AIAA Journal, Vol. 26, No. 5, pp 582-587.

Dainty, J. C. (editor) (1984). Laser Speckle and Related phenomena. Second enlarged edition, Springer-Verlag.

Dan, X., Gong, Y. and Wang, S. (1993). Image processing method for speckle pattern fringe analysis based on a microcomputer. Optical Engineering, Vol. 32, No. 6, pp 1344-1347.

Davis, R. S. (1989). Nondestructive Evaluation with optical holography. Materials Evaluation, 47, pp794-797.

Davies, J. and Buckberry, C. (1989). Applications of a fibre optic TV holography system to the study of large automotive structures. SPIE Vol. 1162 Laser Interferometry: Quantitative Analysis of Interferograms, pp 279-291.

Deaton, J.B. Jr. and Rogowski, R.S. (1993). Applications of electronic shearography for the inspection of airskin structures. SPIE Vol. 2001 Nondestructive Inspection of Aging Aircraft. pp 224-235.

Diao, H., Peng, X., Zou, Y., Tiziani, H. J. and Chen, L. (1992). Contouring using two-wavelength electronic speckle pattern interferometry employing dual-beam illuminations. Optik, 91, No. 1 pp 19-23.

Diao, H., Zou, Y., Peng, X., Tiziani, H. J. and Chen, L. (1992). Calibration of the inclined contour planes formed on ESPI and optimization of ESPI optical system for contouring. Optik, 91, No. 2, pp 71-75.

Diao, H., Zou, Y. and Tiziani, H. J. (1993). Design consideration of a dual- beam ESPI optical system for contouring. Optik, 93, No. 2, pp 45-51.

Dudderar, T. D., Gilbert, J. A., Franzel, R. A. and Schamell, J. H. (1985). Remote vibration measurement by time-averaged holographic interferometry. Experimental Techniques, pp 25-27, Jan..

Durell, W. E. (1991). Fiber optic holography equipment and theory. SPIE 1600 International Symposium on Display Holography, pp 290-293.

Dvies, J. and Buckberry, C. (1989). Applications of a fiber optic TV holography system to the study of large automotive structures. SPIE Vol. 1162 Laser Interferometry: Quantitative Analysis of Interferograms, pp 279-291.

E
S

E
he
1

E
u

E
2

F
p

F
R

F
p

F
p

F
lo

F
6

F
in

F

F
A

F
M
L

C

Ebbeni, J. (1991). Some applications of holographic interferometry in biomechanics. SPIE Vol. 1524, Bioptics: Optics in Biomedicine and Environmental Sciences, pp 75-82.

Ek, L and Jansson, E.V. (1986). Modal properties of wooden plates determined by TV-holography and electroacoustical methods. Journal of Sound and Vibration, 111(1), 115-124.

Ellingsrud, S. and Rosvold, G. O. (1992). Analysis of a data-based TV-holography system used to measure small vibration amplitudes. J. Opt. Soc. Am. A. Vol. 9, No. 2, pp 237-251.

Erf, R. K. (editor) (1978). Speckle Metrology. Academic Press, New York, ISBN 0-12-241360-1.

Fällstrom, K. E. (1991a). A nondestructive method to detect delaminations and defects in plates. NDT & E International, pp 67-76.

Fällström, K. E. (1991b). Determining material properties in anisotropic plates using Rayleigh's method. Polymer Composites, Vol. 12, No. 5, pp 306-314.

Fällström, K. E. and Jonsson, M. (1991). A nondestructive method to determine material properties in anisotropic plates. Polymer Composites, Vol. 12, No. 5, pp 293-305.

Fällström, K. E. and Molin, N. E. (1987). A nondestructive method to determine material properties. Polymer Composites, Vol. 8, No. 2, pp 103-108.

Flemming, T., Hertwig, M. and Usinger, R. (1993). Speckle interferometry for highly localized displacement fields. Meas. Sci. Technol. 4.

Flory, R. E. (1985). Image acquisition technology. Proc. IEEE, Vol. 73, April 1985, pp 613-637.

Floureux, T. (1993). Improvement of electronic speckle fringes by addition of incremental images. Optics & Laser Technology, Vol 25, No 4.

Françon, M. (1966). Optical Interferometry. Academic Press, New York. pp 144.

Françon, M. (1979). Laser speckle and applications in optics. Translated by Henri H. Arsenault, Academic Press.

Froehly, C. (1981). Speckle phenomenon and some of its applications. Optical Methods in Mechanics of Solids, Proceedings of the I.U.T.A.M. Symposium, edited by Alexis Lagarde, pp 279-313.

Gabor, D. (1948). A new microscopic principle. Nature, 161, pp 777-785.

Gabor, D. (1972). Holography, 1948-1971. Proc. IEEE, 60, pp 655-668.

Galanulis, K. and Ritter, R. (1993). Speckle interferometry in material testing and dimensioning of structures. SPIE Vol. 2004 Interferometry VI: Applications.

Ganesan, A.R., Joenathan, C. and Sirohi, R.S. (1988). Sharpening of fringes in digital speckle pattern interferometry. Applied Optics, Vol. 27, No. 11, pp 2099-2100.

Ganesan, A. R., Kothiyal, M. P. and Sirohi, R. S. (1989). Simple image processing techniques for the contrast enhancement of real- time digital speckle pattern. Optical Engineering, Vol. 28, No. 9, pp 1019-1022.

Ganesan, A. R., Sharma, D. K. and Kothiyal, M. P. (1988). Universal digital speckle shearing interferometry. Applied Optics, Vol. 27, No. 22, pp4731-4734.

Garcia, G., Matthews, L. and Hickman, L. (1992). Integration of ESPI and structural analysis to determine the impact of structural defects. SPIE Vol. 1821, pp 64-71.

Ghiglia, D. C., Mastin, G. A. and Romero, L. A. (1987). Cellular-automata method for phase unwrapping. J. Opt. Soc. Am. A, Vol.4, No. 1, pp 267-280.

Greivenkamp, J. E. (1984). Generalized data reduction for heterodyne interferometry. Optical Engineering, Vol. 23, No.4, pp 350-352.

Griffen, C. T., Fryska, S. T. and Bernier, P. R. (1991). Applied holographic interferometry display and quantification methods. SPIE Vol. 1600 International Symposium of Display Holography, pp 333-345.

Gryzagoridis, J. (1992). Holographic methods for component manufacture and evaluation. Int. J. Pres. Ves. & Piping 50, pp 317-335.

Gülker, G., Haack, O., Hinsch, K., Hölscher, C., Kramer, A. and Neunaber, H. (1990). Electronic speckle pattern interferometry system for in situ deformation monitoring on buildings. Opt. Eng. 29, pp 816-820.

Gülker, G., Haack, O., Hinsch, K., Hölscher, C., Kuls, J. and Platen, W.(1991). ESPI system for three dimensional deformation measurement in the investigation of stone decay. SEM Proceedings, Hologram Interferometry and Speckle Metrology, pp 284-287.

Gülker, G., Haack, O., Hinsch, K., Hölscher, C., Kuls, J. and Platen, W. (1992). Two-wavelength electronic speckle-pattern interferometry for the analysis of discontinuous deformation fields. Applied Optics, Vol. 31, No. 22, pp 4519-4521.

Halford, C. E., Gamble, W. L. and George, N. L. (1987). Experimental investigation of the longitudinal characteristics of laser speckle. Optical Engineering, Vol. 26, No. 12, pp 1263-1264.

Hariharan, P. (1975). Speckle-shearing interferometry: a simple optical system. Applied Optics, Vol. 14, No. 11, pp 2563.

Hariharan, P. (1984). Optical Holography. Cambridge University Press.

Hariharan, P., Oreb, B.F. and Brown, N. (1982). A digital phase-measurement system for real-time holographic interferometry. Optics Communications, Vol.41, No.6, pp 392-396.

Hariharan, P., Oreb, B.f. and Eiju, T. (1987). Digital phase-shifting interferometry: a simple error-compensating phase calculation. Applied Optics, Vol. 26, No. 13, pp 2504-2508.

He, S., Wang, L., Dbbins, B. and Kapasi, S. (1991). Investigation of natural convection phenomena from a horizontal heated tube using ESPI. Acta Mechanica Sinica (in Chinese), Vol. 23, No. 6, pp 733-737.

Hertwig, M., Flemming, T. and Usinger, R. (1994). Speckle interferometry for detection of subsurface damage in fibre-reinforced composites. Meas. Sci. Technol. 5.

Hinsch, K. (1991). Coherent optical metrology for environmental diagnostics. SPIE Vol. 1542 Bioptics: Optics in Biomedicine and Environmental Sciences. pp 292-313.

Höfling, R., Aswendt, P., Totzauer, W. and Jüptner, W. (1991). DSPI: A tool for analyzing thermal strain on ceramic and composite materials. SPIE Vol. 1508, Industrial Applications of Holographic and Speckle Measuring Techniques, pp 135-142.

Høgmoen, K and Løkberg, O. J. (1976). Vibration phase mapping using electronic speckle pattern interferometry. Applied Optics, Vol. 15, No. 11. pp 2701-2704.

Høgmoen, K. and Løkberg, O.J. (1977). Detection and measurement of small vibrations using electronic speckle pattern interferometry. Applied Optics, Vol. 16, No. 7, pp 1869-1875.

Holownia, B. P. (1988). Examination of adhesive joints using electronic speckle pattern interferometry. Plastics and Rubber Processing and Applications 9, pp 203-208.

Hsu, D.K., Patton, T.C., Aglan, H. and Shroff (1993). Fatigue-induced disbonds in adhesive lap splices of aluminum and their ultrasonic detection. SPIE Vol. 2001 Nondestructive Inspection of Aging Aircraft. pp 2-13.

Hung, Y. Y. (1974). A speckle-shearing interferometer: a tool for measuring derivatives of surface displacements. Optics Communications, Vol. 11, No. 2, pp 132-135.

Hung, Y. Y. (1982). Shearography: a new optical method for strain measurement and nondestructive testing. Optical Engineering, Vol. 21, No. 3, pp 391-395.

Hung, Y.Y. (1989a). Apparatus and method for electronic analysis of test object. US patent 4,887,899.

Hung, Y.Y. (1989b). Shearography versus holography in nondestructive evaluation of tires and composites. SPIE Proc. Vol. 814, pp433-442.

Hung, Y. Y. (1993). Nondestructive evaluation of composites by digital shearography. ASM and ESD Conference proceedings, Advanced Composite Technologies, pp 647-665.

Hung, Y.Y. (1994). A phase shift technique for automation of phase determination in digital shearography. SEM 1994 Spring Conference, Baltimore.

Hung, Y. Y. and Liang, C. Y. (1979). Image-shearing camera for direct measurement of surface strains. Appl. Opt., Vol. 18, No. 7, pp 1046.

Hung, Y. Y., Long, K. W. and Hovanesian, J. D. (1990a). Fast detection of residual stresses in an industrial environment by electronic shearography. Conference on Hologram Interferometry and Speckle Metrology, pp 134-139.

Hung, Y. Y., Rowlands, R. E. and Daniel, I. M. (1975). Speckle-shearing interferometry techniques: a full-field strain gauge. Applied Optics, Vol. 14, No. 3, pp618-622.

Hung, Y.Y., Tang, S.H. and Hovanesian, J.D. (1990b). Automated deduction of displacement derivatives employing carrier-fringe shearography and fast Fourier transformation. Hologram Interferometry and Speckle Metrology, pp 140-145.

Hung, Y. Y. and Taylor, C. E. (1974). Measurement of slopes of structural deflections by speckle-shearing interferometry. Experimental Mechanics, pp 281-285.

Hung, Y.Y., Wang, J.Q. and Hovanesian, J.D. (1994). A technique for compensating excessive rigid body motion in nondestructive testing of large structures using shearography. SEM 1994 Spring Conference, Baltimore, pp76-84.

Iwahashi, Y., Iwata, K. and Nagata, R. (1984). Single-aperture speckle shearing interferometry with a single grating. Applied Optics, Vol. 23, No. 2. pp247-249.

Iwahashi, Y., Iwata, K. and Nagata, R. (1985). Influence of in-plane displacement in single-aperture and double-aperture speckle shearing interferometry. Applied Optics Vol. 24, No. 14. pp2189-2192.

Jähne, Bernd. (1993). Digital Image Processing. Second Edition, Springer-Verlag. ISBN 3-540-56941-3.

Jin, G., Bao, N. and Chung, P.S. (1994). Applications of a novel phase-shift method using a computer-controlled polarization mechanism. Optical Engineering, Vol. 33, No. 8. pp 2733-2737.

Jin, G. and Tang, S. (1992). Electronic speckle pattern interferometer with a polarization phase-shift technique. Optical Engineering, Vol. 31, No. 4, pp 857-860.

Joenathan, C. (1990). Recent Developments in electronic speckle pattern interferometry. SEM Proceedings, Hologram Interferometry and Speckle Metrology, pp 198-204.

Joenathan, C. (1991). Vibration fringes by phase stepping on an electronic speckle pattern interferometer: an analysis. Applied Optics, Vol. 30, No. 32.

Joenathan, C. and Khorana, B. M. (1990). Phase measuring fiber optic electronic speckle pattern interferometer. SPIE Vol. 1396 Applications of Optical Engineering: Proceedings of OE/Midwest'90, pp155-163.

Joenathan, C. and Khorana, B. M. (1991). A simple and modified ESPI system. Optik, 88, No. 4, pp169-171.

Joenathan, C. and Khorana, B. M. (1992a). Phase-measuring fiber optic electronic speckle pattern interferometer: phase step calibration and phase drift minimization. Optical Engineering, Vol. 31, No. 2, pp315-321.

Joenathan, C. and Khorana, B.M. (1992b). On the electronic speckle pattern interferometric vibration fringes. SPIE Vol. 1779, pp230-238.

Joenathan, C. and Khorana, B.M. (1992c). Contrast of the vibration fringes in time-averaged electronic speckle-pattern interferometry: Effect of speckle averaging. Applied Optics, Vol. 31, No. 11, pp1863-1870.

Joenathan, C. and Khorana, B. M. (1993). Quasi-equal-path electronic speckle pattern interferometric system. Applied Optics, Vol. 32, No. 29, pp 5724-5726.

Joenathan, C. and Torroba, R. (1991a). Modified electronic speckle pattern interferometer employing an off-axis reference beam. Applied Optics, Vol. 30, No. 10, pp 1169-1171.

Joenathan, C. and Torroba, R. (1990b). Simple electronic speckle-shearing-pattern interferometer. Optics Letters, Vol. 15, No. 20, pp1159-1161.

Jones, R. and Wykes, C. (1989). Holographic and Speckle Interferometry. Second edition, Cambridge University Press.

Jones, T. S. and Berger, H. (1989). Application of nondestructive inspection methods to composites. Materials Evaluation, 47, April. pp390-400.

Kadura, S. and Dovgalenko, G. (1992). Application of dynamic holographic interferometry to DNA protein study. SPIE Vol. 1647, pp 202-205.

Kamshilin, A. A., Oliva, A. and Moreno, È. (1990). Use of dynamic holography to study the elastic properties of solids. Sov. Phys. tech. Phys. 35(6). pp 742-744.

Kardestuncer, H. and Pryputniewicz, R.J. (1984). Unification of FEM with laser experimentation. Chapter 9, Unification of finite element methods. H. Kardestuncer (editor), North-Holland, Amsterdam, pp. 207-234.

Kasprzak, H., Forster, W. N. and von Bally, G. (1994). Holographic measurement of changes of the central corneal curvature due to intraocular pressure differences. Optical Engineering, Vol. 33, No. 1.

Kasprzak, H. and Sultanova, N. (1994). Simple holographic interferometric method of investigating the Poisson coefficient and elasticity moduli. Optical Engineering, Vol. 33, No. 1, pp194-197.

Kato, J., Yamaguchi, I. and Ping, Q. (1993). Automatic deformation analysis by a TV speckle interferometer using a laser diode. Applied Optics, Vol. 32, No. 1, pp 77-83.

Katsuma, H., Sato, K. and Iwaki, A. (1992). Many problems about recording the biomedical properties by means of holography. SPIE Vol. 1647, pp88-95.

Kerr, D., Santoyo, F.M. and Tyrer, J. R. (1989). Manipulation of the Fourier components of speckle fringe patterns as part of an interferometric analysis process. Journal of Modern Optics, 36(2), pp195-203.

Kerr, D., Santoyo, F.M. and Tyrer, J. R. (1990). Extraction of phase data from electronic speckle pattern interferometric fringes using a single-phase-step method: a novel approach. J. Opt. Soc. Am. A, Vol. 7, No. 5, pp820-826.

Kerr, D. and Tyrer, J. (1988). Use of high resolution real-time image processing techniques in generation and analysis of ESPI fringe patterns. Optics and Lasers in Engineering 8, pp109-121.

Kimoto, M., Nagata, I., Minowa, A., Moriwaki, K. and Watanabe, K. (1990). Evaluation of disbondings and measurement of Poisson's ration for plastics composites using holographic interferometry. Journal of Applied Polymer Science, Vol. 40, pp1085-1093.

Klausbruckner, M. J. and Pryputniewicz, R. J. (1992). Holographic and computational study of coupled vibration of channel beams. SPIE Vol. 1821, pp54-63.

Klumpp, P. A. and Schnack, E. (1990). Shearograms with variable measurement sensitivity. Experimental Techniques, pp42-44, July/Aug..

Kojima, A., Ogawa, R., Izuchi, N., Yamamoto, M., Nishimoto, T. and Matsumoto, T. (1991). Deformation measurement of the bone fixed with external fixator using holographic interferometry. SPIE Vol. 1429, Holography, Interferometry, and Optical Pattern Recognition in Biomedicine, pp162-171.

Krautkrämer, J. and Krautkrämer, H. (1977). Ultrasonic Testing of Materials. 3rd ed. Springer-Verlag,

Lai, G. and Yatagai, T. (1991). Generalized phase-shifting interferometry. J. Opt. Soc. Am. A/Vol. 8, No.5, pp822-827.

Lee, K. B., Park, S. J., Kwon, Y. K. and Lee, B. H. (1992). Three-dimensional displacement and strain of a vibrating plate determined by holographic interferometry and the finite element method. Journal of Sound and Vibration, 153(1), pp63-75.

Leendertz, J. A. and Butters, J. N. (1973). An image-shearing speckle-pattern interferometer for measuring bending moments. Journal of Physics E: Scientific Instruments 1973, Vol. 6, pp1107-1110.

Leith, E., Chen, H., Chen, Y., Dilworth, D., Lopez, J., Masri, R., Rudd, J. and Valdmanis, J. (1991). Imaging through tissue using electronic holography and femtosecond pulses. SPIE Vol. 1600, International Symposium on Display Holography, pp172-177.

Lim, J. S. (1990). Two Dimensional Signal and Image Processing. Prentice Hall, ISBN 0-13-935322-4.

Liu, W., Tan, Y. and Wang, X. (1990). Fiber optic electronic speckle pattern interferometry and its applications to sensors. SPIE Vol. 1814 Optical Sensors, pp-167-174.

Liu, W., Tan, Y. and Wang, X. (1992). Electronic speckle pattern interferometry using multimode fiber optic bundles for sensing measurement. SPIE Vol. 1814 Optical Sensors, pp112-118.

Løkberg, O. J. (1979). Use of chopped laser light in electronic speckle pattern interferometry. Applied Optics, Vol. 18, No. 14, pp2377-2384.

Løkberg, O. J. ((1980). Electronic speckle pattern interferometry. Phys. Technol., Vol. 11, pp16-22.

Løkberg, O. J. (1991). Speckle and speckle techniques for bio-medical applications. SPIE Vol. 1524 Bioptics: Optics in Biomedicine and Environmental Sciences, pp35-47.

Løkberg, O. J., Ellingsrud, S. and Vikhagen, E. (1990). TV- holography (ESPI) and image processing in practical use. SPIE Vol. 1332 Optical Testing and Metrology III: Recent Advances in Industrial Optical Inspection, pp142-150.

LØkberg, O. J. and HØgmoen, K. (1976). Use of modulated reference wave in electronic speckle pattern interferometry. Journal of Physics E: Scientific Instruments, Vol. 9, pp847-851.

Lokberg, O. J., HØgmoen, K. and Holje, O.M. (1979). Vibration measurement on the human ear drum in vivo. Applied Optics, Vol. 18, No. 6. pp763-765.

LØkberg, O. J. and Malmo, J. T. (1988). Long-distance electronic speckle pattern interferometry. Optical Engineering, Vol. 27, No. 2. pp150-156.

LØkberg, O.J., Rosvold, G.O., Malmo, J. T. and Ellingsrud, S. (1991). Computerized vibration analysis of hot objects. SPIE Vol. 1508 Industrial Applications of Holographic and Speckle Measuring Techniques. pp 153-160.

LØkberg, O. J. and Slettemoen, G. A. (1987). Basic Electronic Speckle Pattern Interferometry. Chapter 8, Applied Optics and Optical Engineering, Vol. X, edited by Shannon, Robert R. and Wyant, James C., Academic Press, Inc.

Lu, B., Hu, Z., Abendroth, H., Eggers, H. and Ziolkowski, E. (1990). Improvement of time-average subtraction technique applied to vibration analysis with TV-holography. Optics Communications, Vol. 78, No. 3,4, pp217-221.

Lu, B., Yang, X., Abendroth, H. and Eggers, H. (1989). Time-average subtraction method in electronic speckle pattern interferometry. Optics Communications, Vol. 70, No. 3, pp177-180.

Lu, Y., Jiang, L., Zou, L., Zhao, X. and Sun, J. (1990). The Non-destructive testing of printed circuit board by phase shifting interferometry. SPIE Vol. 1332, Optical Testing and Metrology III: Recent advances in Industrial Optical Inspection, pp287-291.

Macovski, A., Ramsey, S. D. and Schaefer, L. F. (1971). Time-lapse interferometry and contouring using television system. Applied Optics, Vol. 10, No. 12, pp 2722-2727.

Maden, M. A. and Farris, R. J. (1991). Stress analysis of thin polymide films using holographic interferometry. Experimental Mechanics, pp178-184. June.

Maeta, M., Kawakami, S., Orgawara, T. and Masuda, Y. (1991). Vibration analysis of the tympanic membrane with a ventilation tube and a perforation by holography. SPIE Vol. 1429 Holography, Interferometry, and Optical Pattern Recognition in Biomedicine. pp152-161.

Magnusson, R., Wang, X., Hafiz,, A. Black, T. D., Shji-Sheikh, A., Konecni, S., and Wilson, D. R. (1994). Experiments with photorefractive crystals for holographic interferometry. Opt. Eng. Vol. 33, No. 2. pp596--607.

Maji, A. K. and Wang, J. (1992). Fracture mechanics of a tension-shear microcrack in rocks. Experimental Mechanics, pp190-196, June.

Maji, A. K., Wang, J. L. and Lovato, L. (1991). Electronic Speckle Pattern Interferometry for fracture mechanics testing. Experimental Techniques, pp19-23.

Malmo, J. T., LØkberg, O. J. and Slettemoen, G. A. (1988). Interferometric testing at very high temperatures by TV holography (ESPI). Experimental Mechanics, pp315-321, Sept..

Malmo, J. T. and Vikhagen, E. (1988). Vibration analysis of a car body by means of TV holography. Experimental Mechanics, pp28-30, April.

Malmo, J. and Vikhagen, E. (1990). TV-Holography used in testing and inspection of materials and components. SEM Proceedings, Hologram Interferometry and Speckle Metrology, pp 152-157.

Markhvida, I. V. and Tanin, L. V. (1991). Experimental investigation of speckle size distribution. SPIE Vol. 1508, Industrial Applications of Holographic and Speckle Measuring Techniques, pp128-134.

Miller, R. A., Castro-Montero, A. and Shah, S. P. (1991). Use of laser holographic interferometry and image analysis for the study of fracture specimens. Experimental Techniques (May/June).

Mohanty, R. K., Joenathan, C and Sirohi, R. S. (1985). Speckle and speckle-shearing interferometers combined for the simultaneous determination of out-of-plane displacement and slope. Applied Optics, Vol. 24, No. 18, pp3106-3109.

Montgomery, P.C. and Berquist, B.D. (1985). Contrast enhancement of ESPI vibration patterns by speckle averaging in a video frame store. in Optics in Engineering Measurement, W.F. Fagan, ed., Proc. Soc. Photo-Opt. Instrum. Eng. 599, 201-206.

Moore, A.J., Tyrer, J.R. and Santoyo, F.M. (1994). Phase extraction from electronic speckle pattern interferometry addition fringes. Applied Optics, Vol. 33, No. 31, pp7312-7320.

Morgan, C.J. (1982). least-squares estimation in phase-measurement interferometry. Optics Letters, Vol.7, No.8, pp368-370.

Moslehy, F.A., Mueller, S.A. and Davis, R.M. (1993). Application of laser-based methods and finite element analysis to bond verification of space shuttle tiles. SPIE Vol. 2066 Industrial Optical Sensing and Metrology. pp26-35.

Murthy, R. K., Sirohi, R. S. and Kothiyal, M. P. (1982). Speckle shearing interferometry: a new method. Applied Optics, Vol. 21, No. 16, pp2865-2867.

Nakadate, S. and Saito, H. (1985). Fringe scanning speckle-pattern interferometry. Applied Optics, Vol. 24, No. 14, pp 2174-2180.

Nakadate, S., Yatagai, T. and Saito, H. (1980a). Digital speckle-pattern shearing interferometry. Applied Optics, Vol. 19, No. 24, pp4241-4246.

Nakadate, S., Yatagai, T. and Satito, H. (1980b). Electronic speckle pattern interferometry using digital image processing techniques. Applied Optics, Vol. 19, No. 11, pp 1879-1883.

Newman, J. W. (1986). Holographic inspection of composites. SPIE Vol. 604, Holographic Nondestructive Testing, pp 57-62.

Ng, T.W. and Chau, F.S. (1992). Suppression of fringe modulating in-plane displacement fields in shearing speckle interferometry. SPIE Vol. 1821.

Nokes, J., Cloud, G., Chen, X. and Wede, H. (1995). Interferometric Inspection of Composite Overwrapped Pressure Vessels. 1995 SEM Spring Conference, Grand Rapids, Michigan, June 12-14.

Ohtsu, M. (1992). Highly Coherent Semiconductor Lasers. Artech House, Inc. Boston, London, ISBN 0-89006-462-8.

Osten, W., Jüptner, W. and Mieth, U. (1993). Knowledge assisted evaluation of fringe patterns for automatic fault detection. SPIE Vol. 2004, Interferometry VI: Applications. pp256--268.

Ovryn, B. (1992). Measurement of the converse piezoelectric effect in ceramic and bone using phase-stepped holographic interferometry. SPIE Vol. 1647, pp179-185.

Owner-Petersen, M. (1991a). Digital speckle pattern shearing interferometry: limitations and prospects. Applied Optics, Vol. 30, No. 19, pp2730-2738.

Owner-Petersen, M. (1991b). Decorrelation and fringe visibility: on the limiting behavior of various electronic speckle-pattern correlation interferometers. J. Opt. Soc. Am. A Vol. 8, No. 7.

Owner-Petersen, M. (1991c). Phase map unwrapping: A comparison of some traditional methods and a presentation of a new approach. SPIE Vol. 1508 Industrial Applications of Holographic and Speckle Measuring Techniques. pp73-82.

Paoletti, D. and Spagnolo, G. S. (1993). Automated digital speckle pattern interferometry contouring in artwork surface inspection. Optical Engineering, Vol. 32, No. 6.

Parker, R. J. and Jones, D. J. (1988). Holography in an industrial environment. Optical Engineering, Vol. 27, No. 1.

Pechersky, M. J. and Bergen, T. F. (1990). ESPI measurements of submerged composite plate vibrations. Conference on Hologram Interferometry and Speckle Metrology. Proceedings of SEM, pp254-259.

Pedersen, H.M., LØkberg, O. J. and FØrre, B.M. (1974). Holographic vibration measurement using a TV speckle interferometer with silicon target vidicon. Optics Communications, Vol. 12, No. 4, pp421-426.

Peng, S., Joenathan, C. and Khorana, B. M. (1992). Development of a compact phase measuring ESPI system using single mode fiber and diode laser. SPIE Vol. 1779, pp212-217.

Peng, X., Diao, H., Zou, Y. and Tiziani, H. J. (1992a). Contouring by modified dual-beam ESPI based on tilting illumination beams. Optik, 90, No. 2 pp 61-64.

Peng, X., Diao, H., Zou, Y. and Tiziani, H. J. (1992b). A novel approach to determine decorelation effect in a dual-beam electronic speckle pattern interferometer. Optik 90, No. 3, pp129-133.

Peng, X., Zou, Y.L., Pedrini, G. and Tiziani, H.J. (1993). A simplified multi-wavelength ESPI contouring technique based on a diode laser system 2: Automatic fringe analysis. Optik 92, No. 3. pp114-118.

Pouet, B. F. and Krishnaswanmy, S. (1993). Additive/subtractive decorrelated electronic speckle pattern interferometry. Optical Engineering, Vol. 32, No. 6. pp1360-1369.

Powell, R. L. and Stetson, K. A. (1965). Interferometric Vibration Analysis by Wavefront Reconstruction. J. Opt. Soc. Am. 55, pp1593-1598.

Preater, R. and Swain, R. (1990). In-plane strain measurement on high speed rotating components using pulsed laser ESPI. SEM Proceedings, Hologram Interferometry and Speckle Metrology, pp288-293.

Preater, R. and Swain, R. (1993). A preliminary assessment of the requirements to transfer in-plane ESPI to an industrial spinning pit facility. SPIE Vol. 2004 Interferometry VI: Applications. pp142-149.

Pryputniewicz, R. J. (1992a). Quantitative holographic studies in biomedicine. SPIE Vol. 1647, pp 206-214.

Pryputniewicz, R.J. (1992b). Electronic shearography and electronic holography working side by side. SPIE Vol. 1821, pp27-37.

Quiroga, J. A. and Bernabeu, E. (1994). Phase-unwrapping algorithm for noisy phase-map processing. Applied Optics, Vol. 33, No. 29, pp6725-6731.

Rao, C. B., Venkatraman, B., Shyamsunder, M. T., Raj, B. and Bhattacharya, D. K. (1987). Precise-twist measurement by laser-holographic interferometry. Experimental Techniques, pp 26-27.

Rastogi, P. K., Pflug, L. and Delez, R. (1989). Noninvasive observation of embryonic behavior in chicks using holographic interference. Applied Optics, Vol. 28, No. 7. pp1378-1381.

Ratnam, M. M., Evans, W. T. and Tyrer, J. R. (1992). Measurement of thermal expansion of a piston using holographic and electronic speckle pattern interferometry. Optical Engineering, Vol. 31, No. 1, pp61-69.

Robinson, D. W. (1983). Automatic fringe analysis with a computer image-processing system. Applied Optics, Vol. 22, No. 14, pp2169- 2176.

Robinson, D. W. and Williams, D. C. (1986). Digital phase stepping speckle interferometry. Optics Communications, Vol. 57, No., 1, pp26-30.

Rossing, T. D. and Hampton, D. S. (1990). Modal analysis of musical instruments with holographic interferometry. SPIE Vol. 1396, Applications of Optical Engineering: Proceedings of OE/Midwest'90, pp108-121.

Rottenkolber, H. and Juptner, W. (1989). Holographic Interferometry in the next decade. SPIE Vol. 1162, Laser Interferometry: Quantitative Analysis of Interferomgrams, pp 2-15.

Rowland, A. C. and Santoyo, F. M. (1986). Evaluation of dynamic volume viscoelasticity using electronic speckle pattern interferometry. Optical Engineering, Vol. 25, No. 7, pp865-870.

Rubayi, N. A. and Liew, S. H. (1989). Vacuum stressing technique for composite laminates inspection by optical method. Experimental Techniques, pp 17-20, Mar.

Safai, M. (1992). Real-time shearography of silicone rubber bonds. Materials Evaluation, pp698-701, June.

Safai, M. (1993). Nondestructive evaluation of aircraft fuselage panels with electronic shearography. SPIE Vol. 2066 Industrial Optical Sensing and Metrology, pp 20-25.

Saluja, C. L., Button, B. L. and Dobbins, B. N. (1988). Full-field in situ measurement of local mass transfer coefficient using ESPI with the swollen polymer technique. Int. J. Heat Mass Transfer, Vol. 31, No. 7, pp1375-1384.

Santoyo, F. M., Moore, A. J., Tyrer, J. R. and Ochoa, N. A. (1994). Noise reduction in twin-pulsed addition electronic speckle pattern interferometry fringe patterns. Optical Engineering, Vol. 33, No. 5. pp1712-1716.

Santoyo, F. M., Shellabear, M. C. and Tyrer, J. R. (1991a). Four cases of engineering vibration studies using pulsed ESPI. SPIE Vol. 1508 Industrial Applications of Holographic and Speckle Measuring Techniques, pp143-152.

Santoyo, F. M., Shellabear, M. C. and Tyrer, J. R. (1991b). Whole field in-plane vibration analysis using pulsed phase-stepped ESPI. Applied Optics, Vol. 30, No. 7. pp717-721.

Saxby, Graham. (1988). Practical Holography. Prentice Hall, New York, ISBN 0-13-693797-7.

Schwider, J., Falkenstörfer, O., Schreiber, H., Zöller, A. and Streibl, N. (1993). New compensating four-phase algorithm for phase-shift interferometry. Optical Engineering, Vol. 32, No.8, pp1883-1885.

Sciammarella, C. A., Bhat, G. K. and Albertazzi, A. Jr. (1991). Electro-optical system for the non-destructive evaluation of bioengineering materials. SPIE Vol. 1429, Holography, Interferometry, and Optical Pattern Recognition in Biomedicine, pp183-194.

Sciammarella, C. A., Bhat, G. and Bayeux, P. (1993). A portable electro-optical interferometer. ATEM'93, Conference on Advanced Technology in Experimental Mechanics'93 JSME.

Sciammarella, C. A., Bhat, G. and Vaitekunas, J. (1990). Measurement of strains at high temperatures by means of electro-optics holography. Hologram interferometry and speckle metrology, Proceedings of SEM, pp205-214.

Shang, H. M., Lim, E. M. and Lim, K. B. (1991). Computer-aided assessment of debonds in laminates from shearographic fringe patterns. Journal of Materials Processing Technology, 25, pp 55-67.

Sharma, D.K., Sirohi, R.S. and Kothiyal, M.P. (1984). Simultaneous measurement of slope and curvature with a three-aperture speckle shearing interferometer. Applied Optics, Vol. 23, No. 10, pp1542-1546.

Shellabear, M.C., Santoyo, F.M. and Tyrer, J.R. (1990). Processing of addition and subtraction fringes from pulsed ESPI for the study of vibrations. SEM Proceedings, Hologram Interferometry and Speckle Metrology, pp238-244.

Sickinger, H., Falkenstorfer, O., Lindlein, N. and Schwider, J. (1994). Characterization of microlenses using a phase-shifting shearing interferometer. Optical Engineering, Vol. 33, No. 8. pp 2680-2686.

Silvennoinen, R., Nygren, K. and Karna, M. (1992). Holographic nondestructive testing in bone biomechanics. SPIE Vol. 1647, pp156-163.

Slettemoen, G. Å. (1977). Optimal signal processing in electronic speckle pattern interferometry. Optics Communications, Vol. 23, No. 2, pp213-216.

Slettemoen, G. Å. (1979). General analysis of fringe contrast in electronic speckle pattern interferometry. Optica Acta, Vol. 26, No. 3, pp313-327.

Slettemoen, G. A. (1980). Electronic speckle pattern interferometric system based on a speckle reference beam. Applied Optics, Vol. 19, No. 4, pp 616-623.

Smigielski, P.(1991). Holography: a tool for wide-spread industrial applications, analysis and comments. SPIE Vol. 1508, Industrial applications of Holographic and Speckle Measuring Techniques, pp38-49.

Smigielski, P., Albe, F. and Dischli, B. (1992). Real-time holographic endoscopy. SPIE Vol. 1647, pp186-193.

Soares, O. D. D., Almeida, M. S. P. and Bermardo, L. M. (1991). Holography in Biosciences. SPIE Vol. 1524, Bioptics: Optics in Biomedicine and Environmental Sciences, pp48-74.

Sollid, J. E. (1975). Holography applied to structural components. Optical Engineering, Vol. 14, No.5

Spooren, R. (1992a). Double-pulse characteristics of a single-oscillator Nd: YAG laser affecting its performance in TV holography. Applied Optics, Vol. 31, No. 2, pp208-216.

Spooren, R. (1992b). Double-pulse subtraction TV holography. Optical Engineering, Vol. 31, No. 5.

Stetson, K. A. (1974). Holographic Vibration analysis. Chapter 7 in Holographic Nondestructive Testing, by Erf, R.K. (editor), pp202.

Stetson, K. A. (1975). A review of speckle photography and interferometry. Optical engineering, Vol. 14, No. 5.

Stetson, K. A. (1989). An electronic system for real-time display and quantitative analysis of hologram interference fringes. L.I.A. Vol. 70 ICALEO, pp 78-85.

Stetson, K. A. (1990a). Theory and applications of electronic holography. Hologram Interferometry and Speckle Metrology, Proceedings of SEM, pp294-300.

Stetson, K. A. (1990b). Use of sensitivity vector variations to determine absolute displacements in double exposure hologram interferometry. Applied Optics, Vol. 29, No. 4.

Stetson, K. A. and Brohinsky, W. R. (1985). Electro-optic holography and its application to hologram interferometry. Applied Optics, Vol. 24, No. 21, pp3631-3637.

Stetson, K. A. and Brohinsky, W. R. (1987). Electro-optic holography system for vibration analysis and nondestructive testing. Optical Engineering, Vol. 26, No. 12, pp 1234-1239.

Stetson, K. A. and Brohinsky, W.R. (1988). Fringe-shifting technique for numerical analysis of time-average holograms of vibrating objects. J. Opt. Soc. Am. A. Vol. 5, No. 9, pp1472-1476.

Summerscales, J. (1990). NDT of advanced composites - an overview of the possibilities. Britich Journal of NDT, Vol. 32, No. 11, pp 568-576.

Surrel, Y. (1993). Phase stepping: a new self-calibrating algorithm. Applied Optics, Vol. 32, No. 19, pp3598-3600.

Taniguchi, M., Oki, M. and Takagi, T. (1991). Basic study on possibility for application of optical fiber to the interferometry. Proc. 1991 IEEE Instrumentation & Measurement Technology Conference, pp135-137.

Tatam, R. P., Davies, J. C., Buckberry, C. H and Jones, J. D. C. (1990). Electronic speckle pattern surface contouring using optical fibres and wavelength modulation of laser diodes. SPIE Vol. 1314 Fiber Optics'90, pp278-283.

Templeton, D. W. and Hung, Y. Y. (1989). Shearographic fringe carrier method for data reduction computerization. Optical Engineering, Vol. 28, No. 1, pp030-034.

Toyooka, S and Kadono, H. (1990). Digital speckle shearography using a liquid-crystal phase shifter. SEM Proceedings, Conference on Hologram Interferometry and Speckle Metrology, pp 158-163.

Tyrer, J.R. (1988). The use of TV holography (ESPI) for loudspeaker chassis and cabinet modal analysis. J. Audio Eng. Soc., Vol. 36, No.5, pp342-349.

Tyrer, J. R. and Versteeg, H. K. (1992). Use of ESPI in hemodynamics: a means of visualizing vessel blood flow. SPIE Vol. 1647, pp114-124.

Valera, J. D., Doval, A. F. and Jones, J.D.C. (1993). Combined fibre optic laser velocimeter and electronic speckle pattern interferometer with a common reference beam. Engineering Optics, pp289-293.

Valera, J. D., Harvey, D. and Jones, J. D. C. (1992). Automatic heterodyning in fiber optic speckle pattern interferometry using laser velocimetry. Optical Engineering, Vol. 31, No. 8. pp1646-1653.

Vest, C. M. (1979). Holographic Interferometry. John Wiley & Sons, Inc. ISBN 0-471-90683-2.

Vikhagen, E. (1989). Vibration measurement using phase shifting TV-holography and digital image processing. Optics Communications, Vol. 69, No. 3, 4. pp214-218.

Vikhagen, E. (1990). Nondestructive testing by use of TV holography and deformation phase gradient calculation. Applied Optics, Vol. 29, No. 1. pp137-144.

Vikhagen, E. (1991). TV holography: spatial resolution and signal resolution in deformation analysis. Applied Optics, Vol. 30, No. 4, pp420-425.

Vikhagen, E. and Løkberg, O. J. (1990). Detection of defects in composite materials by television holography and image processing. Materials Evaluation, 48, pp 244-248.

Vollesen, J. H. (1990). Quantitative vibration data with time average ESPI and PC-based image processing. SEM Proceedings, Hologram Interferometry and Speckle Metrology, pp225-231.

Vrooman, H. A. & Maas, A. M. (1991). Image processing algorithms for the analysis of phase-shifted speckle interference patterns. Applied Optics, Vol. 30, No. 13, pp1636-1641.

Wang, W-C., Day, C-H., Hwang, C-H. and Chiou, T-B. (1993). Nondestructive testing of composite materials by ESPI. ATEM'93 Conference on advanced Technology in Experimental Mechanics'93, JSME.

Wippler, C., Aroulfaraj, M., Schirrer, R. and Pixa, R. (1988). Experimental determination of the evolution of internal stresses in a composite material: case of a circular bilayered laminate glass-resin. Polymer Composites, Vol. 9, No. 2.

Wizinowich, P. L. (1990). Phase shifting interferometry in the presence of vibration: a new algorithm and system. Applied Optics, Vol. 29, No. 22, pp 3271-3279.

Wood, C. P. and Trolinger, J. D. The application of real- time holographic interferometry in the nondestructive inspection of electronic parts and assemblies. SPIE Vol. 1332 Optical Testing and Metrology III: Recent Advances in Industrial optical Inspection, pp122-131.

Wyant, J.C., Oreb, B.F. and Hariharan, P. (1984). Testing a spherics using two-wavelength holography: use of digital electronic techniques. Applied Optics, Vol. 23, No. 22, pp4020-4023.

Wykes, C. (1987). A theoretical approach to the optimization of electronic speckle interferometry fringes with limited laser power. Journal of Modern Optics, Vol. 34, No. 4, pp539-554.

Zhang, F., Wang, J., Qin, Y. and Zhang, Y. (1990). The effect of the camera resolution on fringe patterns in electronic shear speckle pattern interferometry. SPIE Vol. 1230

International Conference on Optoelectronic Science and Engineering'90, pp154-156.

Zheng, W. (1992). Phase-stepping DSPI and its applications. SPIE Vol. 1821, pp 46-53.

Zou, Y., Peng, X. and Tiziani, H. J. (1993). Two-wavelength DSPI surface contouring through the temperature modulation of a laser diode. Optik, 94, No. 4, pp 155-158.